RF COIL SYSTEM DESIGN FOR MRI APPLICATIONS IN INHOMOGENEOUS MAIN MAGNETIC FIELD

A THESIS SUBMITTED TO
THE GRADUATE SCHOOL OF NATURAL AND APPLIED SCIENCES
OF
MIDDLE EAST TECHNICAL UNIVERSITY

BY

AYHAN OZAN YILMAZ

IN PARTIAL FULFILLMENT OF THE REQUIREMENTS
FOR
THE DEGREE OF MASTER OF SCIENCE
IN
ELECTRICAL AND ELECTRONICS ENGINEERING

JUNE 2007

Approval of the Graduate School of Natural and Applied Sciences.

Prof. Dr. Canan Özgen
Director

I certify that this thesis satisfies all the requirements as a thesis for the degree of Master of Science.

Prof. Dr. İsmet Erkmen
Head of Department

This is to certify that we have read this thesis and that in our opinion it is fully adequate, in scope and quality, as a thesis for the degree of Master of Science.

Prof. Dr. B. Murat Eyüboğlu
Supervisor

Examining Committee Members

Prof. Dr. Nevzat Güneri Gençer (METU, EE)

Prof. Dr. B. Murat Eyüboğlu (METU, EE)

Associate Prof. Sencer Koç (METU, EE)

Assistant Prof. Yeşim Serinağaoğlu (METU, EE)

Prof. Dr. Ergin Atalar (Bilkent, EE)

I hereby declare that all information in this document has been obtained and presented in accordance with academic rules and ethical conduct. I also declare that, as required by these rules and conduct, I have fully cited and referenced all material and results that are not original to this work.

Name, Last name :

Signature :

ABSTRACT

RF COIL SYSTEM DESIGN FOR MRI APPLICATIONS IN INHOMOGENEOUS MAIN MAGNETIC FIELD

Yilmaz, Ayhan Ozan
Ms, Department of Electrical and Electronics Engineering
Supervisor: Prof. Dr. B. Murat Eyüboğlu

June 2007, 146 pages

In this study, RF coil geometries are designed for MRI applications using inhomogeneous main magnetic fields. The current density distributions that can produce the desired RF magnetic field characteristics are obtained on predefined cubic, cylindrical and planar surfaces and Tikhonov, CGLS, TSVD and Rutisbauer regularization methods are applied to match the desired and generated magnetic fields. The conductor paths, which can produce the current density distribution calculated for each surface selection and regularization technique, are determined using stream functions. The magnetic fields generated by the current distributions are calculated and the error percentages between the desired and generated magnetic fields are found. Optimum conductor paths that are going to be produced on cubic, cylindrical and planar surfaces and the required regularization method are determined on the basis of error percentages and realizability of the conductor paths.

The optimum conductor path calculated for the planar coil is realized and in the measurement done by LakeShore 3-Channel Gaussmeter, an average error percentage of 11 is obtained between the theoretical and measured magnetic field. The inductance values of the realized RF coil are measured; the tuning and matching capacitance values are calculated and the frequency characteristics of the system is tested using Electronic Workbench 5.1. The quality factor value of the tested system is found to be 162.5, which corresponds to a bandwidth of 39.2 KHz at 6.387 MHz (operating frequency of METU MRI system).

The techniques suggested in this study can be used in order to design and realize RF coils on predefined arbitrary surfaces for inhomogeneous main magnetic fields. In addition, a hand held MRI device can be manufactured which uses a low cost permanent magnet to provide a magnetic field and generates the required RF field with the designed RF coil using the techniques suggested in this study.

Keywords: Magnetic Resonance Imaging, Rf Coil Design, Inhomogeneous Main Magnetic Field, Rf Field, Stream Functions, Basis Functions, Method of Moments, Surface Current Density

ÖZ

HOMOJEN OLMAYAN ANA MANYETİK ALANDA MANYETİK REZONANS GORÜNTÜLEME İÇİN RF SARGISI SİSTEMİ TASARIMI

Yilmaz, Ayhan Ozan

Yüksek Lisans, Elektrik ve Elektronik Mühendisliği Bölümü

Tez Yöneticisi: Prof. Dr. B. Murat Eyüboğlu

Haziran 2007, 146 sayfa

Bu çalışmada, homojen olmayan ana manyetik alanlarda kullanılmak üzere RF sargısı geometrileri tasarlanmıştır. İstenen RF manyetik alan karakterini oluşturabilecek akım yoğunluğu dağılımı, önceden tanımlanmış kübik, silindirik ve düzlemsel yüzeylerde Momentler Yöntemi kullanılarak elde edilmiş, elde edilen akım yoğunluğu dağılımlarının yarattığı manyetik alanın istenen alana yaklaştırılması için Tikhonov, CGLS, TSVD ve Rutisbauer düzenlileştirme yöntemleri uygulanmış, her bir yüzey seçimi ve düzenlileştirme yöntemi için hesaplanan akım yoğunluğunu oluşturabilecek iletken şekilleri Akı Fonksiyonları kullanılarak belirlenmiştir. Elde edilen akım yoğunluğu dağılımlarının oluşturduğu manyetik alanlar hesaplanmış, hesaplanan alanlar ile oluşturulmak istenen alanlar arasındaki hata yüzdeleri hesaplanmıştır. Hata yüzdeleri ve iletken şekillerinin hayata geçirilebilme kolaylığı göz önünde bulundurularak; silindirik, kübik ve düzlemsel yüzeyler üzerine yerleştirilmek üzere optimum iletken şekilleri belirlenmiş, bu şekilleri elde etmek için kullanılması gereken düzenlileştirme yöntem ve parametreleri belirlenmiştir.

Elde edilen sonuçlardan düzlemsel yüzey için hesaplanan iletken şekli gerçekleştirilmiş, teorik olarak hesaplanan manyetik alan ile LakeShore 3 Kanallı Gaussmetre kullanılarak ölçülen manyetik alan arasında 11 ortalama hata yüzdesi elde edilmiştir. Gerçekleştirilen RF sargısının indüktans değerleri ölçülmüş, ayarlama ve eşleme kapasitör değerleri hesaplanmış, Electronic Workbench 5.1 kullanılarak elde edilen sistem test edilmiştir. Test edilen sistemin kalite faktör değeri 162.5 olarak belirlenmiştir. Bu değer 6.387 MHz'te (ODTU MRG sistemi çalışma frekansı) 39.2 KHz'lik bir bant genişliğine karşılık gelmektedir.

Bu çalışmada önerilen teknikler kullanılarak homojen olmayan bir ana manyetik alanda kullanılabilecek RF sargıları, önceden tanımlanmış yüzeyler üzerinde tasarlanıp gerçekleştirilebilir. Ayrıca geliştirilen sargı sayesinde kalıcı mıknatıs ile yaratılan manyetik alanlar kullanılarak elde uygulanabilecek taşınabilir bir manyetik rezonans görüntüleme cihazı tasarlanabilir.

Anahtar Kelimeler: Manyetik Rezonans Görüntüleme, Rf Sargısı Tasarımı, Homojen Olmayan Ana Manyetik Alan, RF Alanı, Akı Fonksiyonları, Taban Fonsiyonları, Momentler Yöntemi, Yüzey Akım Yoğunluğu

To my father,

ACKNOWLEDGMENTS

I would like to express my profound gratitude to my advisor Prof. Dr. Murat Eyüboğlu for his guidance and support throughout this study.

I owe much to my friend Volkan Emre Arpınar, who is a great hero saving people that get stuck in problems, for his help in my progress throughout my studies. I thank Evren Değirmenci and Dario Martin Lorca for their motivation and mental support. Thanks to Mustafa Seçmen for his help to construct the coil and to Zekeriya Özgün for his help to construct the experimental setup. I would also like to thank Hüs, Doğa, Taha and Koray for being together throughout the way.

I feel grateful to my family for giving me the heart and mind to overcome the difficulties and all the situations I have faced.

I was so lucky to have the support of Dilek, concon butterfly, and Dunç, Ayşegül, the güvercin; and the cakes and böreks of Nihal Teyze on hard days.

Also thanks to Aero for manufacturing the air bed I used for several nights though for the last few days the air lasted only for three hours. On the overall, it was bliss to serve for a purpose that provides progress in health occasions. I hope I could perform a few paces towards the health and comfort of human beings.

TABLE OF CONTENTS

LIST OF TABLES

LIST OF FIGURES

CHAPTER 1

INTRODUCTION

Magnetic Resonance imaging is a tomographic imaging technique that produces images of internal physical and chemical characteristics of an object from externally measured nuclear magnetic resonance (NMR) signals. The first successful nuclear magnetic resonance (NMR) experiment was made in 1946 independently by two scientists in the United States. Bloch *et al* [1, 2] and Purcell *et al* [3], found that when certain nuclei were placed in a magnetic field they absorbed energy in the radio frequency range of the electromagnetic spectrum, and re-emitted this energy when the nuclei transferred to their original state. The strength of the magnetic field and the radio frequency matched each other as earlier demonstrated by Joseph Larmor and is known as the Larmor relationship.

In 1973, Paul Lauterbur described a new imaging technique [4]. This referred to the joining together of a weak gradient magnetic field with the stronger main magnetic field allowing the spatial localization of two test tubes of water. He used a back projection method to produce an image of the two test tubes. This imaging experiment moved from the single dimension of NMR spectroscopy to the second dimension of spatial orientation being the foundation of Magnetic Resonance Imaging (MRI).

Raymond Damadian demonstrated that a NMR tissue parameter (termed T1 relaxation time) of tumor samples, measured in vitro, was significantly higher than normal tissue. The first whole body image is published by Damadian *et al* [5] in 1977.

Clinical MRI uses the magnetic properties of hydrogen and its interaction with both a large external magnetic field and radio waves to produce highly detailed images of the human body. Conventional MRI relies upon highly homogeneous magnetic fields and linear gradient field. In this thesis, designing RF coils for inhomogeneous fields is studied.

MRI using open imaging systems is discussed in several studies. Bálibanu *et al* [6] simulated the NMR signal and investigated the effect of pulse sequences for a hand held NMR-MOUSE (mobile universal surface explorer) composed of a permanent magnet which was modeled as surface elements and an RF coil, which was modeled as set of circles.

Anferova *et al* [7] measured the dead times for NMR signals for an NMR-MOUSE hardware setup composed of a permanent with two poles, set of straight wires serving as a gradient coil between the poles, and spiral shaped RF coil placed parallel to the magnet's pole surfaces. Casanova and Blümich [8] obtained a two dimensional image using a similar structure with an additional gradient field. Improving the study of Casanova and Blümich, Perlo *et al* [9] achieved 3D imaging with the single sided sensor.

Blümler *et al* [10] designed a similar hand held NMR device introducing an additional sweep coil to enhance the static field of the permanent magnet and obtained two dimensional images on planes normal to the permanent magnet pole surface.

All the studies stated above utilized the inhomogeneous magnetic field as the main magnetic field. However, they either tried to produce a magnetic field as homogenous as possible or selected a particular region where the main field did not relatively vary. On the contrary, Prado [11] worked in an inhomogeneous main field without the effort of selecting a relatively homogeneous region and measured echo signals with a circular RF coil, which he connected to a relay controlled unit that could switch to different capacitor connections so that the coil could be tuned to different frequencies matching the magnetic field amplitude values. However, he did not worry about the magnetic field produced by the coil or obtaining an image by spatial encoding. RF field, in these studies, are desired to be homogeneous and perpendicular to the main field, but the concern on RF coils only consisted of forming a coarsely perpendicular field to the main field by placing the coil on a perpendicular plane in spiral or circular structures.

While most of the studies on MRI in inhomogeneous fields approach the inhomogeneity as a defect to be amended, there are some studies that make use of the inhomogeneity. Thayer [12] and Yigitler [13] simulated MRI making use of inhomogeneous main magnetic fields. In Yigitler's study an inhomogeneous RF field is used in order to excite the spins and two dimensional images are obtained by the simulation.

Studies on the optimization of coil shapes are usually carried out for conventional MRI applications. There are two main kinds of RF coils, volume coils and surface coils. Volume coils include Helmholtz coils, saddle coils, and birdcage coils. Volume coils can be used as either transmit or receive coils.

The most common RF coil for volume imaging in MRI, is the RF birdcage coil which encloses the imaged volume allowing open access from the top and bottom sides. The birdcage coil was first introduced by Hayes *et al* [14]. The studies of Tropp [15], [16] on birdcage coils form a basis for RF coil improvements in MRI. Doty *et al* [17] developed a new class of RF volume coil denoted as Litz coil, improving the tuning range, homogeneity, tuning stability and sensitivity compared to birdcage coils. To allow greater access to the imaged volume, it is advantageous to design an RF coil with more open sides, such as in front as well as top and bottom.

One of the first open RF coils was designed by Roberts *et al* [18], who used longitudinal wires on two parallel plates as the coil and obtained images of the human abdomen in axial and sagittal planes. Open birdcage coils have been designed by breaking the two end-rings at the zero current points and then using half of the coil to generate the magnetic field [19], [20]. A U-shaped coil was also investigated for the different directional modes using the half-birdcage principle [21]. Alternatively, dome-shaped RF coils have been designed to enclose only the top half of the imaged volume [22], [23].

Surface coils have high SNR, but a small field of view (FOV). To improve signal coil design, arrays of surface coils are used [24], [25]. This increases the FOV without decreasing SNR. In order to improve the quality factor, SNR and radiation loss of the surface coils, microstrip and high temperature conducting materials of various alloys have been used for surface coils.

Lee *et al* [26] used an array of parallel microstrips with a high permittivity substrate. Zhang *et al* [27] developed a microstrip spiral coil that reduced the radiation loss and perturbation of the sample loading to the RF coil compared to conventional surface coils.

Ma *et al* [28], [29] developed and fabricated circular High-Temperature Superconductor (HTS) coils made from $YBCO(YBa_2Cu_3O_7 - Yttriumbarium copperoxide)$ thin films on two inch $LaAlO_3(LanthanumAluminate)$ substrates with chemical etching techniques and achieved better quality factors and image qualities compared to spiral copper coils and volume coils.

Ginefri *et al* [30] compared a spiral HTS coil made with $YBCO$ superconductor on $LaAlO_3$ substrate with copper coil of same shape varying the sizes, temperatures of the coils and size of the sample. They proved a range of 4.1-11.4 fold improvement in SNR over that obtained with the room-temperature copper coil.

The open RF coil designs stated above are generally modifications of volume coils or variations of simple circular, spiral or circular geometries. The coil shape is usually fixed at the beginning of each study and the variables such as the materials of coil fabrication, the dimensions of the conductor, the number of turns for a spiral or size of the gap between conductors are aimed to be optimized. Also the quantities that are desired to be improved are usually quality factor and SNR values rather than the magnetic field produced by the coil.

Using an inverse approach can broaden the limits of the coil design problem in the sense that the coil shape can be determined based on the desired quantities rather than determining an initial coil and measuring how close the quantities are to the desired ones.

One of the first studies that used inverse approach to design coils was performed by Martens *et al* [31] who designed the conductor contours on two parallel planes for a gradient coil based on the magnetic field that is desired to be produced by the coil.

Later Fujita *et al* [32] extended the inverse approach to optimize wire patterns of a cylindrical RF coil by quasi-static approach based on SNR and magnetic field of the coil.

The studies carried out by Lawrence *et al* [33], [34], While *et al* [35] and Müftüler *et al* [36] obtained current distribution on cylindrical surfaces by inverse approach, discretized current density using Method of Moments and obtained conductor patterns using stream functions. The images obtained by

Lawrence *et al* [33], [34] proved averaged SNR and better homogeneity compared to birdcage coils.

This thesis outlines the design of an open RF coil using the time-harmonic inverse approach, as an extension to and modification of the technique outlined in [19]. This method entails the calculation of an ideal current density on arbitrary surfaces that would generate a specified magnetic field. Different regularization techniques are used to match the generated magnetic field and the desired magnetic field. The stream-function technique is used to ascertain conductor pattern.

The design approach used in this thesis differs from previous designs by using a modification of the time-harmonic inverse approach to calculate the current required to generate the specified field. Also, differing from previous designs, this work aims to design an RF coil that can be utilized in MRI applications that use an inhomogeneous magnetic field as the main field. Therefore, the magnetic field that is specified to be generated by the RF coil is required to be also inhomogeneous.

1.1 Background

A nucleus with a non-zero spin creates a magnetic field around it, which is analogous to that of a microscopic bar magnet. Physically, this is called *nuclear magnetic dipole moment or magnetic moment.* Spin angular momentum $\vec{J}$ and magnetic moment vectors $\vec{\mu}$ are related such that

$$\vec{\mu} = \gamma \vec{J} \tag{1.1}$$

where γ is a nucleus-dependent physical constant called *gyromagnetic ratio.* Although the magnitude of $\vec{\mu}$ is constant under any conditions, its direction is completely random in the absence of an external field. In order to activate macroscopic magnetism from an object, it is necessary to line up the spin vectors. In conventional MRI, this is accomplished by a strong homogeneous one directional external magnetic field of strength B_0.

$$\vec{B_0} = B_0\vec{k} \tag{1.2}$$

where $\vec{k}$ is the unit vector in z direction. According to mechanics, the torque that $\vec{\mu}$ experiences from the external magnetic field is given by $\vec{\mu} \times B_0\vec{k}$ which is equal to rate of change of its angular momentum.

$$\frac{d\vec{J}}{dt} = \vec{\mu} \times B_0\vec{k} \tag{1.3}$$

It is concluded that the angular frequency of nuclear precession is

$$w_0 = \gamma B_0 \tag{1.4}$$

which is known as Larmor frequency and precession of $\vec{\mu}$ about $\vec{B_0}$ is clockwise if observed against the direction of the magnetic field [37]. In order for the spins to produce signals, they should be flipped onto the transverse plane. This is performed by a rotating RF field, which is perpendicular to the main magnetic field. For conventional MRI, main magnetic field is in the z direction. Therefore, the effective RF excitation field is modeled as a field oscillating on the transverse plane in clockwise direction perpendicular to the main field:

$$\vec{B_1}(t) = B_1^e(t)[\cos(w_{rf}t + \varphi)\vec{i} - \sin(w_{rf}t + \varphi)\vec{j}] \tag{1.5}$$

where $B_1^e(t)$ is the envelope function, w_{rf} is the carrier frequency and φ is the initial phase angle [37].

The resonance condition for the RF field is that it should rotate in the same manner as the precessing spins, in other words

$$w_{rf} = w_0 \tag{1.6}$$

When *Bloch Equation* for the rotating frame is considered [37] under the assumption that the duration of the RF pulse is short compared to T_1 and T_2

relaxation times, the motion of the bulk magnetization can be expressed as

$$\frac{\partial \vec{M}}{\partial t} = \gamma \vec{M}_{rot} \times B_1^e(t)\vec{i} \tag{1.7}$$

where $\vec{M}_{rot}$ is the magnetization vector in rotating frame of reference and γ is the gyromagnetic ratio.

Under initial conditions $M_{x'}(0) = 0$, $M_{z'}(0) = 0$, $M_{z'}(0) = M_z^0$, magnetization vector components at time t can be expressed as

$$M_{x'}(t) = 0 \tag{1.8}$$

$$M_{y'}(t) = M_z^0 \sin\alpha \tag{1.9}$$

$$M_{z'}(t) = M_z^0 \cos\alpha \tag{1.10}$$

where

$$\alpha = \int_0^t \gamma B_1^e(\widehat{t})d\widehat{t} \tag{1.11}$$

If a rectangular RF pulse of duration τ_p is considered, the *flip angle* is

$$\alpha = \gamma B_1 \tau_p \tag{1.12}$$

which indicates that the flip angle of the magnetization vector is determined by the duration and strength of the RF pulse. If a linear relation is assumed between the flip angle and the RF field strength, which is known as small flip angle approximation [38], then the flip angle of the spins resonating with w of deviation from w_{rf} is

$$\alpha(w) = \frac{F\{B_1^e(t)\}(w)}{F\{B_1^e(t)\}(0)}\alpha(0) \tag{1.13}$$

If a rectangular RF pulse of duration τ_p is considered, spins resonating at a frequency range of $|w - w_{rf}| < \frac{2\pi}{\tau_p}$ are excited by the RF pulse. This indicates that rectangular pulses with long duration are more selective.

Gradient fields, which are special kinds of inhomogeneous fields that provide linearly varying magnetic fields along a specific direction, are used to select slices to be excited and to localize spatial data by frequency and phase encodings. In conventional MRI three gradient coils are used in order to provide varying magnetic fields along x, y and z directions, which make it possible to excite or localize objects point wise in 3D space.

The main idea in the application of homogeneous main magnetic field and linearly varying gradient fields in conventional MRI is to align all spins in a controlled manner and vary the precession frequencies with a known, linearly changing, controlled inhomogeneity so that spins within slices, strips or points of a three dimensional object can be discriminated with a relation between precession frequency and spatial location.

1.2 Objectives of the Thesis

Objectives of this study are listed as follows:

- Determine four arbitrary surfaces which the RF coil is going to be produced on.
- Model an inhomogeneous main magnetic field and determine the RF field that is desired to be generated by the coil based on the main field.
- Model the current density and magnetic field relations in the form of Fredholm integral equations and use inverse approach to obtain current density distributions on each selected surface.
- Discretize the current density distribution to solve the problem as a matrix equation and use four different regularization techniques to match the generated magnetic field and the desired magnetic field.
- Obtain current flow paths for each surface selection and regularization technique using stream functions.
- Calculate the error percentage between the generated and desired magnetic field for each surface selection and regularization technique.

- Compare the error percentages and current flow paths and determine the optimum surface and regularization technique so that the error percentage is minimum and the current path is realizable.
- Fabricate the optimum planar coil and measure the magnetic field produced by the coil.
- Simulate the required circuitry to tune and match the coil to operate at 6.378 MHz in order to be used in 0.15 $Tesla$ METU MRI system.

1.3 Outline of the Thesis

A short introduction on existing MRI modalities and a brief background of MRI principles is presented in Chapter 1. The theory of the methods used in order to determine the RF coil structure is presented in Chapter 2. The implementation of the methods represented in Chapter 2 is presented in Chapter 3 for the RF coil design problem in inhomogeneous main field using various target and source field definitions. The experiments carried out based on the simulations and the results of these experiments and simulations are discussed in Chapter 4.

CHAPTER 2

RF Coil Design in Inhomogeneous Main Fields Using Method of Moments

This chapter presents the relation between current density and magnetic field using Maxwell equations and techniques for reducing functional equations to matrix equations using method of moments. Regularization methods are introduced in order to solve ill-conditioned matrix equations formed by method of moments. Finally, stream functions are represented, which are used to determine current paths for current density solution.

2.1 Method of Moments (MoM)

MoM is used to provide a unified treatment of matrix methods for computing the solutions to field problems. The basic idea is to reduce a functional equation to a matrix equation, and then solve the matrix equation by known techniques. These concepts are best expressed as linear spaces and operators [39]. For this study, inhomogeneous type of equations,

$$L(f) = g \tag{2.1}$$

are considered, where L is a linear operator, g is the source or excitation (known function), and f is the field or response (unknown function to be determined). By the term deterministic we mean that the solution to (2.1) is unique; that is, only one f is associated with a given g. A problem of analysis involves the determination of f when L and g are given. A problem of synthesis involves a determination of L when f and g are specified. In this study we consider only the analysis problem.

2.1.1 A General Solution Procedure

Consider the inhomogeneous equation 2.1. Let f be expanded in a series of functions f_1,f_2, f_3, ... in the domain of L, as

$$f = \sum_n \alpha_n f_n \tag{2.2}$$

where α_n are constants. f_n are called *expansion functions* or *basis functions.* For exact solutions, 2.2 is usually an infinite summation and the f_n form a complete set of basis functions. For approximate solutions, 2.2 is usually a finite summation. Substituting 2.2 in 2.1, and using the linearity of L, we have

$$L(f) = \sum_n \alpha_n L(f_n) = g \tag{2.3}$$

It is assumed that a suitable inner product $\langle f, g\rangle$ has been determined for the problem. Now define a set of *weighting functions*, or *testing functions* w_1,w_2, w_3, ... in the range of L, and take the inner product of 2.3 with each w_m. The result is

$$L(f) = \sum_n \langle w_m, \alpha_n L f_n\rangle = \langle w_m, g\rangle \tag{2.4}$$

where m=*1, 2, 3, ...*. This set of equations can be written in matrix form as

$$[T_{mn}][\alpha_n] = [g_m] \tag{2.5}$$

where

$$[T_{mn}] = \begin{bmatrix} \langle w_1, Lf_1 \rangle & \langle w_1, Lf_2 \rangle & ... & \langle w_1, Lf_n \rangle \\ \langle w_2, Lf_1 \rangle & \langle w_2, Lf_2 \rangle & ... & \langle w_2, Lf_n \rangle \\ \vdots & \vdots & \ddots & \vdots \\ \langle w_m, Lf_1 \rangle & \langle w_m, Lf_2 \rangle & ... & \langle w_m, Lf_n \rangle \end{bmatrix} \tag{2.6}$$

$$[\alpha_n] = \begin{bmatrix} \alpha_1 \\ \alpha_2 \\ \vdots \\ \alpha_n \end{bmatrix} \tag{2.7}$$

$$[g_m] = \begin{bmatrix} \langle w_1, g \rangle \\ \langle w_2, g \rangle \\ \vdots \\ \langle w_m, g \rangle \end{bmatrix} \tag{2.8}$$

If the matrix $[T]$ is nonsingular its inverse $[T^{-1}]$ exists. The α_n are then given by

$$[\alpha_n] = [T_{mn}^{-1}][g_m] \tag{2.9}$$

and the solution for f is given by 2.2.

2.2 Maxwell Relations

The four differential equations that are valid in every point in space for linear, non-magnetic, isotropic medium are

$$\nabla \times \vec{E} = -\frac{\partial \vec{B}}{\partial t} \tag{2.10}$$

$$\nabla \times \vec{H} = \vec{J}_s + \frac{\partial \vec{D}}{\partial t} \tag{2.11}$$

$$\nabla \cdot \vec{D} = \rho \tag{2.12}$$

$$\nabla \cdot \vec{B} = 0 \tag{2.13}$$

which are called *Maxwell equations* [40] and where

$$\vec{D} = \varepsilon \vec{E} \tag{2.14}$$

$$\vec{B} = \mu \vec{H} \tag{2.15}$$

$$\vec{J} = \sigma \vec{E} \tag{2.16}$$

The magnetic field $\vec{B}$ can be expressed in terms of a vector potential,

$$\vec{B} = \nabla \times \vec{A} \tag{2.17}$$

due to the identity $\nabla \cdot (\nabla \times \vec{A}) = 0$ using equation 2.13. Combining equations 2.11, 2.14, 2.15, 2.16 and 2.17 yields

$$\nabla \times \nabla \times \vec{A} = \mu\sigma\vec{E} + \mu\varepsilon\frac{\partial \vec{E}}{\partial t} - \mu\vec{J}_s \tag{2.18}$$

Combining equations 2.10 and 2.17 yields

$$\nabla \times \left(\vec{E} + \frac{\partial \vec{A}}{\partial t} \right) = 0 \tag{2.19}$$

and the electric field can be expressed as

$$\vec{E} = -\nabla\phi - \frac{\partial \vec{A}}{\partial t} \tag{2.20}$$

Using the identity $\nabla \times (\nabla\phi) = 0$, where ϕ constitutes for the potential function in equation 2.20, substituting equation 2.20 into 2.18 and using the identity $\nabla \times \nabla \times \vec{A} = \nabla \cdot (\nabla \cdot \vec{A}) - \nabla^2 \vec{A}$,

$$\nabla \cdot \left(\nabla \cdot \vec{A}\right) - \nabla^2 \vec{A} = \nabla \left[- \left(\mu\sigma\phi + \mu\varepsilon \frac{\partial \phi}{\partial t} \right) \right] - \mu\sigma \frac{\partial \vec{A}}{\partial t} - \mu\varepsilon \frac{\partial^2 \vec{A}}{\partial t^2} \tag{2.21}$$

If we choose Lorenz gauge valid for uniform medium

$$\nabla \cdot \vec{A} = - \left(\mu\sigma\phi + \mu\varepsilon \frac{\partial \phi}{\partial t} \right) \tag{2.22}$$

equation 2.21 takes the form

$$\nabla^2 \vec{A} - \mu\sigma \frac{\partial \vec{A}}{\partial t} - \mu\varepsilon \frac{\partial^2 \vec{A}}{\partial t^2} = -\mu \vec{J_s} \tag{2.23}$$

where $\vec{J_s}$ is the source current. If $\vec{A}$ has exponential characteristics (e^{jwt}), equation 2.23 can be expressed as,

$$\nabla^2 \vec{A} + k^2 \vec{A} = -\mu \vec{J_s} \tag{2.24}$$

where $k^2 = -jw\mu\,(\sigma + jw\varepsilon)$. Any vector field $\vec{A}$ generated by a volume current $\vec{J_s}$ through the vector Helmholtz equation 2.24 has a solution for uniform, unbounded medium:

$$\vec{A}(r) = \int_V \vec{J_s}(r') \frac{e^{-jk|r-r'|}}{4\pi\mu\,|r-r'|} dr' \tag{2.25}$$

where r is the field point vector and r' is the source point vector.

2.3 Combining MoM and Maxwell Relations

Four different geometries are considered for the source surface on which the RF coil pattern is planned to be designed. For all of the considerations, MoM is used to obtain the current density on the considered geometric surface and the coil pattern is formed utilizing stream functions [41].

Maxwell Equations form the basis for the implementation of MoM. In order to use MoM in the problem, magnetic flux density is expressed in terms of current density by substituting 2.25 into 2.17. An integral equation in the form of Fredholm Integral Equations

$$\int_{\Omega} K(x,x^{'})f(x^{'})dx^{'} = g(x), \qquad x \in \Omega \tag{2.26}$$

is obtained. For this expression, which is stated in only one direction, x, for the sake of simplicity

f (.) is the unknown function, which corresponds to the current density for the described problem.
K (. , .) is the Kernel of the integral equation, which corresponds to the relation between source and field points.
g (.) is the known or given function which is the magnetic flux density $\vec{B}$ for the described problem.

In order to convert the integral equation into a matrix equation, $f(x')$ is approximated using basis functions such that

$$f(x') \cong \sum_{j=1}^{N} \alpha_j f_j(x') \tag{2.27}$$

where $f_j(x')$ is the basis function for source point x' and α_j is the coefficient of the basis function $f_j(x')$. In equation 2.27, $f(x')$ only depends on the coordinate x' ; however, for the defined problem, $f(x')$; in other words, the current density is a function of x' , y' , z' . The choice of the basis and weight functions is explained in the *Chapter 3.*

When equation 2.27 is substituted into 2.26 the equality takes the form

$$\sum_{1}^{N} \alpha_j \int_{\Omega_j} f(x_j^{'}) K(x_i, x_j^{'})\, dx^{'} = g(x_i) \tag{2.28}$$

Equation 2.6 can be expressed as a matrix equation in the form,

$$\mathbf{A}\mathbf{x} = \mathbf{b} \tag{2.29}$$

where

$$\mathbf{x} = \begin{bmatrix} \alpha_1 \\ \alpha_2 \\ . \\ . \\ \alpha_N \end{bmatrix}_{N \times 1} \tag{2.30}$$

$$\mathbf{b} = \begin{bmatrix} g(x_1) \\ g(x_2) \\ . \\ . \\ g(x_{M-1}) \\ g(x_M) \end{bmatrix}_{M \times 1} \tag{2.31}$$

$$\mathbf{A} = \begin{bmatrix} f(x_1^{'})K(x_1, x_1^{'})dx' & f(x_2^{'})K(x_1, x_2^{'})dx' & \cdots & f(x_N^{'})K(x_1, x_N^{'})dx' \\ f(x_1^{'})K(x_2, x_1^{'})dx' & f(x_2^{'})K(x_2, x_2^{'})dx' \cdots & & f(x_N^{'})K(x_2, x_N^{'})dx' \\ \vdots & \ddots & & \\ f(x_1^{'})K(x_M, x_1^{'})dx' & & \cdots & f(x_N^{'})K(x_M, x_N^{'})dx' \end{bmatrix}_{M \times N} \tag{2.32}$$

where N and M are the number of source and field points respectively.

2.4 Regularization

In a wide sense, inverse problems are concerned with the task of finding the cause, given the effect.

A generic example of the inverse problem is the following: Let $\mathbf{A} : M \rightarrow N$ be a mapping between the sets, and suppose $\mathbf{b} \in N$. The problem is then to find $\mathbf{x} \in M$ such that $\mathbf{Ax} = \mathbf{b}$, or if no such $\mathbf{x}$ exists, such that $\mathbf{Ax} - \mathbf{b}$ is "small" in some sense.

A problem is referred to as ill–posed, in the sense that one or more of the following conditions are violated:

1. There exists some solution $\mathbf{x}$ (existence)
2. There is only one solution (uniqueness)
3. The solution depends continuously on the data $\mathbf{y}$ (stability)

On the other hand, if all three conditions hold for a particular inverse problem, the problem is referred to as well-posed. Fredholm Integral equations of the first kind (of type I) which take the following form for functions defined in the interval [0, 1]:

$$\int_0^1 k(s,t)x(t)\,dt = y(s) \qquad ,0 \leq s \leq 1 \tag{2.33}$$

are usually ill-posed problems [42].

A function $f : G \rightarrow H$ mapping elements in a linear space (a vector space) G into a linear space H is called linear if we have $f(\alpha x + \beta y) = \alpha\, f(x) + \beta\, f(y)$ for all $x,\, y \in G \quad and \quad \alpha,\, \beta \in R$. Let G and H be Euclidean spaces, such that $f : R^m \rightarrow R^n$ for some integers $m,\, n > 0$. Then there exists a matrix $\mathbf{A} \in R^{m,n}$ such that $f(x) = \mathbf{Ax}$ for all $\mathbf{x} \in R^n$. Suppose we have the linear rather relationship $\mathbf{Ax} = \mathbf{b}$ between the vectors $\mathbf{b} \in R^m$ and $\mathbf{x} \in R^n$ where

$\mathbf{x}$ might represent parameters of a physical system or the input to the system, $\mathbf{A}$ is the transformation performed by the system on the input and $\mathbf{b}$ is the output from the system.

The problem of computing $\mathbf{b}$ when $\mathbf{A}$ and $\mathbf{x}$ are given, is an example of a *forward* problem which obviously has only one solution. Since the relationship between $\mathbf{x}$ and $\mathbf{b}$ is linear, the right hand side b is a continuous function of $\mathbf{x}$. Thus, the solution is stable in the sense that small changes in $\mathbf{x}$ will result in small changes in $\mathbf{b}$. Theoretically, this problem is therefore well-posed. If $\mathbf{A}$ is ill-conditioned, the direct problem may still be ill-posed in a weaker sense. In this case, regularization may be applied.

Suppose $\mathbf{A}$ and $\mathbf{b}$ are known and $\mathbf{x}$ is to be determined. Here, x is only implicitly given by the equation $\mathbf{Ax} = \mathbf{b}$, hence this is an inverse problem. Existence and uniqueness of the solution is only guaranteed under certain assumptions. The simplest case arises when $rank(\mathbf{A}) = p = n$ and therefore $\mathbf{A}$ is invertible. The inverse problem is then obviously also well-posed in theory. If $\mathbf{A}$ is not invertible, we see that a solution exists if and only if $\mathbf{b}$ is an element of the range space, $\mathbf{b} \in \Re(A)$ and the solution is unique if and only if null space of $\mathbf{A}$ is an empty set, $N(A) = \{0\}$. Furthermore, when a unique solution exists it is only stable if $\Re(\mathbf{A}) = R^n$ (implying that $\mathbf{A}$ is invertible) [42].

There are three possible scenarios [43]:

1. The system is full rank; i.e., the number of equations equals the number of unknowns. In this case, there is only one solution which is given by

$$\hat{\mathbf{x}} = \mathbf{A}^{-1}\mathbf{b} \tag{2.34}$$

2. The matrix $\mathbf{A}$ has more rows than columns; i.e., there are more equations than unknowns. An exact solution for the system does not exist, so this problem is solved in the mean square sense. The solution is chosen to be the

vector x that satisfies the least squares equation

$$\hat{\mathbf{x}} = \arg\min_{x} \| \mathbf{b} - \mathbf{A}\mathbf{x} \|_2^2 \tag{2.35}$$

Recall that $\mathbf{x}$ is a least squares solution if and only if the *normal equations*

$$\mathbf{A}^T (\mathbf{b} - \mathbf{A}\mathbf{x}) = 0 \tag{2.36}$$

are satisfied. This means that the error $(\mathbf{b} - \mathbf{A}\mathbf{x})$ in the approximation is in the subspace $N\left(\mathbf{A}^T\right)$. Geometrically, the least squares solution $\mathbf{x}$ is the orthogonal projection of $\mathbf{b}$ into $\Re(\mathbf{A})$. Provided $N(\mathbf{A}) = \{0\}$ there is a unique least squares solution given by

$$\hat{\mathbf{x}} = (\mathbf{A}^T\mathbf{A})^{-1}\mathbf{A}^T\mathbf{b} \tag{2.37}$$

3. The matrix $\mathbf{A}$ has more columns than rows; i.e., there are more unknowns than equations. There are infinitely many solutions for this type of system, which is also solved in a mean square sense. The solution $\hat{\mathbf{x}}$ is chosen to be the minimum energy solution to the least squares equation, which is also the solution to cases 2.33 and 2.34 and is given by

$$\hat{\mathbf{x}} = \arg\min_{x} \|\mathbf{x}\|_2^2 \ \textit{subject to} \ \min \|\mathbf{b} - \mathbf{A}\mathbf{x}\|_2^2 \tag{2.38}$$

The superior numerical tools for analysis of rank-deficient and discrete ill-posed problems are Singular Value Decomposition (SVD) of $\mathbf{A}$ and its generalization to two matrices, the generalized SVD (GSVD) of the matrix pair (A, L) . The SVD reveals all the difficulties associated with the ill-conditioning of the matrix $\mathbf{A}$, while GSVD of $(\mathbf{A}, \mathbf{L})$ yields important insight into the regularization problems involving both the matrix $\mathbf{A}$ and the regularization matrix $\mathbf{L}$.

2.4.1 The Idea of Regularization

Most regularization methods produce an estimate of the form

$$\mathbf{x} = \mathbf{V}\mathbf{F}\mathbf{D}^{-1}\mathbf{U}^T\mathbf{b} = \sum_{i=1}^{n} f_i \frac{\langle u_i, b\rangle}{\sigma_i} v_i \tag{2.39}$$

The matrices $\mathbf{V}$, $\mathbf{D}$, $\mathbf{U}$ are the matrices obtained by the SVD of $\mathbf{A}$. There is an additional scale factor f_i for each term in the sum. These factors usually satisfy $0 \leq f_i \leq 1$, corresponding to the notion that regularization down weights or filters out some of the directions v_i , usually those that are associated with smaller singular values σ_i . The diagonal matrix $\mathbf{F}$ which is composed of the diagonal elements $f_1, f_2, \ldots f_n$, completely characterizes the filtering properties of the regularization method. The matrix $\mathbf{A}^{\#} = \mathbf{V}\mathbf{F}\mathbf{D}^{-1}\mathbf{U}^T$ is called the regularization matrix, as we have $\mathbf{x} = \mathbf{A}^{\#}\mathbf{b}$ [42].

2.5 Stream Functions

The definition of a streamline is the line everywhere tangential to the local fluid velocity, i.e., the solution of

$$\frac{dx}{u} = \frac{dy}{v} = \frac{dz}{w} \tag{2.40}$$

where u, v and w are the speeds of the fluid in x, y and z directions respectively. It has been shown that, in order to construct accurate streamlines, mass conservation must be maintained. This means that the divergence of the fluid momentum must be zero [44]

$$\nabla \cdot (\rho \vec{F}) = 0 \tag{2.41}$$

where ρ is the fluid density and $\vec{F}$ is the fluid velocity.

The stream function was first introduced by Lagrenge to describe two-dimensional incompressible flow ($\nabla \cdot \vec{F} = 0$). This condition allows $\vec{F}$ to be described as the curl of a vector potential with a single component ψ in perpendicular direction to the surface where $\vec{F}$ is defined [41]. The function ψ is the stream function, and it is related to vector field through the equation

$$\vec{F} = \nabla \times \psi \vec{n} \tag{2.42}$$

where $\vec{n}$ is the unit vector perpendicular to the surface on which $\vec{F}$ is defined. Equation 2.42 yields the following relation for cartesian coordinates between the stream function and vector field which has two normal components $u\vec{a}_x$ and $u\vec{a}_y$ on xy-plane:

$$\begin{aligned} u &= \frac{\partial \psi}{\partial y} \\ v &= \frac{-\partial \psi}{\partial x} \end{aligned} \tag{2.43}$$

It can be seen that 2.43 can be arranged to obtain

$$udy - vdx = 0 \tag{2.44}$$

so that

$$d\psi = 0 \tag{2.45}$$

and ψ is constant along the streamline. This is an important result as it means that a streamline can be formed by computing contours of the scalar field ψ [45].

The stream function also has an important physical property which is related to the mass flow rate between two points in the flow field. Let us consider the vector field as an divergence free surface current density $\vec{J_s}$ on an arbitrary surface Ω. From the definition of the current density [40], the total current flowing through an arbitrary surface Ω is

$$I = \int_{\Omega} \vec{J} \cdot \vec{ds} \tag{2.46}$$

When dealing with the sheet current density $\vec{J_s}$, 2.46 can be modified to

$$I = \int_{\ell} \vec{J_s} \cdot \vec{dl} \tag{2.47}$$

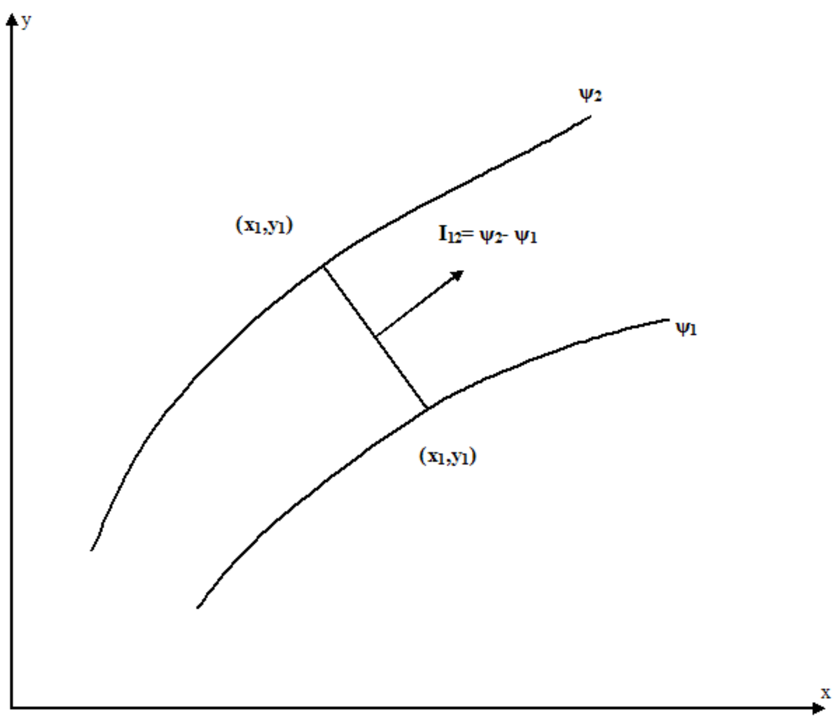

Figure 2.1: Equally spaced contours of ψ represent winding patterns with constant current in each streamline. The difference between the magnitude of ψ_2 at point (x_2, y_2) and the magnitude of ψ_1 at point (x_1, y_1) is equal to the magnitude of the current I_{12} flowing between the streamlines ψ_1 and ψ_2.

With the line integral split into smaller segments, the change in current across a segment is

$$I_{12} = \int_{l_1}^{l_2} \vec{J}_s \cdot \vec{n} dl \tag{2.48}$$

$$= \int_{l_1}^{l_2} u\delta y - v\delta x \tag{2.49}$$

$$= \int_{l_1}^{l_2} d\psi = \psi_2 - \psi_1 \tag{2.50}$$

This shows that a spatial change in the value of ψ corresponds to an equivalent change in the value of the current I and that contour plots of $\psi(x, y)$ will give the locations of discrete wires carrying equal currents.

It can be shown that streamlines, lines where $\psi = constant$, are everywhere parallel to the current sheet density vector $\vec{J}_s = J_x\vec{a}_x + J_y\vec{a}_y$. For $\nabla \cdot \vec{J}_s = 0$

$$\vec{J}_s = \frac{\partial\psi}{\partial y}\vec{a}_x - \frac{\partial\psi}{\partial x}\vec{a}_y \tag{2.51}$$

Any point on the curve $\psi = constant$ can be expressed in cartesian coordinates as

$$\vec{r} = x(s)\vec{a}_x - y(s)\vec{a}_y \tag{2.52}$$

where s is the arc length along the streamline curve. The unit vector to this streamline is

$$\vec{T} = \frac{d\vec{r}}{ds} = \frac{dx}{ds}\vec{a}_x + \frac{dy}{ds}\vec{a}_y \tag{2.53}$$

For the streamline $\psi(x(s), y(s)) = constant$, the chain rule yields

$$\frac{d\psi}{ds} = \frac{\partial\psi}{\partial x}\frac{dx}{ds} + \frac{\partial\psi}{\partial y}\frac{dy}{ds} \tag{2.54}$$

Using 2.51,

$$\frac{dy}{ds} = \frac{J_y}{J_x}\frac{dx}{ds} \tag{2.55}$$

Substituting 2.51 into, 2.53 gives the result:

$$\vec{T} = \frac{1}{J_x}\frac{dx}{ds}(J_x\vec{a}_x + J_y\vec{a}_y) \tag{2.56}$$

which means that current flow is parallel to the streamlines.

CHAPTER 3

Implementing the Coil Structure by Using Regularization Methods and Stream Functions

3.1 Defining the Required Magnetic Field

The main purpose of the algorithm defined in this report is to find a current density map on a pre-defined surface in order to create a specified magnetic field within a predefined volume. Therefore, magnetic field specification is one of the inputs that should be defined. As the aim of this work is to produce a coil that generates an RF field for an inhomogeneous main field, the characteristics of the RF field should also be determined with reference to the main magnetic field. In order to specify an RF field, first an inhomogeneous magnetic field is produced by a square coil placed on the $yz-plane$, within the pre-defined field volume as illustrated in 3.1 and for each field point, RF field components are specified based on the requirements related to this main field. The main magnetic field in the target volume that is considered as a reference to produce RF field is illustrated in Figure 3.1.

The first requirement on the RF field is that, the field produced by the coil should be perpendicular to the main magnetic field at every field point. In other words, if a single field point and the main field vector at this point are considered, then the RF field vector is defined on the plane which the main field vector is normal to.

For this requirement to be satisfied, the main magnetic field and the RF field are defined as:

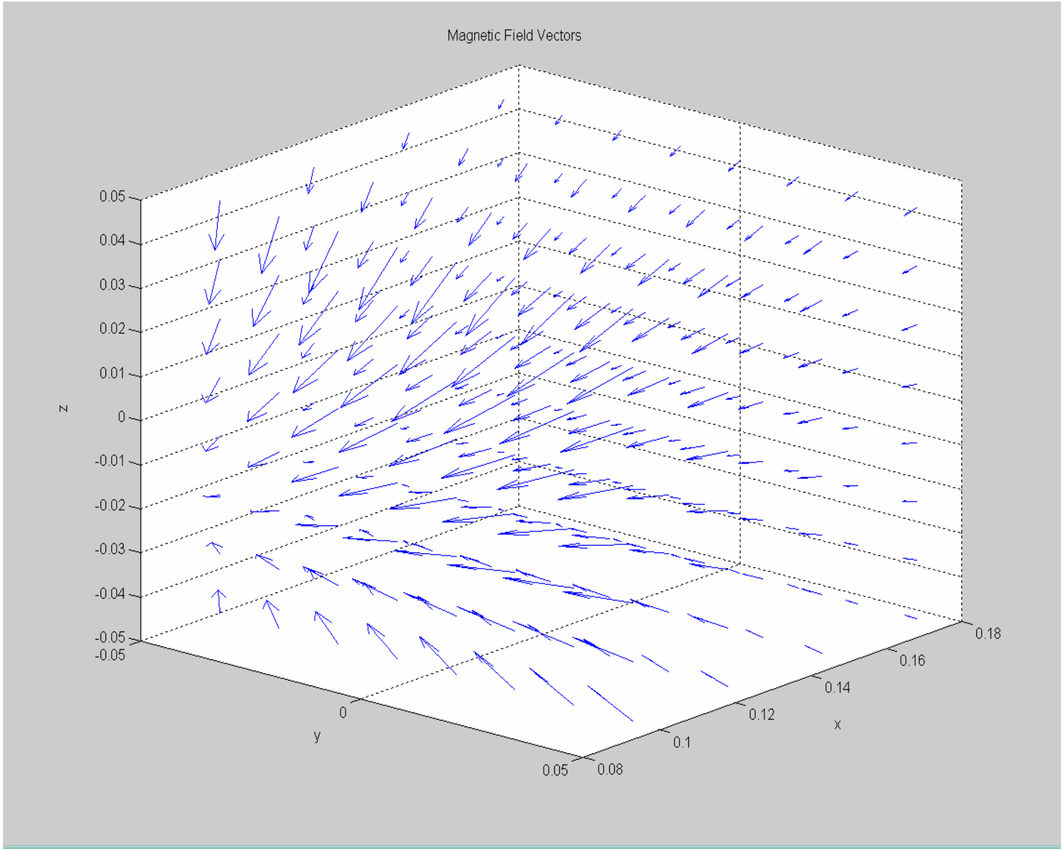

Figure 3.1: Main magnetic field Vectors in the field volume. A square wire of 10cm by 10cm is considered on yz-plane. The center of the square coil is at point (0,0,0) and the coil generates magnetic field vectors represented by the arrows of length proportional to the magnitudes at every field point.

$$\begin{aligned} \vec{B} &= B_x\vec{a}_x + B_y\vec{a}_y + B_z\vec{a}_z \\ \vec{B}_{rf} &= B_{rx}\vec{a}_x + B_{ry}\vec{a}_y + B_{rz}\vec{a}_z \end{aligned} \tag{3.1}$$

Then, the orthogonality principle, which is a preferred constraint for RF field determination, requires that

$$\vec{B} \cdot \vec{B}_{rf} = 0 \tag{3.2}$$

which results in the equality

$$B_x B_{rx}(t) + B_y B_{ry}(t) + B_z B_{rz}(t) = 0 \tag{3.3}$$

A second preferred constraint on the RF field is that, at every field point the magnitude of the field vector should be equal so that the spins at every field point is forced onto the transverse plane of the field vector at the same time. For this requirement to be satisfied:

$$\sqrt{B_{rx}^2 + B_{ry}^2 + B_{rz}^2} = m \tag{3.4}$$

where m is a non-zero real number.

In order to determine an RF field as the desired magnetic field, four different magnetic field characteristics are considered specifying different requirements.

3.1.1 RF Field Case 1

For these characteristics, only the first requirement is considered and the x and y components of the RF field are specified as:

$$B_{rx} = B_x \ \ and \ \ B_{ry} = B_y \tag{3.5}$$

From equation 3.3 it is determined that

$$B_{rz} = -\frac{B_x^2 + B_y^2}{B_z} \tag{3.6}$$

Using the main magnetic field B and the equations 3.5, 3.6, one of the possible RF field characteristics is determined as illustrated in Figure 3.2.

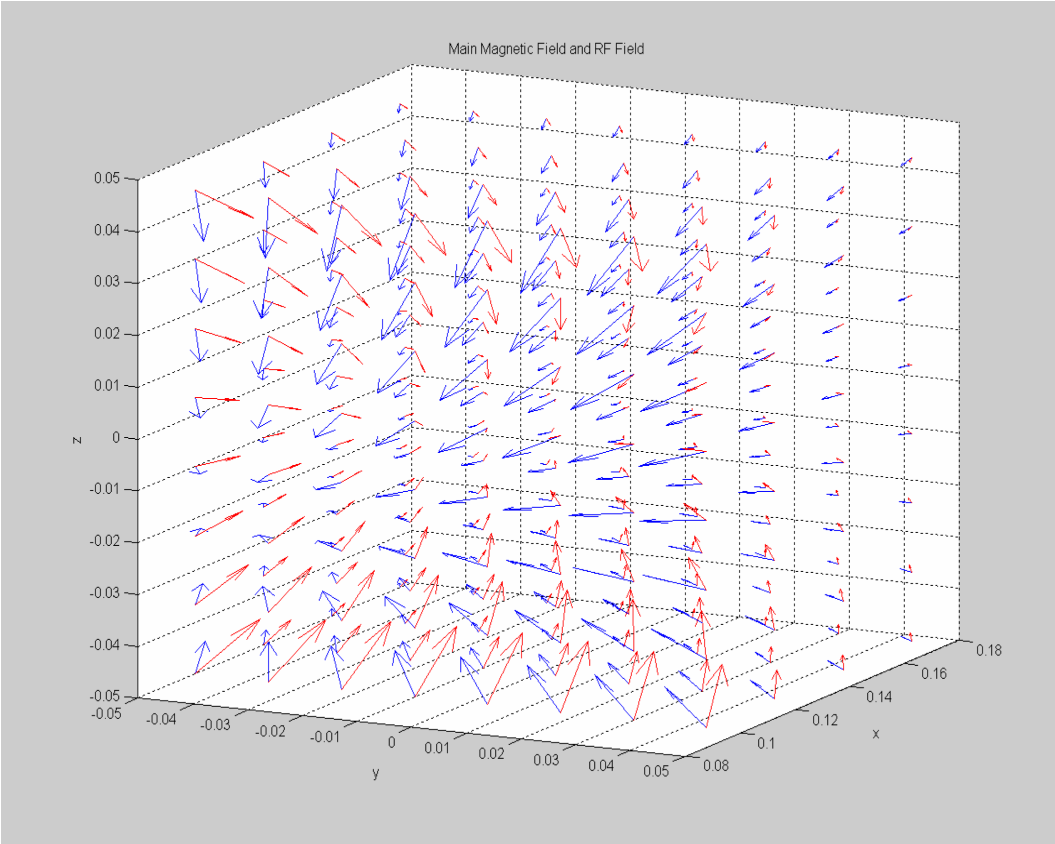

Figure 3.2: Main magnetic field and RF field vectors within the field volume for case 1. The main magnetic field vectors are illustrated as blue arrows, while RF field vectors are illustrated as red arrows.

3.1.2 RF Field Case 2

For this characteristics, both requirements are considered and y component of the RF field is specified as zero at all field points, so that the spin interactions are decreased as all spins will lie perpendicular to the y-axis when RF field is applied. Therefore, equation 3.4 takes the form:

$$B_{rx}^2 + B_{rz}^2 = m^2 \tag{3.7}$$

From 3.3,

$$B_{rx} = \frac{-B_{rz}B_z}{B_x} \tag{3.8}$$

If 3.8 is substituted in 3.7, it is found that

$$B_{rz} = \frac{|mB_x|}{\sqrt{B_x^2 + B_z^2}} \tag{3.9}$$

From 3.9,

$$B_{rx} = -\frac{|mB_x|}{B_x} \cdot \frac{B_z}{\sqrt{B_x^2 + B_z^2}} \tag{3.10}$$

And it is initially defined that

$$B_{ry} = 0 \tag{3.11}$$

Using the main magnetic field B and the equations 3.9, 3.10, 3.11; another possible RF field characteristics is determined as illustrated in Figure 3.3.

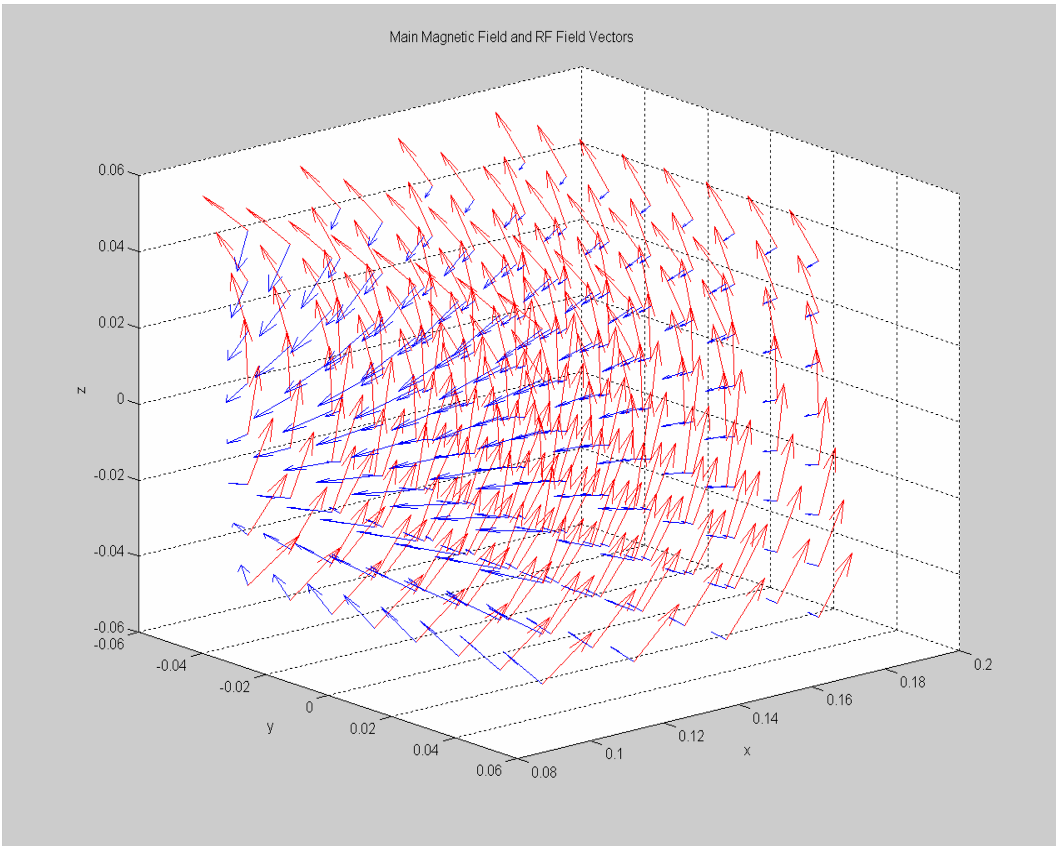

Figure 3.3: Main magnetic field and RF field vectors within the field volume for case 2. The main magnetic field vectors are illustrated as blue arrows, while RF field vectors are illustrated as red arrows.

3.1.3 RF Field Case 3

For this characteristics, both requirements are considered. Also it is specified that the component of the RF field on the xy-plane is in the same or opposite direction as the one of the main magnetic field. This requires:

$$\frac{B_{rx}}{B_{ry}} = \frac{B_x}{B_y} \tag{3.12}$$

Using equations 3.3 and 3.4,

$$B_{ry} = \mp \sqrt{\frac{m^2}{\frac{B_x^2+B_y^2}{B_y^2} + \frac{\left(B_x^2+B_y^2\right)^2}{B_y^2 B_z^2}}} \tag{3.13}$$

where the minus or plus sign determines whether the transverse components of the fields are in the same or opposite direction respectively.

$$B_{rx} = \frac{B_x}{B_y} B_{ry} \tag{3.14}$$

and

$$B_{rz} = -\frac{B_x^2 + B_y^2}{B_y B_z} B_{ry} \tag{3.15}$$

Using the main magnetic field B and the equations 3.13, 3.14, 3.15 ; another possible RF field characteristics is determined as illustrated in Figure 3.4.

3.1.4 RF Field Case 4

For this characteristics, both requirements are considered and it is specified that the y-component of the RF field is constant at all field points, so that it could be tested whether the regularization works better for such characteristics that is forced to be more homogeneous. For a constant y-component,

$$B_{ry} = a \tag{3.16}$$

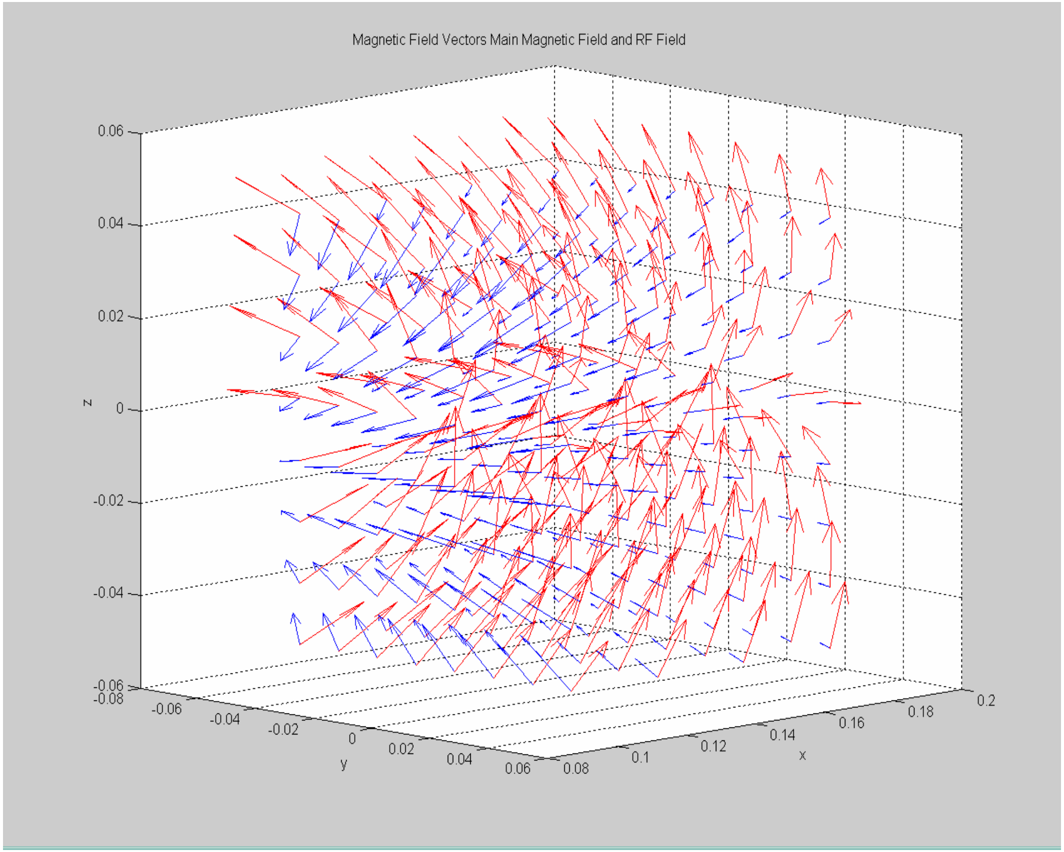

Figure 3.4: Main magnetic field and RF field vectors within the field volume for case 3. The main magnetic field vectors are illustrated as blue arrows, while RF field vectors are illustrated as red arrows.

where a is a positive real number. Combining 3.4 and 3.16,

$$B_{rx}^2 = m^2 - a^2 - B_{rz}^2 \tag{3.17}$$

and combining 3.3 and 3.17,

$$B_{rz} = \frac{-2aB_yB_z \mp \sqrt{4a^2B_y^2B_z^2 - 4\left(B_x^2 + B_z^2\right)\left(a^2B_y^2 + a^2B_x^2 - m^2B_x^2\right)}}{2\left(B_x^2 + B_z^2\right)} \tag{3.18}$$

And using 3.3,

$$B_{rx} = -\frac{mB_y + B_zB_{rz}}{B_x} \tag{3.19}$$

Using the main magnetic field B and the equations 3.16, 3.18, 3.19; another possible RF field characteristics is determined as illustrated in Figure 3.5.

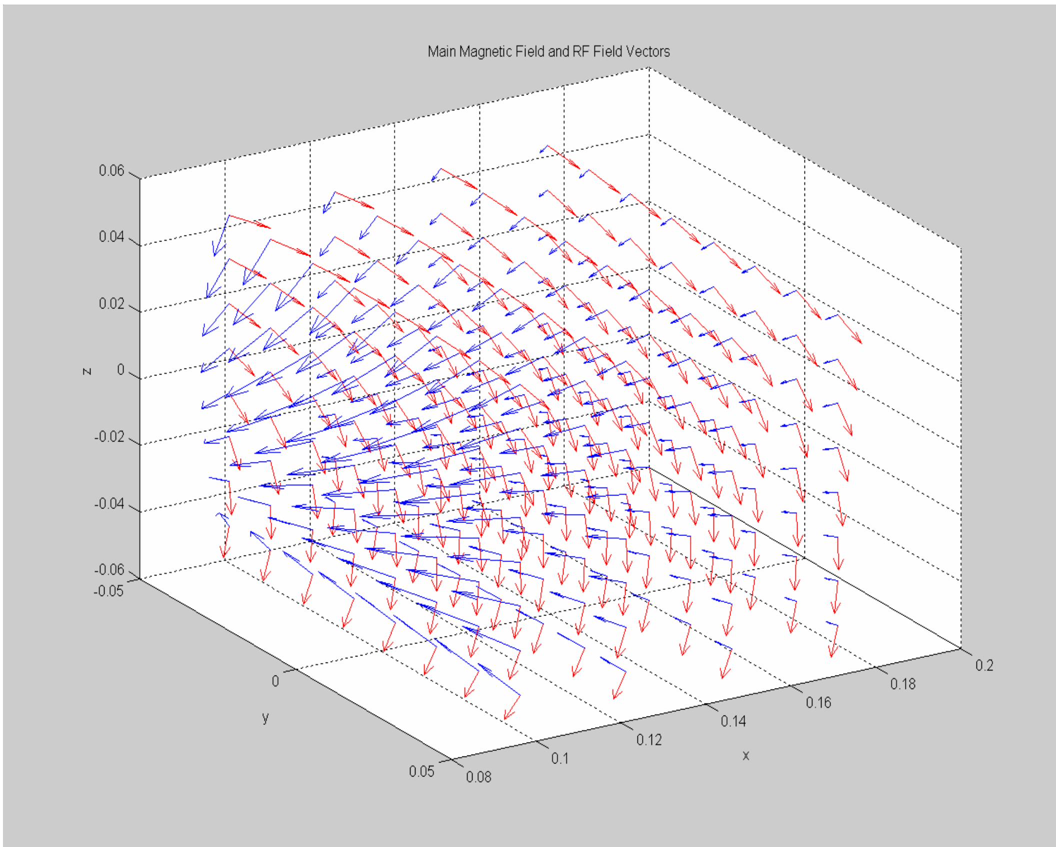

Figure 3.5: Main magnetic field and RF field vectors within the field volume for case 4. The main magnetic field vectors are illustrated as blue arrows, while RF field vectors are illustrated as red arrows. RF Field vector magnitudes are scaled by a factor of 0.5.

3.2 Defining Target and Source Fields

Four different geometries are considered as source fields where surface current density is defined. Target fields are defined as cubes with their centers placed at the origin. The problem definitions are named after the source field geometries on which the surface current density vectors are defined:

- Cylindrical Surface,
- Planar Surface,

- Tri-planar Surface and
- Orthogonal Three Planes

3.2.1 Cylindrical Source Surface

The required RF field is aimed to be generated within the cube at the origin by the surface current density vectors in angular and vertical directions defined on a cylinder of radius ρ_0 and length L which surrounds the target field. The source and target fields for this problem definition are illustrated in Figure 3.6.

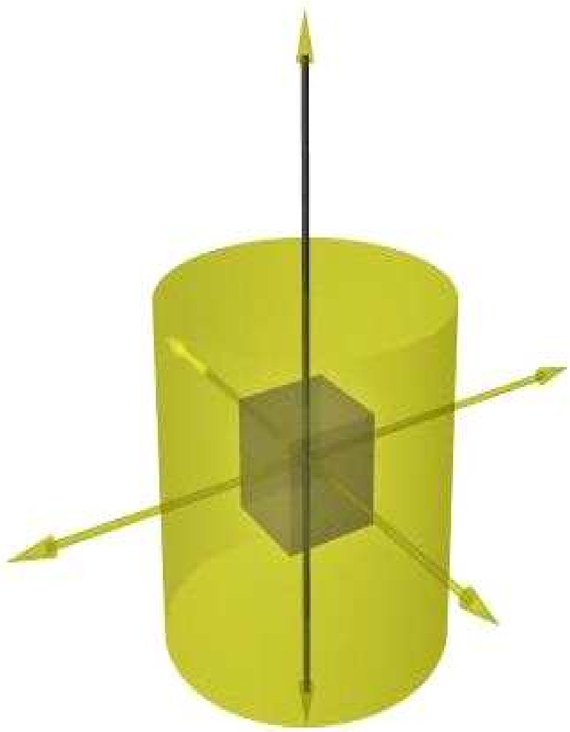

Figure 3.6: Target and source fields for cylindrical surface problem definition.The cube inside the cylinder is the target field while the cylindrical surface is the source field.

In order to carry out the MoM solution, the surface of the cylinder is divided into M longitudinal and N angular pieces forming $M \times N$ subdomains. The mapping of cylinder surface into two dimensional grid structure is illustrated in Figure 3.7.

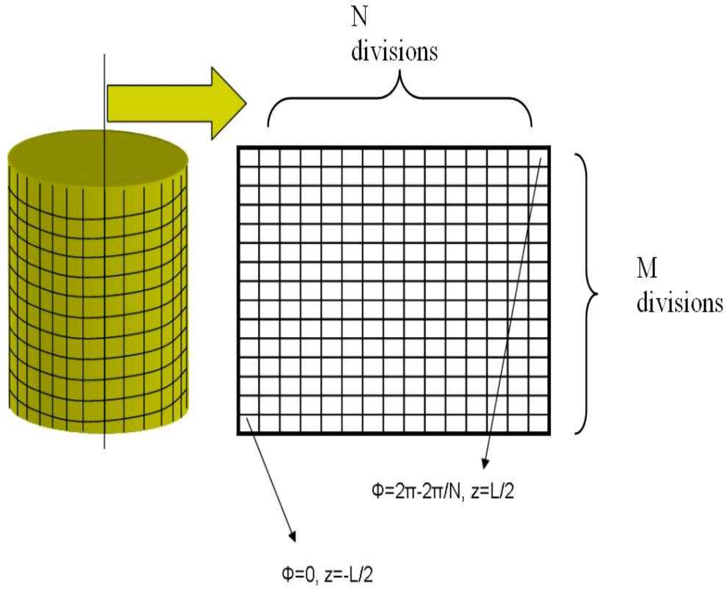

Figure 3.7: Spatial mapping of cylinder surface coordinates onto subdomains.

3.2.2 Tri-Planar Source Surface

The required RF field is aimed to be generated within the cube at the origin by the surface current density vectors on a geometry formed by three planes, one of which is placed parallel to $yz - plane$ and the remaining two parallel to each other and $xz - plane$. This surface geometry has a total longitudinal length of L and a width of W. The source and target fields for this problem definition are illustrated in Figure 3.8.

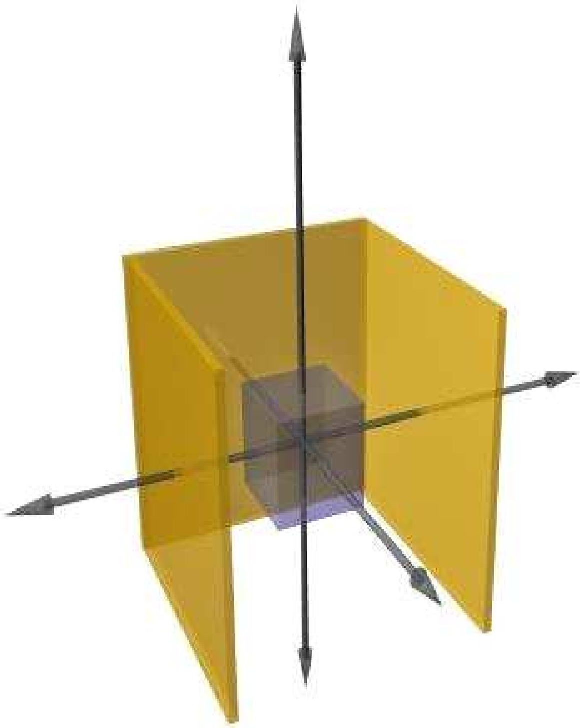

Figure 3.8: Target and source fields for tri-planar surface problem definition. The cube in front of the tri-planar geometry is the target field while the tri-planar surface is the source field.

In order to carry out the MoM solution, the surface is divided into M longitudinal and N angular pieces forming $M \times N$ subdomains. The mapping of surface into two dimensional grid structure is illustrated in Figure 3.9.

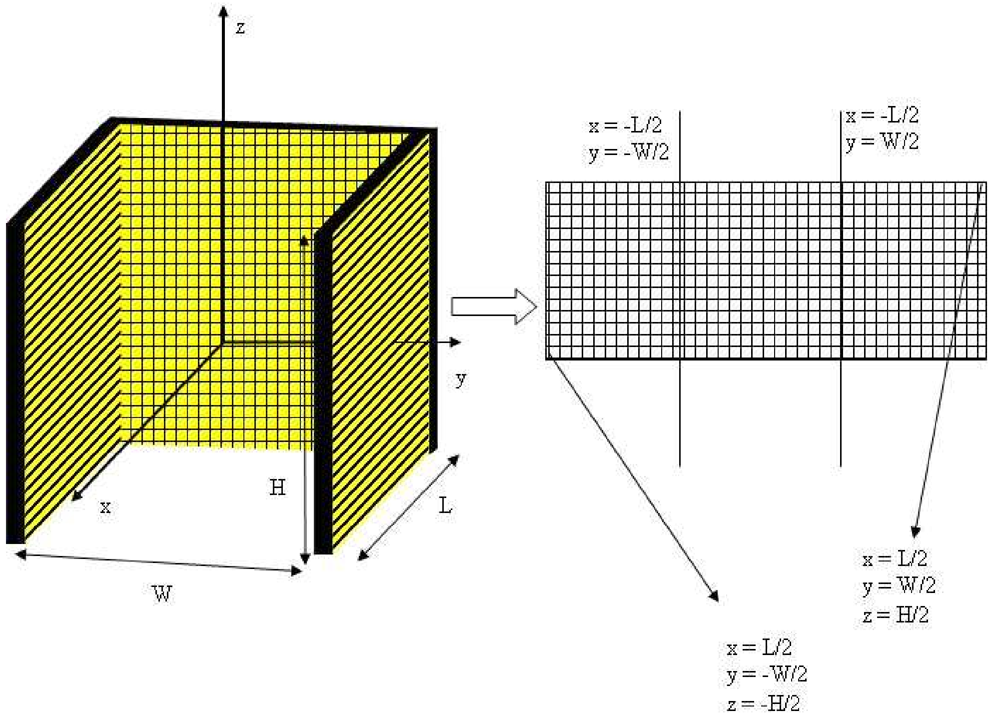

Figure 3.9: Spatial mapping of tri-planar surface coordinates onto subdomains.

3.2.3 Planar Source Surface

The required RF field is aimed to be generated within the cube at the origin by the surface current density vectors on a planar surface placed on $yz-plane$ of length L and width W. The source and target fields for this problem definition are illustrated in Figure 3.10.

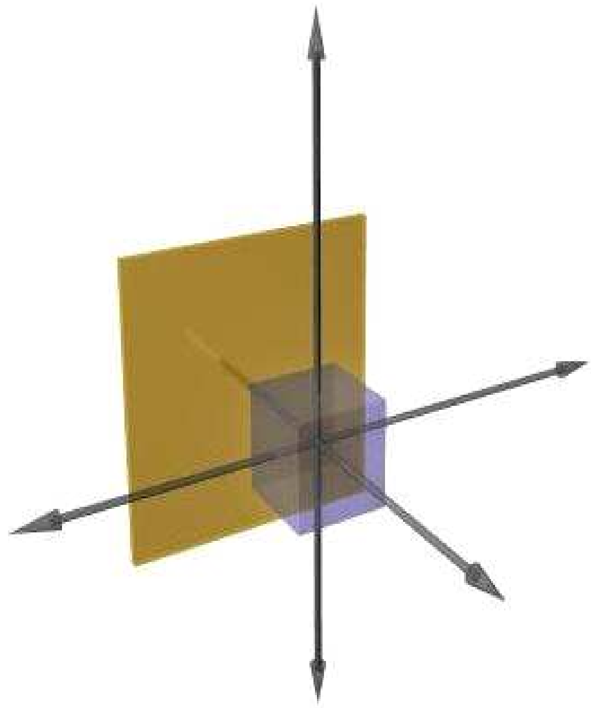

Figure 3.10: Target and source fields for planar surface problem definition.The cube in front of the planar geometry is the target field while the planar surface is the source field.

In order to carry out the MoM solution, the planar surface is divided into M pieces on $z-axis$ and N pieces on $y-axis$ forming $M \times N$subdomains.

3.2.4 Orthogonal Three Planes

The required RF field is aimed to be generated within the cube at the origin by the surface current density vectors on a geometry formed by three planes, that are placed on three different planes orthogonal to each other. As a definition of this problem, each plane acts as an independent planar surface that aims to generate one directional component of the required RF field, which is directed normal to the corresponding plane. Each planar surface geometry has a length and width equal to each other. The source and target fields for this problem definition are illustrated in Figure 3.11.

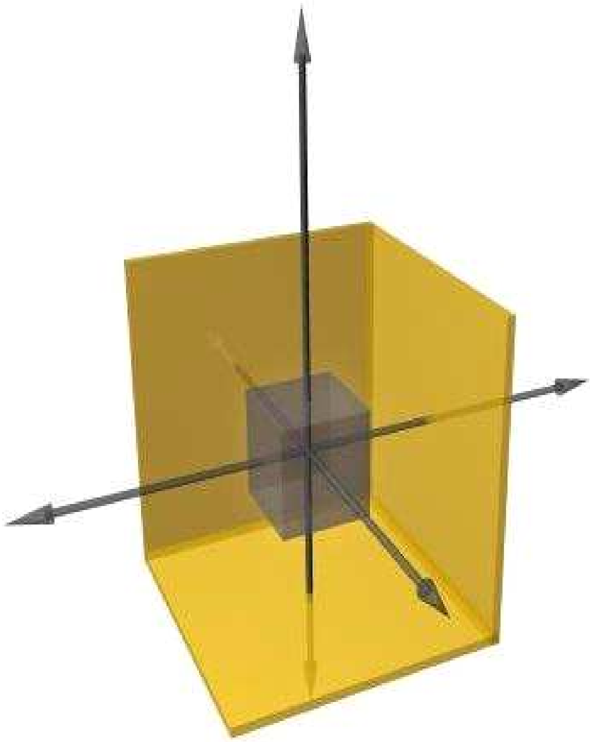

Figure 3.11: Target and source fields for orthogonal three planes problem definition.The cube in the middle of the three planes is the target field while the three orthogonal planes form the source field.

In order to carry out the MoM solution, each surface is divided into M longitudinal and N angular pieces forming $M \times N$ subdomains.

3.3 Defining the Basis Functions

When the defined geometries are divided into subdomains and mapped to two dimensional grid structure, the current density should be expressed in terms of basis functions for each subdomain in order to carry out Method of Moments procedure. While defining basis functions, the continuity of the current density between subdomains is a constraint. Fourier series are chosen in order to provide a continuous transition between the subdomains on the surface.

Also the behavior of the current density vectors on the boundaries of the surfaces should be able to be controlled by the basis function. Additional parameters are introduced to the Fourier series in order to control the function magnitude on the surface boundaries.

Two general basis function sets are defined for the current density vectors. The first definition is used for the cylindrical geometry while the second definition is used for planar geometries.

3.3.1 Basis Functions for Cylindrical Geometry

The basis functions used for current densities in angular and longitudinal directions on each subdomain of the surface are defined as follows:

$$\begin{aligned}
\vec{J}_\phi &= \sum_{q=0}^{1}\sum_{p=0}^{1}\sum_{h_1=1}^{H_1}\sum_{h_2=p+1}^{H_2} \alpha_{h_1 h_2 pq} \cos(h_1\phi + \frac{q\pi}{2}) \cos(k_h z + \frac{(2p-h_2)\pi}{2})\vec{a}_\phi \\
\vec{J}_z &= \sum_{q=0}^{1}\sum_{p=0}^{1}\sum_{h_1=1}^{H_1}\sum_{h_2=p+1}^{H_2} \beta_{h_1 h_2 pq} \sin(h_1\phi + \frac{q\pi}{2}) \sin(k_h z + \frac{(2p-h_2)\pi}{2})\vec{a}_z
\end{aligned} \tag{3.20}$$

where $k_h = \frac{(h_2-p)\pi}{L}$

The effect of the parameters used in the basis functions are listed in Table 3.1 and resulting function magnitudes for variation of these parameters are illustrated in Table 3.2 and Table 3.3. p and q are determined according to the basis function behavior on the boundaries of the surface.

Table 3.1: Parameters in the basis function definition for cylindrical surface

Parameter	Role in the basis function definition
p	Controls the vector magnitudes on z-boundaries.
q	Controls the vector magnitudes on ϕ-boundaries.
h_1	Harmonics of the basis functions specifying ϕ dependence of the basis functions. Controls the symmetry conditions on $\phi = \pi$ axis.
h_2	Harmonics of the basis functions specifying z dependence of the basis functions. Controls the symmetry conditions on z = 0 axis.

Table 3.2: Basis function characteristics for Cylindrical Surface varying p, q, H_1 and H_2 - 1

	p=0, q=0		p=0, q=1	
	J_ϕ	J_z	J_ϕ	J_z
H_1=1 H_2=1	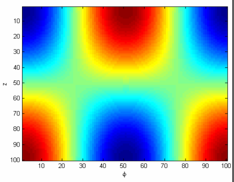	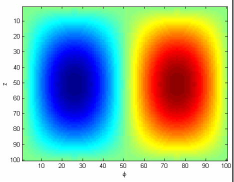	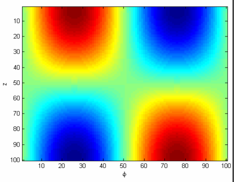	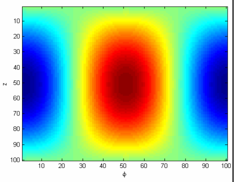
H_1=2 H_2=2	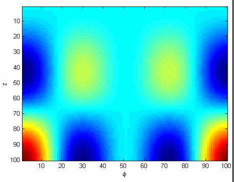	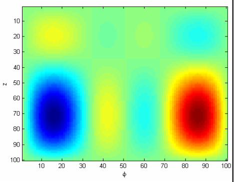	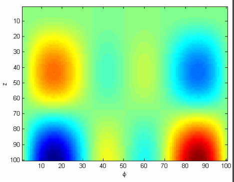	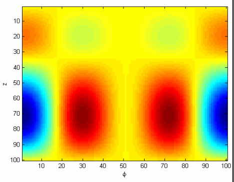
H_1=3 H_2=3	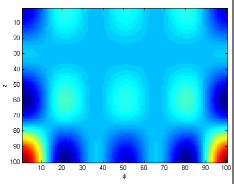	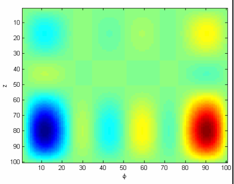	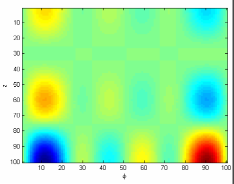	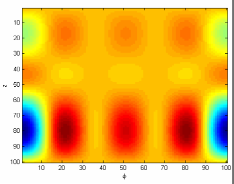
H_1=4 H_2=4	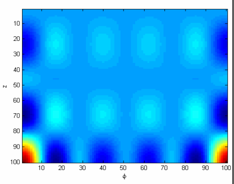	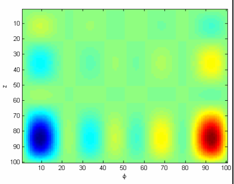	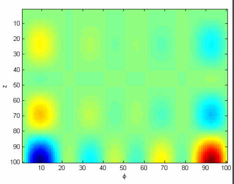	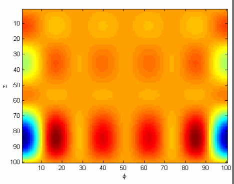

Table 3.3: Basis function characteristics for Cylindrical Surface varying p, q, H_1 and H_2 - 2

	p=1, q=0		p=1, q=1	
	J_ϕ	J_z	J_ϕ	J_z
H_1=2 H_2=2	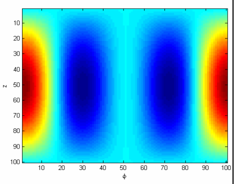	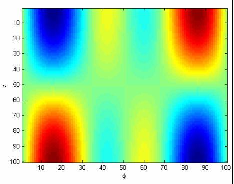	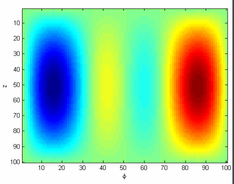	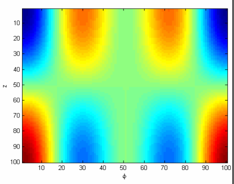
H_1=3 H_2=3	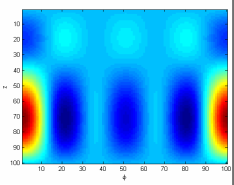	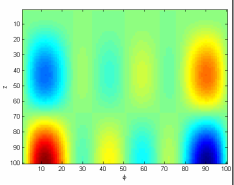	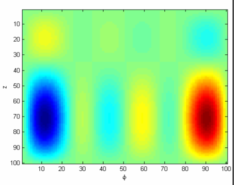	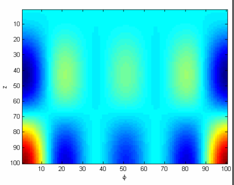
H_1=4 H_2=4	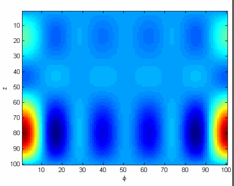	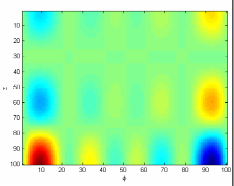	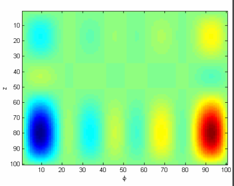	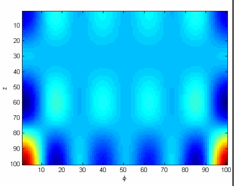

3.3.1.1 Stream Functions

The $\hat{a}_z$ and $\hat{a}_\phi$ sinusoidal terms spatially differ by 90^0 because this form gives a convenient description of the scalar functions and that fully describe the current density as a sum of a rotational (R) and irrotational (I) term:

$$\vec{J} = \vec{J}_\phi + \vec{J}_z = \vec{J}_R + \vec{J}_I \tag{3.21}$$

or in terms of scalar functions ψ and χ

$$\vec{J} = \vec{a}_\rho \times \nabla\chi + \nabla\Psi \tag{3.22}$$

such that

$$\psi \quad = \quad \sum_{q=0}^{1}\sum_{p=0}^{1}\sum_{h_1=1}^{H_1}\sum_{h_2=p+1}^{H_2} \gamma_{h_1 h_2 pq} \ \sin(\, h_1\phi + \frac{q\pi}{2}\,)\cos(\ k_h z + \frac{(2p-h_2)\pi}{2}\,)$$

$$\chi = \sum_{q=0}^{1}\sum_{p=0}^{1}\sum_{h_1=1}^{H_1}\sum_{h_2=p+1}^{H_2} \kappa_{h_1h_2pq}\cos(h_1\phi + \frac{q\pi}{2})\sin(k_hz + \frac{(2p-h_2)\pi}{2}) \tag{3.23}$$

where $\nabla = \frac{\partial}{\partial\phi}\vec{a}_\phi + \frac{\partial}{\partial z}\vec{a}_z$

If the coil structure is very small relative to the wavelength of operation, the current density $\vec{J}$ is purely rotational [33]. This situation is valid for low operating frequencies such as METU MRI system (6.387 MHz). Therefore, the current density is approximated without divergence. As current density function is purely rotational

$$\gamma_{h_1h_2pq} = 0 \quad and \quad \beta_{h_1h_2pq} = \frac{h_1\alpha_{h_1h_2pq}}{\rho_0k_h} \tag{3.24}$$

Therefore, current density functions can be rewritten as:

$$\begin{aligned}
\vec{J}_\phi &= \sum_{h_1=1}^{H_1}\sum_{h_2=1}^{H_2}\alpha_{h_1h_2}\cos(h_1\phi)\cos(k_hz - \frac{h_2\pi}{2})\vec{a}_\phi \\
\vec{J}_z &= \sum_{h_1=1}^{H_1}\sum_{h_2=1}^{H_2}\frac{h_1\alpha_{h_1h_2}}{\rho_0k_h}\sin(h_1\phi)\sin(k_hz - \frac{h_2\pi}{2})\vec{a}_z \\
\psi &= \sum_{h_1=1}^{H_1}\sum_{h_2=1}^{H_2} -\frac{\alpha_{h_1h_2pq}}{k_h}\sin(h_1\phi)\cos(k_hz - \frac{h_2\pi}{2})
\end{aligned} \tag{3.25}$$

where $k_h = \frac{h_2\pi}{L}, \quad (p = 0, q = 0)$

3.3.2 Basis Functions for Planar Geometries

A general form of Fourier series is used for planar geometries. The basis functions used for current densities on each subdomain of the surface are as follows:

$$
\begin{aligned}
\vec{J}_u &= \sum_{q=0}^{1}\sum_{p=0}^{1}\sum_{h_1=1}^{H_1}\sum_{h_2=1}^{H_2} \alpha_{h_1 h_2 pq} \cos(k_{h_1} u + \frac{q\pi}{2}) \cos(k_{h_2} v + \frac{p\pi}{2})\vec{a}_u \\
\vec{J}_v &= \sum_{q=0}^{1}\sum_{p=0}^{1}\sum_{h_1=1}^{H_1}\sum_{h_2=1}^{H_2} \beta_{h_1 h_2 pq} \sin(k_{h_1} u + \frac{q\pi}{2}) \sin(k_{h_2} v + \frac{p\pi}{2})\vec{a}_v
\end{aligned} \tag{3.26}
$$

where $k_{h_1} = \frac{h_1\pi}{l_u}$ and $k_{h_2} = \frac{h_2\pi}{l_v}$

The effect of the parameters used in the basis functions are listed in Table 3.4 and resulting function magnitudes for variation of these parameters are illustrated in Table 3.5 and Table 3.6. p and q are determined according to the basis function behavior on the boundaries of the surface.

Table 3.4: Parameters in the basis function definition for planar surfaces

Parameter	Role in the basis function definition
p	Controls the vector magnitudes on v-boundaries.
q	Controls the vector magnitudes on u-boundaries.
h_1	Harmonics of the basis functions specifying u dependence of the basis functions. Controls the symmetry conditions on u= $l_u/2$ axis.
h_2	Harmonics of the basis functions specifying v dependence of the basis functions. Controls the symmetry conditions on v = 0 axis.
l_u	Length of the surface in u direction.
l_v	Length of the surface in v direction.

Table 3.5: Basis function characteristics for planar geometries varying p, q, H_1 and H_2 - 1

	p=0, q=0		p=0, q=1	
	J_u	J_v	J_u	J_v
H_1=1 H_2=1	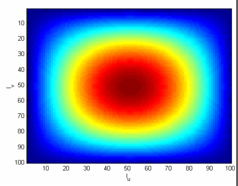	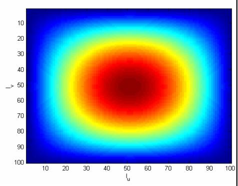	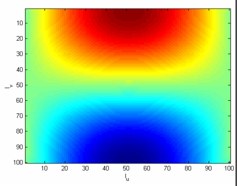	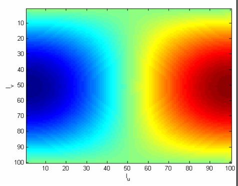
H_1=2 H_2=2	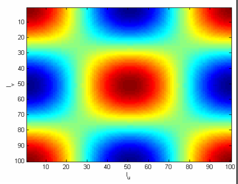	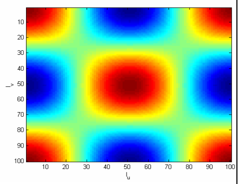	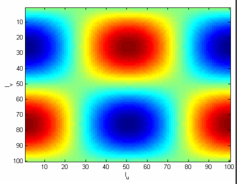	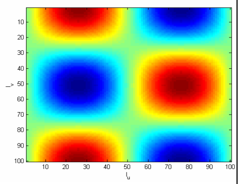
H_1=3 H_2=3	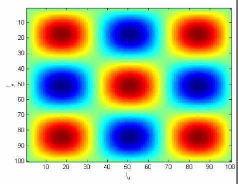	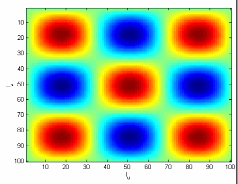	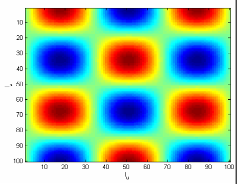	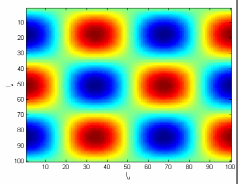
H_1=4 H_2=4	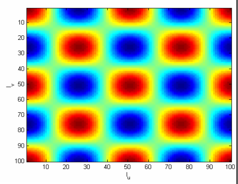	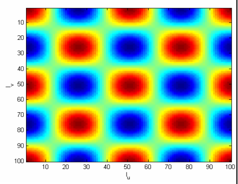	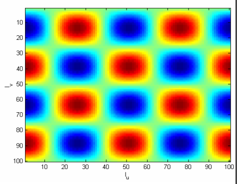	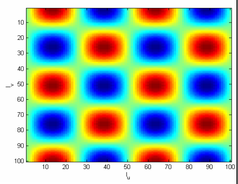

Table 3.6: Basis function characteristics for planar geometries varying p, q, H_1 and H_2 - 2

	p=1, q=0		p=1, q=1	
	J_u	J_v	J_u	J_v
H_1=1 H_2=1	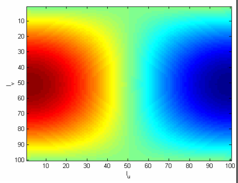	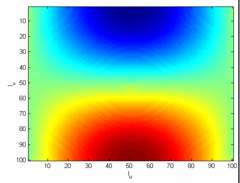	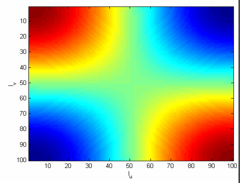	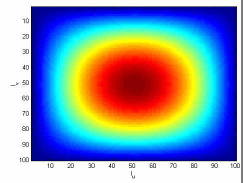
H_1=2 H_2=2	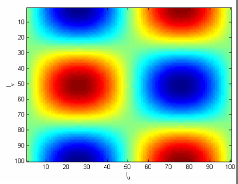	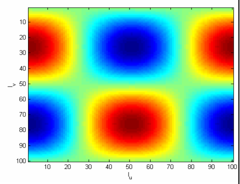	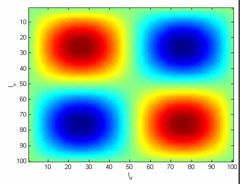	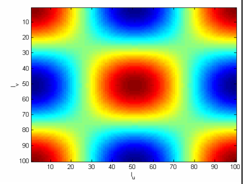
H_1=3 H_2=3	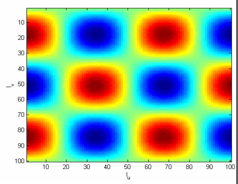	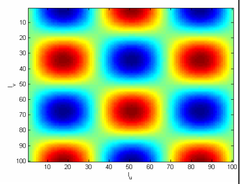	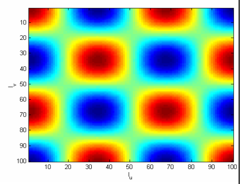	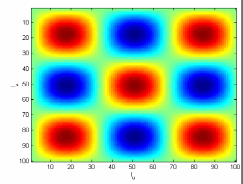
H_1=4 H_2=4	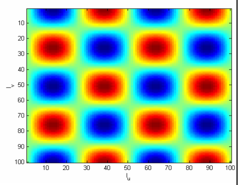	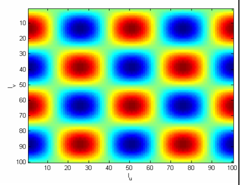	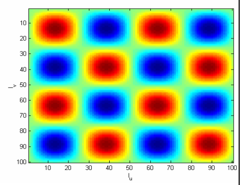	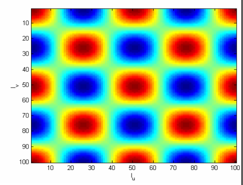

Current density vectors can be expressed in terms of the basis functions defined in 3.26 for all planar geometries. The vectors $\vec{u}$ and $\vec{v}$ are used to define perpendicular directions corresponding to different directions in cartesian coordinates for each geometry definition, which are expressed in Table 3.7.

Table 3.7: Mapping for u and v parameters onto Cartesian coordinates

Direction	Planar	Tri-Planar	Ortho. 3 Planes
u	y	x; y; x	y; x; z
v	z	z; z; z	z; y; x
$\vec{a}_u$	$\vec{a}_y$	$-\vec{a}_x$; $\vec{a}_y$; $\vec{a}_x$	$\vec{a}_y$; $\vec{a}_x$; $\vec{a}_z$
$\vec{a}_v$	$\vec{a}_z$	$\vec{a}_z$; $\vec{a}_z$; $\vec{a}_z$	$\vec{a}_z$; $\vec{a}_y$; $\vec{a}_x$
l_u	l_y	$2l_x + l_y$	l_y; l_x; l_z
l_v	l_z	l_z	l_z; l_y; l_x

3.3.2.1 Stream Functions

The $\vec{a}_u$ and $\vec{a}_v$ sinusoidal terms spatially differ by 90^0. This form gives a convenient description of the scalar functions that fully describe the current density such that

$$\vec{J} = \vec{a}_w \times \nabla\chi + \nabla\Psi \tag{3.27}$$

where $\nabla = \frac{\partial}{\partial u}\vec{a}_u + \frac{\partial}{\partial v}\vec{a}_v$ and $\vec{a}_w$ denotes the normal to the directions $\vec{a}_u$ and $\vec{a}_v$; that is

$$\vec{a}_w \times \nabla\chi = -\vec{a}_u \frac{\partial\chi}{\partial v} + \vec{a}_v \frac{\partial\chi}{\partial u} \tag{3.28}$$

Hence, the scalar function χ is conveniently expressed as

$$\chi = \sum_{q=0}^{1}\sum_{p=0}^{1}\sum_{h_1=1}^{H_1}\sum_{h_2=1}^{H_2} \kappa_{h_1h_2pq} \cos\left(k_{h_1}u + \frac{q\pi}{2}\right)\sin\left(k_{h_2}v + \frac{p\pi}{2}\right) \tag{3.29}$$

The coefficients $\kappa_{h_1h_2pq}$ can be expressed in terms of current coefficients $\alpha_{h_1h_2pq}$ and $\gamma_{h_1h_2pq}$

$$\kappa_{h_1h_2pq} = -\frac{\beta_{h_1h_2pq}k_{h_1} + \alpha_{h_1h_2pq}k_{h_1}}{k_{h_1}^2 + k_{h_2}^2} \tag{3.30}$$

Similarly:

$$\psi = \sum_{q=0}^{1}\sum_{p=0}^{1}\sum_{h_1=1}^{H_1}\sum_{h_2=1}^{H_2} \gamma_{h_1 h_2 pq} \sin\left(k_{h_1} u + \frac{q\pi}{2}\right) \cos\left(k_{h_2} v + \frac{p\pi}{2}\right) \tag{3.31}$$

where $\gamma_{h_1 h_2 pq} = \frac{\beta_{h_1 h_2 pq} k_{h_2} - \alpha_{h_1 h_2 pq} k_{h_1}}{k_{h_1}^2 + k_{h_2}^2}$

When, the current density is approximated without divergence

$$\gamma_{h_1 h_2 pq} = 0 \tag{3.32}$$

$$\beta_{h_1 h_2 pq} = \frac{k_{h_1} \alpha_{h_1 h_2 pq}}{k_{h_2}} \tag{3.33}$$

and the basis functions and the stream function are simplified to:

$$\begin{aligned}
\vec{J}_u &= \sum_{q=0}^{1}\sum_{p=0}^{1}\sum_{h_1=1}^{H_1}\sum_{h_2=1}^{H_2} \alpha_{h_1 h_2 pq} \cos\left(k_{h_1} u + \frac{q\pi}{2}\right) \cos\left(k_{h_2} v + \frac{p\pi}{2}\right) \vec{a}_u \\
\vec{J}_z &= \sum_{q=0}^{1}\sum_{p=0}^{1}\sum_{h_1=1}^{H_1}\sum_{h_2=1}^{H_2} \frac{k_{h_1} \alpha_{h_1 h_2 pq}}{k_{h_2}} \sin\left(k_{h_1} u + \frac{q\pi}{2}\right) \sin\left(k_{h_2} v + \frac{p\pi}{2}\right) \vec{a}_v \\
\chi &= \sum_{q=0}^{1}\sum_{p=0}^{1}\sum_{h_1=1}^{H_1}\sum_{h_2=1}^{H_2} -\frac{\alpha_{h_1 h_2 pq}}{k_{h_2}} \cos\left(k_{h_1} u + \frac{q\pi}{2}\right) \sin\left(k_{h_2} v + \frac{p\pi}{2}\right)
\end{aligned} \tag{3.34}$$

Therefore, only the coefficients $\alpha_{h_1 h_2 pq}$ are to be calculated using the matrix equations.

3.4 Forming the Matrix Equation

3.4.1 Magnetic Field Expressions

When cylindrical coordinates are considered, the components of the vector potential

$$\vec{A}(r) = \int_V \vec{J}_s(r') \frac{e^{-jk|r-r'|}}{4\pi\mu\,|r-r'|} dr' \tag{3.35}$$

can be expressed as:

$$\begin{aligned}
\vec{A}_\rho(r) &= \frac{1}{4\pi\mu} \int_{S_0} \vec{J}_\phi(r') \frac{e^{-jk|r-r'|}}{|r-r'|} \sin(\phi - \phi_0)\, dS \\
\vec{A}_\phi(r) &= \frac{1}{4\pi\mu} \int_{S_0} \vec{J}_\phi(r') \frac{e^{-jk|r-r'|}}{|r-r'|} \cos(\phi - \phi_0)\, dS \\
\vec{A}_z(r) &= \frac{1}{4\pi\mu} \int_{S_0} \vec{J}_z(r') \frac{e^{-jk|r-r'|}}{|r-r'|} dS
\end{aligned} \tag{3.36}$$

for uniform medium where $r \to (x, y, z)$ and $r' \to (x_0, y_0, z_0)$ represent field and source point vectors; and ϕ and ϕ_0 represent angle values for field and source points respectively. The equations do not include the radial current density $\vec{J}_\rho$ as the current density is only defined on the cylinder surface where there exists no current in radial direction. S_0 represents the cylinder surface where every subdomain area is equal to dS .

Magnetic field expression in cylindrical coordinates can be obtained using

$$\vec{B} = \nabla \times \vec{A} \tag{3.37}$$

as follows:

$$\begin{aligned}
B_x &= \int_{S_0} \frac{e^{-jkR}}{4\pi\mu R^2} \left(jk + \frac{1}{R}\right) \begin{bmatrix} -J_z(\phi_0, z_0)(\rho \sin\phi - \rho_0 \sin\phi_0) \\ +J_\phi(\phi_0, z_0)(z - z_0)\cos\phi_0 \end{bmatrix} dS \\
B_y &= \int_{S_0} \frac{e^{-jkR}}{4\pi\mu R^2} \left(jk + \frac{1}{R}\right) \begin{bmatrix} J_z(\phi_0, z_0)(\rho \cos\phi - \rho_0 \cos\phi_0) \\ +J_\phi(\phi_0, z_0)(z - z_0)\sin\phi_0 \end{bmatrix} dS \\
B_z &= \int_{S_0} \frac{e^{-jkR}}{4\pi\mu R^2} \left(jk + \frac{1}{R}\right) J_\phi(\phi_0, z_0)\, dS
\end{aligned} \tag{3.38}$$

where

$$
\begin{aligned}
R &= \sqrt{(x-x_0)^2+(y-y_0)^2+(z-z_0)^2} \\
&= \sqrt{\rho^2+\rho_0^2+2\rho\rho_0\cos(\phi-\phi_0)+(z-z_0)^2}
\end{aligned}
$$

are the radial lengths of the field and source points with reference to the origin respectively.

When Cartesian coordinates are considered, the magnetic field components can be expressed as:

$$
\begin{aligned}
B_x &= \int_{S_0} \frac{e^{-jkR}}{4\pi\mu R^2}\left(jk+\frac{1}{R}\right)\begin{bmatrix} -J_z(y_0,z_0)(y-y_0) \\ +J_y(y_0,z_0)(z-z_0) \end{bmatrix} dS \\
B_y &= \int_{S_0} \frac{e^{-jkR}}{4\pi\mu R^2}\left(jk+\frac{1}{R}\right)\left[J_z(y_0,z_0)(x-x_0)+J_x(y_0,z_0)(z-z_0)\right] dS \\
B_z &= \int_{S_0} \frac{e^{-jkR}}{4\pi\mu R^2}\left(jk+\frac{1}{R}\right)\left[J_x(y_0,z_0)(y-y_0)-J_y(y_0,z_0)(x-x_0)\right] dS
\end{aligned} \tag{3.39}
$$

where $R=\sqrt{(x-x_0)^2+(y-y_0)^2+(z-z_0)^2}$.

3.4.2 Method

1. Source field is subdivided into N subdomains.
2. Target field is subdivided into M subdomains.
3. Centers of the subdomains are used as source and target coordinates.
4. Basis function expressions are substituted into magnetic field expressions in order to obtain a relation between the magnetic field and surface

current density for i_{th} target field and j_{th} source field in the following form:

$$\begin{aligned}
B_{x,i} &= \sum_{j=1}^{N}\sum_{h_1=1}^{H_1}\sum_{h_2=1}^{H_2}\alpha_{h_1h_2,j}K_{xh_1h_2,ij} \\
B_{y,i} &= \sum_{j=1}^{N}\sum_{h_1=1}^{H_1}\sum_{h_2=1}^{H_2}\alpha_{h_1h_2,j}K_{yh_1h_2,ij} \\
B_{z,i} &= \sum_{j=1}^{N}\sum_{h_1=1}^{H_1}\sum_{h_2=1}^{H_2}\alpha_{h_1h_2,j}K_{zh_1h_2,ij}
\end{aligned} \tag{3.40}$$

where $i = 1, 2, \ldots M$ and $j = 1, 2, \ldots N$ and for cylindrical source field and for

$$G(R) = \frac{e^{-jkR}}{4\pi\mu R^2}\left(jk + \frac{1}{R}\right) \tag{3.41}$$

$$\begin{aligned}
K_{xh_1h_2,ij} &= G(R)\begin{bmatrix} -\frac{k_n}{k_m}\cos(k_n y_{0,j})\cos(k_m z_{0,j})(y_i - y_{0,j}) \\ +\sin(k_n y_{0,j})\sin(k_m z_{0,j})(z_i - z_{0,j}) \end{bmatrix}\Delta S \\
K_{yh_1h_2,ij} &= G(R)\begin{bmatrix} \frac{h_1}{\rho_0 k_h}\sin(h_1\phi_{0,j})\sin(k_h z_{0,j} - \frac{h_2\pi}{2})(\rho\cos\phi_i - \rho_0\cos\phi_{0,j}) \\ +\cos(h_1\phi_{0,j})\cos(k_h z_{0,j} - \frac{h_2\pi}{2})(z_i - z_{0,j})\sin\phi_{0,j} \end{bmatrix}\Delta S \\
K_{zh_1h_2,ij} &= G(R)\cos(h_1\phi_{0,j})\cos(k_h z_{0,j} - \frac{h_2\pi}{2})\,\Delta S
\end{aligned} \tag{3.42}$$

while for planar source field on yz-plane:

$$\begin{aligned}
K_{xh_1h_2,ij} &= G(R)\begin{bmatrix} -\frac{k_n}{k_m}\cos(k_n y_{0,j})\cos(k_m z_{0,j})(y_i - y_{0,j}) \\ +\sin(k_n y_{0,j})\sin(k_m z_{0,j})(z_i - z_{0,j}) \end{bmatrix}\Delta S \\
K_{yh_1h_2,ij} &= G(R)\left[\cos(k_n y_0)\cos(k_m z_0)(x_i - x_{0,j})\right]\ \Delta S \\
K_{zh_1h_2,ij} &= G(R)\ \left[-\sin(k_n y_{0,j})\sin(k_m z_{0,j})(x_i - x_{0,j})\right]\ \Delta S
\end{aligned} \tag{3.43}$$

5. In order to describe the relation for all target and source fields a matrix equation is formed in the form $Ax = b$ such that:

$$
\begin{aligned}
A &= \begin{bmatrix}
K_{x11,11} & K_{x12,11} & . & K_{x1H_2,11} & . & K_{xH_1H_2,11} & K_{x11,12} & . & K_{xH_1H_2,1N} \\
K_{x11,21} & K_{x12,21} & . & K_{x1H_2,21} & . & K_{xH_1H_2,21} & K_{x11,22} & . & K_{xH_1H_2,2N} \\
\vdots & \vdots & \vdots & & & & \vdots & & \\
K_{x11,M1} & K_{x12,M1} & . & K_{x1H_2,M1} & . & K_{xH_1H_2,M1} & K_{x11,M2} & . & K_{xH_1H_2,MN} \\
K_{y11,11} & K_{y12,11} & . & K_{y1H_2,11} & . & K_{yH_1H_2,11} & K_{y11,12} & . & K_{yH_1H_2,1N} \\
K_{y11,21} & K_{y12,21} & . & K_{y1H_2,21} & . & K_{yH_1H_2,21} & K_{y11,22} & . & K_{yH_1H_2,2N} \\
\vdots & \vdots & \vdots & & & & \vdots & & \\
K_{y11,M1} & K_{y12,M1} & . & K_{y1H_2,M1} & . & K_{yH_1H_2,M1} & K_{y11,M2} & . & K_{yH_1H_2,MN} \\
K_{z11,11} & K_{z12,11} & . & K_{z1H_2,11} & . & K_{zH_1H_2,11} & K_{z11,12} & . & K_{zH_1H_2,1N} \\
K_{z11,21} & K_{z12,21} & . & K_{z1H_2,21} & . & K_{zH_1H_2,21} & K_{z11,22} & . & K_{zH_1H_2,2N} \\
\vdots & \vdots & \vdots & & & & \vdots & & \\
K_{z11,M1} & K_{z12,M1} & \dots & K_{z1H_2,M1} & . & K_{zH_1H_2,M1} & K_{z11,M2} & . & K_{zH_1H_2,MN}
\end{bmatrix} \\
x &= \begin{bmatrix}
\alpha_{11,1} \\ \alpha_{12,1} \\ \vdots \\ \alpha_{1H_2,1} \\ \vdots \\ \alpha_{H_1H_2,1} \\ \alpha_{11,2} \\ \vdots \\ \alpha_{H_1H_2,N}
\end{bmatrix}_{NH_1H_2\ x\ 1} \\
b &= \begin{bmatrix}
B_{x,1} \\ B_{x,2} \\ \vdots \\ B_{x,M} \\ B_{y,1} \\ \vdots \\ B_{y,M} \\ B_{z,1} \\ \vdots \\ B_{z,M}
\end{bmatrix}_{3M\ x\ 1}
\end{aligned}
\tag{3.44}
$$

where A is a $3M \times H_1H_2N$ matrix. This matrix equation is obtained for each required RF Field definition and for each source geometry using MATLAB.

Implementations for the remaining three geometries are carried out in a similar manner to planar surface modifying the target and source coordinates and assigning the basis function parameters taking the boundary conditions into consideration. However, matrix A is usually an ill-condition matrix and therefore, the matrix solution has to be obtained using regularization methods.

3.5 Obtaining the Solution by Regularization

In order to obtain the solution matrix x, TSVD, Tikhonov, CGLS, TTLS, Rutisbauer methods are implemented, the details of which are explained in Appendix A.

In order to obtain minimum error and optimum solutions for each regularization, the regularization parameters are swept,

1. For CGLS method, iteration number k is incremented from 1 to 3000 in steps of one.

2. For Tikhonov Method, three different L matrices are evaluated (identity, first derivative and second derivative) and regularization parameter λ is evaluated as 10^i and i is swept from 2 to -8 in decremented steps of 0,5.

3. For Rutisbauer Method, regularization parameter λ is evaluated as 10^i and i is swept from 2 to -8 in decremented steps of 0,5.

4. For TSVD Method, regularization parameter k is swept from 1 to 1800 in incremented steps of 30.

$\|Ax\|$ and $\|x\|$ norms are evaluated for each value of the swept regularization parameter for each

1. matrix A obtained for the geometry selection,

2. matrix b required field selection,

3. regularization method.

Using the L-Curve Method [46], optimum solution for the current density and stream function coefficients are recorded and the average error percentages between the required and generated magnetic field are calculated for each regularization method, source geometry and RF field case.

In order to decrease the complexity of the comparison process, the RF field options, which turned out to yield high error percentages are eliminated and the comparison process is carried out with RF field case 4.

Each solution is evaluated taking the error percentage and the realizability of the coil into consideration. The stream function contours form the patterns for the coil conductor, so it is the major measure of how realizable the coil is.

3.6 Approximating the Stream Function by a Conductor

After the solution is obtained using one of the regularization parameters, the coefficients can be substituted back into the basis functions in order to obtain the current density distribution and stream functions for every subdomain.

The contours of the stream functions are used to determine the conductor shape for the RF coil.

3.6.1 A simple Procedure

1. Choose the number of contour lines, $N_s \in \aleph$ to describe the two dimensional stream function on a surface S on xz plane.

2. Define the difference of current between two adjacent streamlines as:

$$\Delta I = \frac{max_{x \in S} \psi(x) - min_{x \in S} \psi(x)}{N_s} \tag{3.45}$$

3. The centerlines of the unconnected conductors are the isolines of $\psi(x)$ with step ΔI,

$$\{x \in S \mid \psi(x)\} = min_{x \in S}\psi(x) + (n - \frac{1}{2})\Delta I, \quad n = 1, ..., N_s \tag{3.46}$$

4. Form unconnected conductors from the centerlines by applying a width. The width can be constrained by physical considerations or optimization parameters.

5. Convert the unconnected conductors into one conductor by opening ends of close loops and adding one end to another changing the streamline shape as slightly as possible.

CHAPTER 4

Results and Conclusion

Using the methods explained in Chapter 3, the matrix equation is obtained for the four geometries of source fields. RF field case 4 is defined as the desired magnetic field to be produced by the RF coil on these geometries. The target field is defined as a cube placed at the center of the the source fields.

The regularization techniques stated in Chapter 3 are used in the solution of the matrix equation. The parameters of each regularization method are adjusted in order to find the minimum and optimum error percentage for each source geometry. The solutions obtained by these regularization provide the current density distributions and stream functions on the corresponding source fields. The stream function contours are investigated and a comparison between error percentages and realizibility of the coil pattern is made.

The stream function contours obtained for the planar source field is formed into a conductor pattern by the procedure explained in Chapter 3 and the magnetic field produced by the coil is calculated theoretically. This coil is also realized and a circuit is designed to provide the coil with the calculated current values. The magnetic field produced using DC current is measured using 3-Channel Gauss meter.

A circuit is designed in order to tune and match the coil to operate in 0.15 Tesla METU MRI System, which is explained in 4.2.2.3.

4.1 Theoretical Results

4.1.1 Desired and Generated Magnetic Fields

The minimum and optimum error percentages are calculated for each solution obtained by the corresponding regularization method using the formula:

$$error\ \% = \frac{\left[\sum_{i=1}^{M} \frac{\left(B_{desired,i} - B_{calculated,i}\right)^2}{B_{desired,i}^2}\right]}{3M} \times 100 \qquad (4.1)$$

where M is the number of field points.

The error percentages for minimum error solution are illustrated in Table 4.1 while error percentages for optimum error solution are illustrated in Table 4.2.

Table 4.1: Error percentages for solutions with minimum error. Minimum error percentages between the desired and generated magnetic field are illustrated for the current density solutions obtained by applying the regularization methods listed as columns to source surfaces listed as rows for the corresponding target fields.

	CGLS	Rutisbauer	TSVD	Tikhonov		
				L= Identity	L=$1^{st}der.$	L=$2^{nd}der.$
Planar	25,7	26,0	25,2	25,1	25,2	24,8
Tri-Planar	3,8	4,1	3,8	3,8	3,7	3,8
3 Orth. Planes	11,2	12,0	2,5	2,5	2,4	2,2
Cylindrical	3,8	3,9	3,9	3,9	3,9	3,8

Table 4.2: Error percentages for solutions with optimum error. Error percentages between the desired and generated magnetic field are illustrated for the optimum current density solutions obtained by applying the regularization methods listed as columns to source surfaces listed as rows for the corresponding target fields.

	CGLS	Rutisbauer	TSVD	Tikhonov		
				L= Identity	L=$1^{st}der.$	L=$2^{nd}der.$
Planar	26,0	35,0	29,0	30,6	30,7	26,6
Tri-Planar	4,3	9,5	5,0	6,6	8,4	4,2
3 Orth. Planes	12,1	29,9	3,2	3,7	4,6	6,1
Cylindrical	4,7	7,5	5,3	4,6	9,2	9,3

The regularization parameter values used in order to obtain the minimum and optimum error solutions are stated in Table 4.3, Table 4.4, Table 4.5 and Table 4.6.

Table 4.3: Regularization parameter values for planar surface

PLANAR			
		Minimum Error Solution	Optimum Error Solution
CGLS		iteration number = 2305	iteration number = 273
Rutisbauer		$\lambda = 3.162 \times 10^{-7}$	$\lambda = 3.162 \times 10^{-3}$
TSVD		truncation level = 691	truncation level = 181
Tikhonov	L= identity	$\lambda = 10^{-6}$	$\lambda = 3.162 \times 10^{-2}$
	L= 1^{st} der.	$\lambda = 10^{-6}$	$\lambda = 0.1$
	L= 2^{nd} der.	$\lambda = 10^{-3}$	$\lambda = 0.01$

Table 4.4: Regularization parameter values for tri-planar surface

TRI-PLANAR			
		Minimum Error Solution	Optimum Error Solution
CGLS		iteration number = 1294	iteration number = 165
Rutisbauer		$\lambda = 10^{-8}$	$\lambda = 3.162x10^{-4}$
TSVD		truncation level = 661	truncation level = 61
Tikhonov	L= identity	$\lambda = 3.162 \times 10^{-7}$	$\lambda = 0.01$
	L= 1^{st} der.	$\lambda = 3.162 \times 10^{-7}$	$\lambda = 0.1$
	L= 2^{nd} der.	$\lambda = 10^{-7}$	$\lambda = 10^{-4}$

Table 4.5: Regularization parameter values for three orthogonal planes

THREE ORTHOGONAL PLANES			
		Minimum Error Solution	Optimum Error Solution
CGLS		iteration number = 198; 2789; 3000	iteration number = 162; 331; 395
Rutisbauer		$\lambda = 10^{-8}$; 10^{-8}; 10^{-8}	$\lambda = 10^{-4}$; 3.162×10^{-4}; 3.162×10^{-4}
TSVD		truncation level = 301; 451; 541	truncation level = 61; 61; 91
Tikhonov	L= identity	$\lambda = 10^{-7}; 10^{-7}; 10^{-7}$	$\lambda = 10^{-4}; 3.162 \times 10^{-7}; 10^{-3}$
	L= 1^{st} der.	$\lambda = 3.162 \times 10^{-7}; 10^{-7}; 3.162 \times 10^{-7}$	$\lambda = 10^{-3}; 3.162 \times 10^{-6}; 0.01$
	L= 2^{nd} der.	$\lambda = 3.162 \times 10^{-8}; 3.162 \times 10^{-8}; 3.162 \times 10^{-8}$	$\lambda = 3.162 \times 10^{-4}; 10^{-4}; 10^{-4}$

Table 4.6: Regularization parameter values for cylindrical surface

CYLINDRICAL			
		Minimum Error Solution	Optimum Error Solution
CGLS		iteration number = 2984	iteration number = 52
Rutisbauer		$\lambda = 10^{-8}$	$\lambda = 0.3162$
TSVD		truncation level = 661	truncation level = 61
Tikhonov	L= identity	$\lambda = 3.162 \times 10^{-6}$	$\lambda = 3.162 \times 10^{-3}$
	L= 1^{st} der.	$\lambda = 10^{-5}$	$\lambda = 10^{-2}$
	L= 2^{nd} der.	$\lambda = 3.162 \times 10^{-7}$	$\lambda = 10^{-4}$

4.1.2 Stream Function Contours

The stream function contours resulting from the minimum and optimum error solutions for each regularization method are illustrated in tables from Table 4.7 to Table 4.14.

Table 4.7: Stream function contours for planar surface - 1

PLANAR		
	Minimum Error Solution	Optimum Error Solution
CGLS	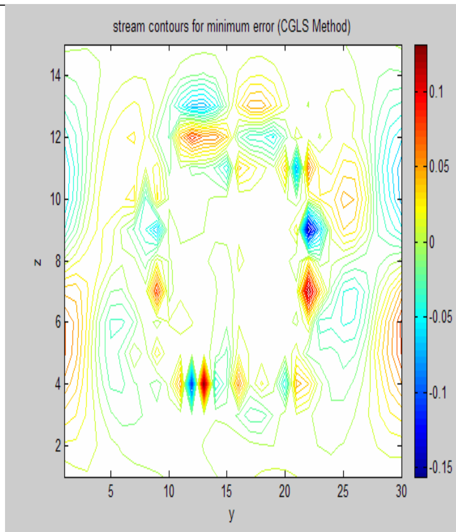	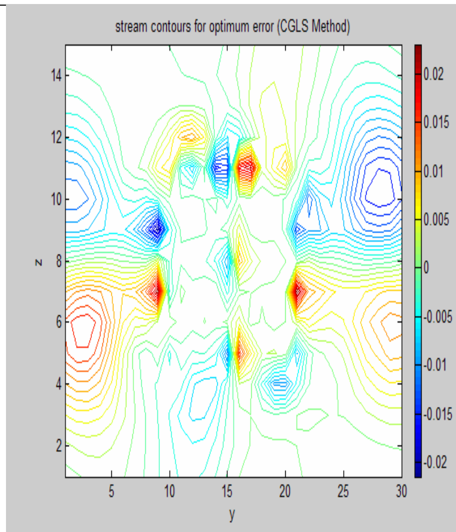
Rutis.	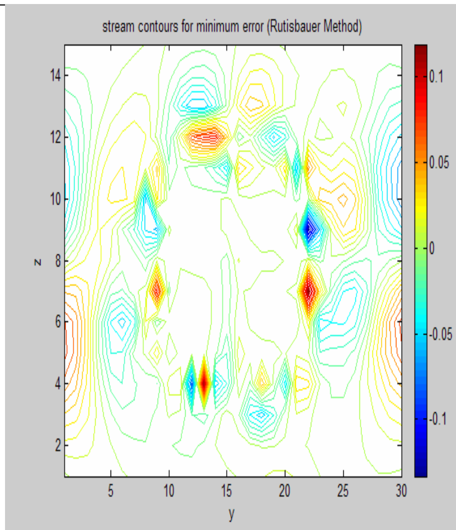	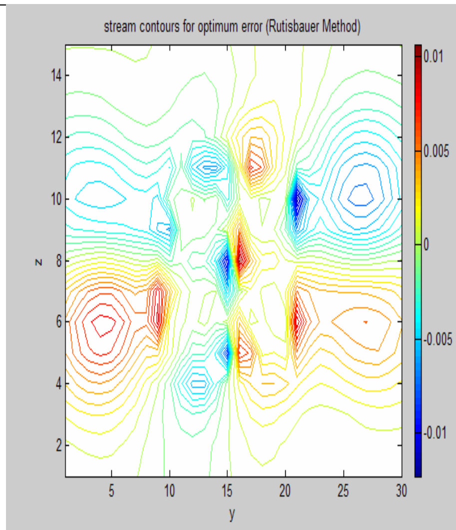
TSVD	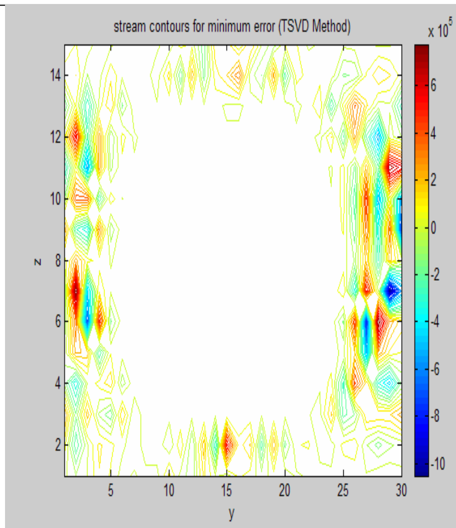	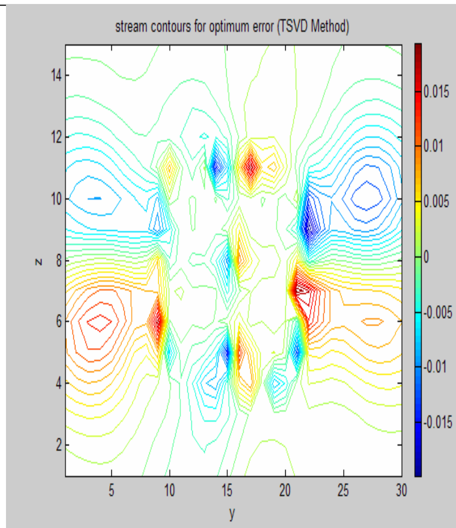

Table 4.8: Stream function contours for planar surface - 2

PLANAR		
Tikh.	Minimum Error Solution	Optimum Error Solution
$L = I$	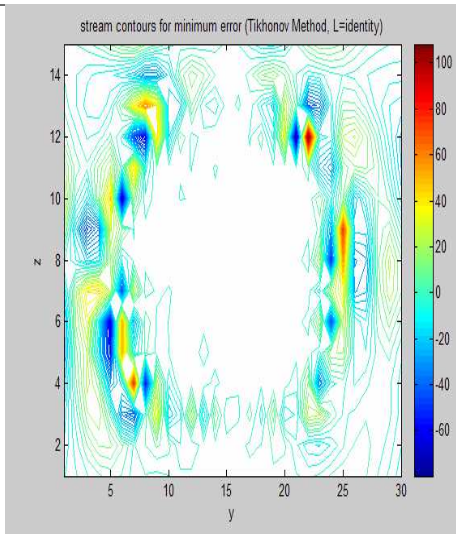	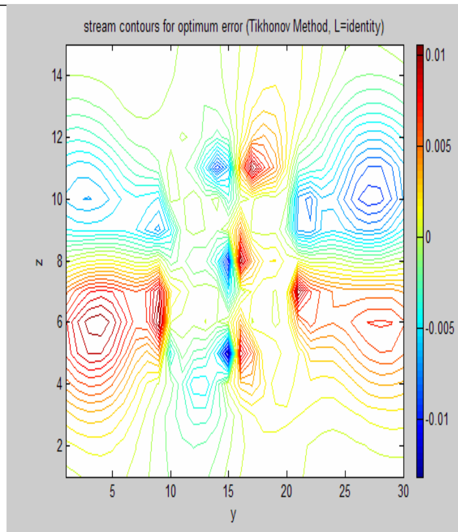
$L = 1^{st} der.$	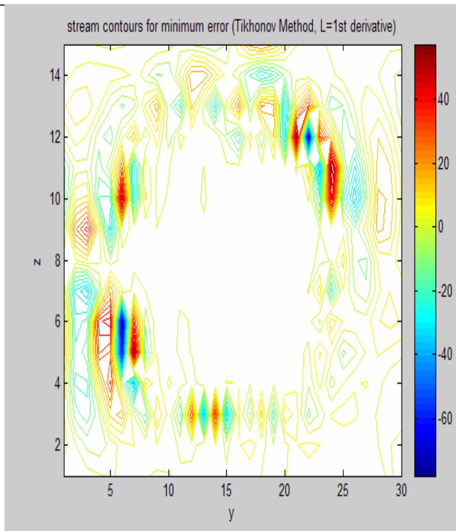	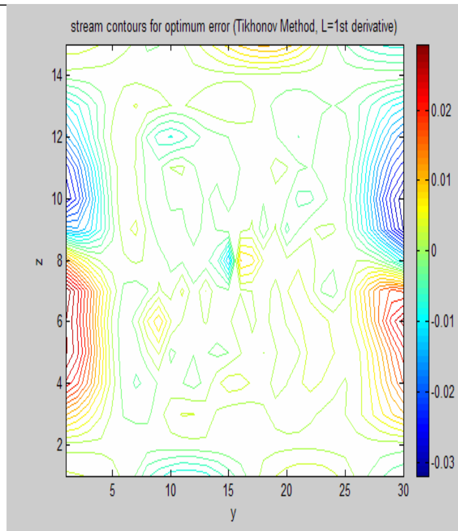
$L = 2^{nd} der.$	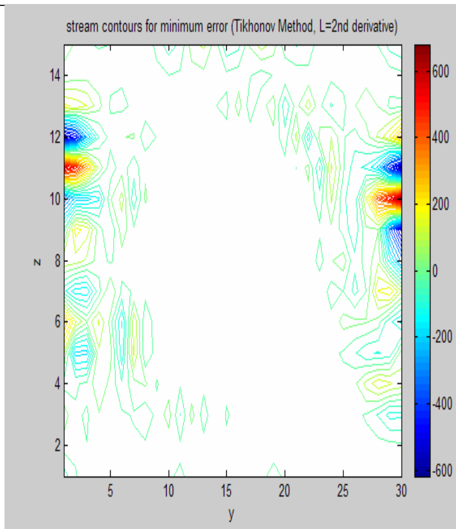	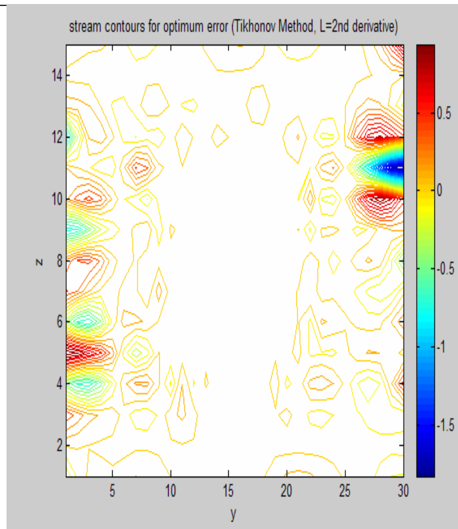

Table 4.9: Stream function contours for tri-planar surface - 1

TRI-PLANAR		
	Minimum Error Solution	Optimum Error Solution
CGLS	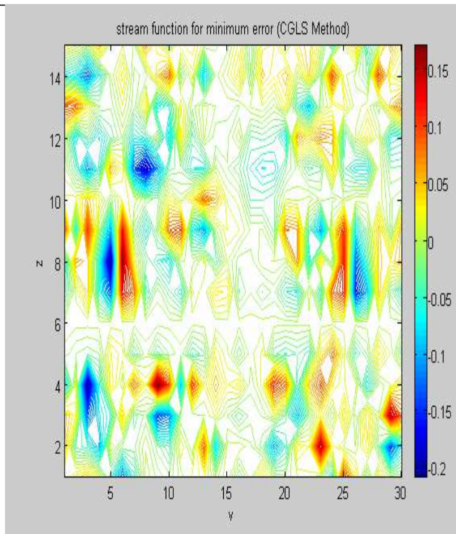	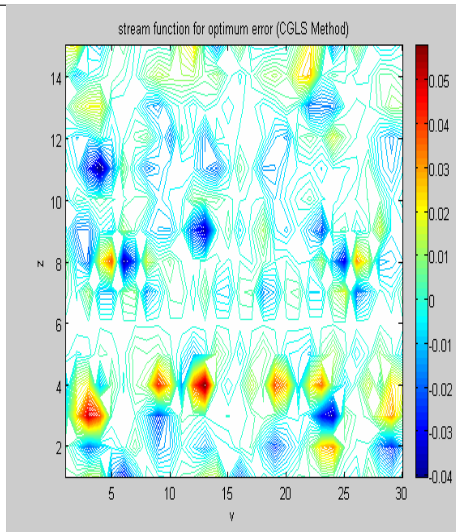
Rutis.	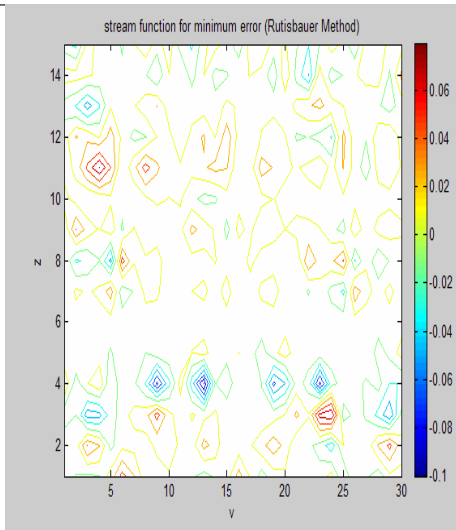	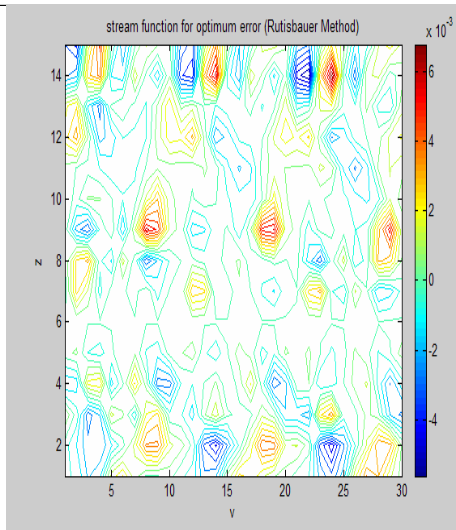
TSVD	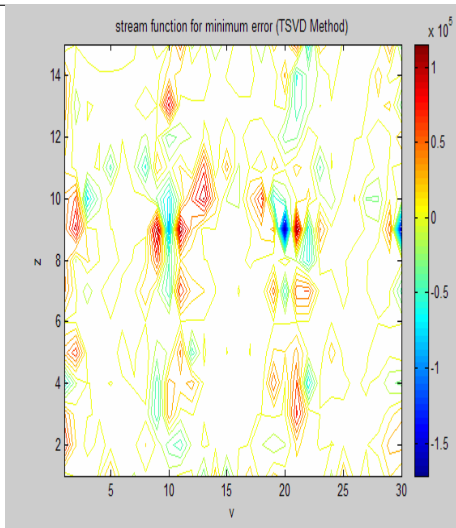	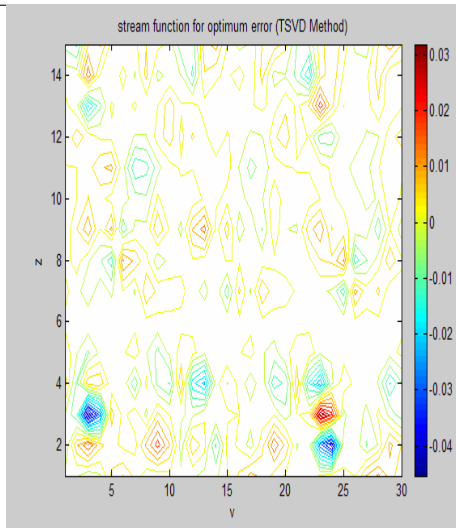

Table 4.10: Stream function contours for tri-planar surface - 2

TRI-PLANAR		
Tikh.	Minimum Error Solution	Optimum Error Solution
$L = I$	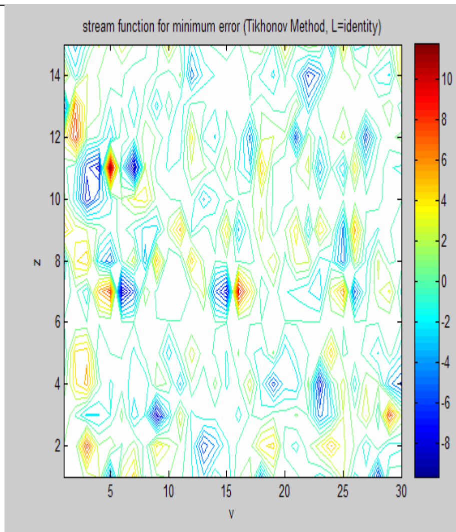	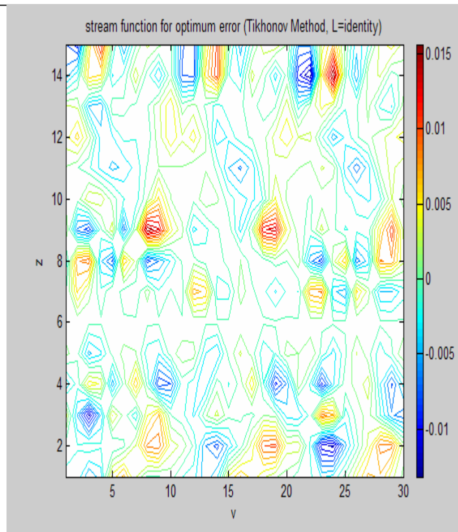
$L = 1^{st} der.$	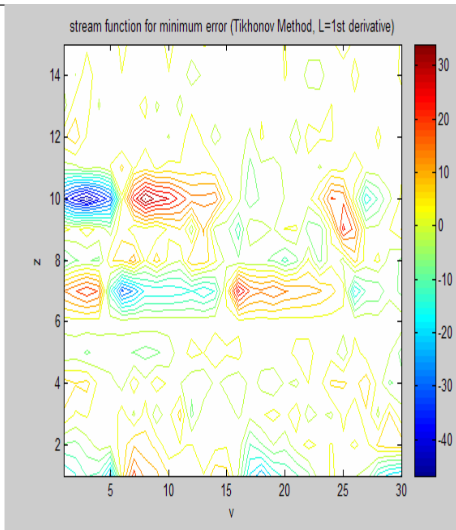	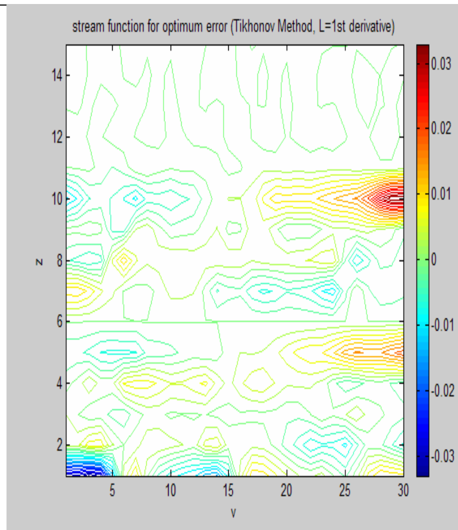
$L = 2^{nd} der.$	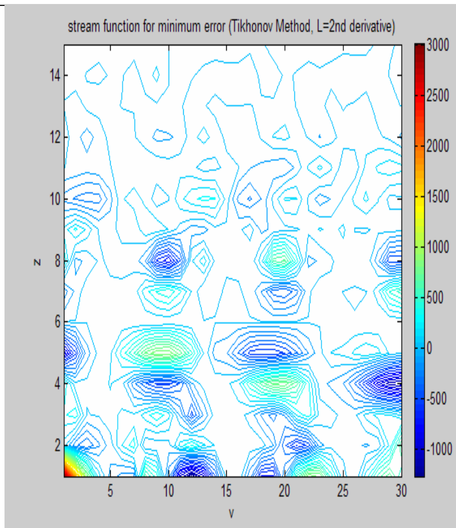	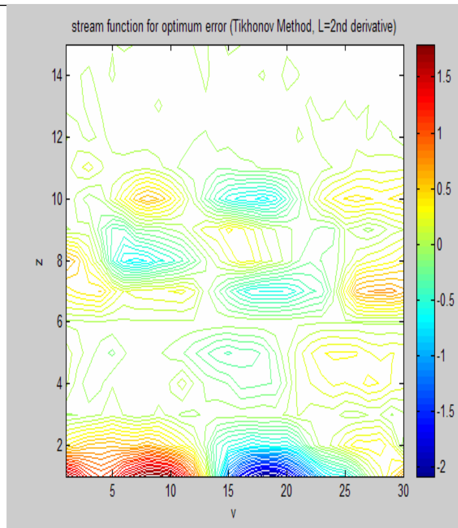

Table 4.11: Stream function contours for three orthogonal planes - 1

THREE ORTHOGONAL PLANES		
	Minimum Error Solution	Optimum Error Solution
CGLS	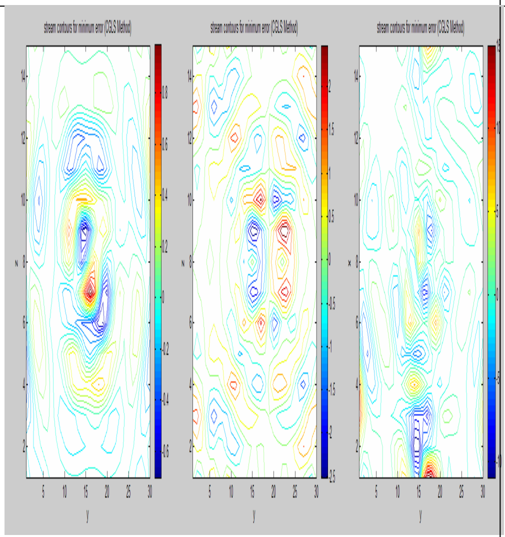	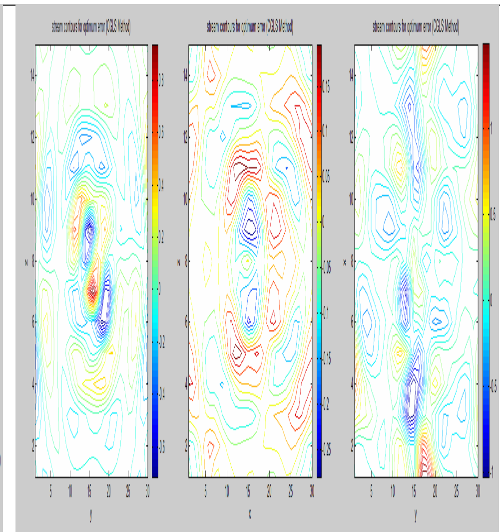
Rutis.	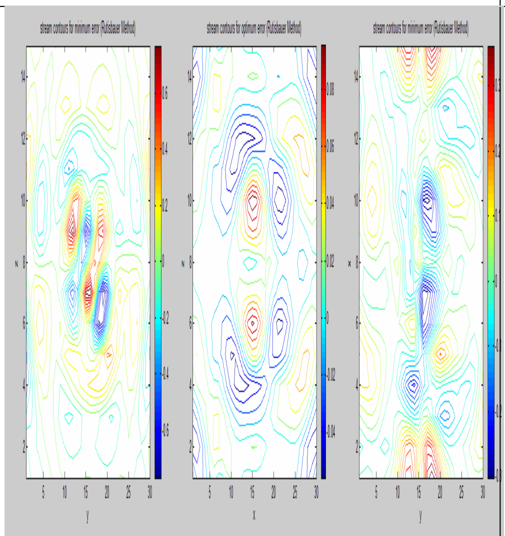	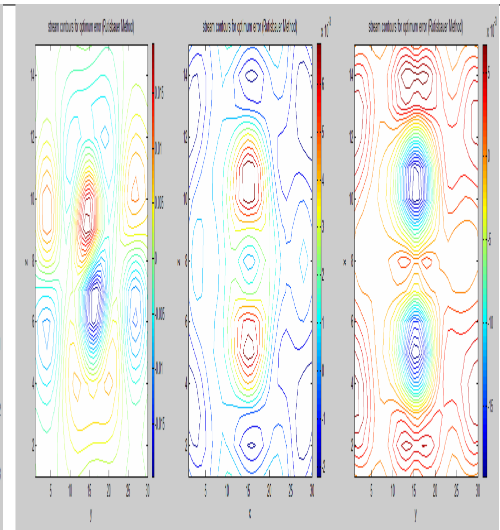
TSVD	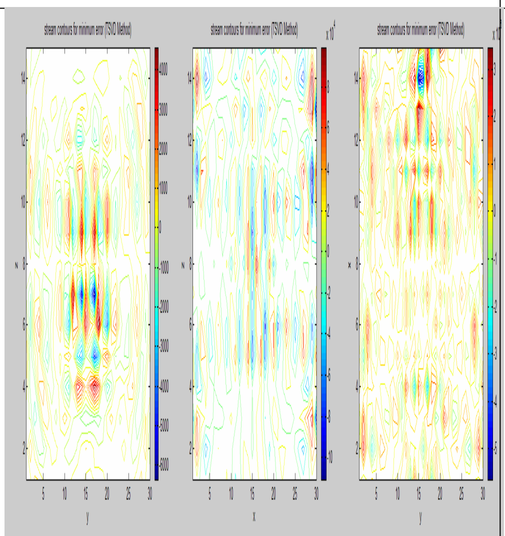	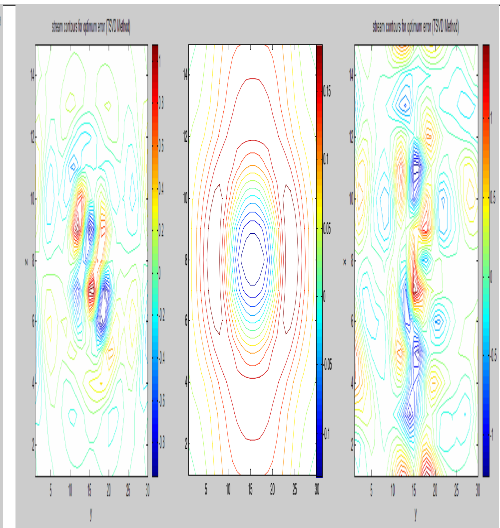

Table 4.12: Stream function contours for three orthogonal planes - 2

THREE ORTHOGONAL PLANES		
Tikh.	Minimum Error Solution	Optimum Error Solution
$L = I$	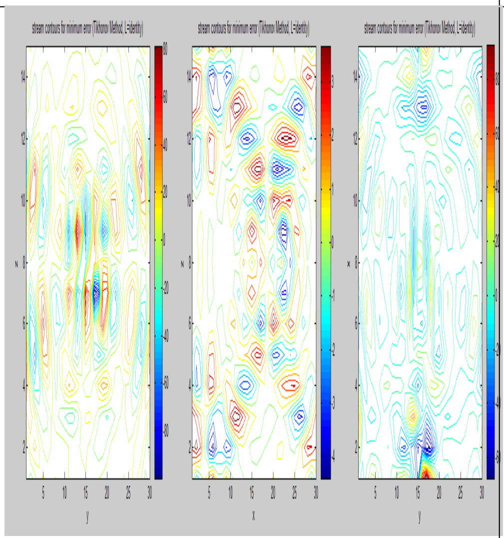	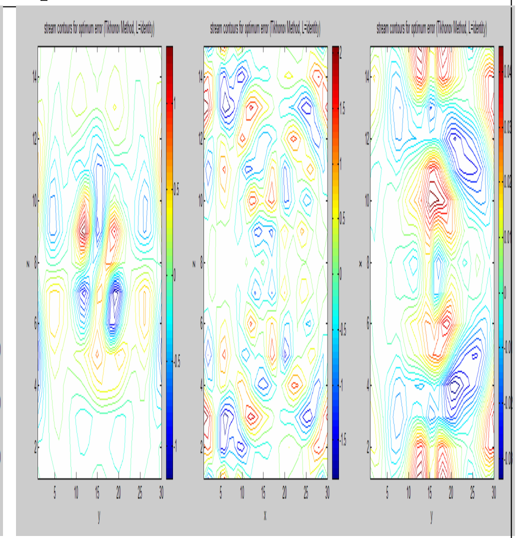
$L = 1^{st} der.$	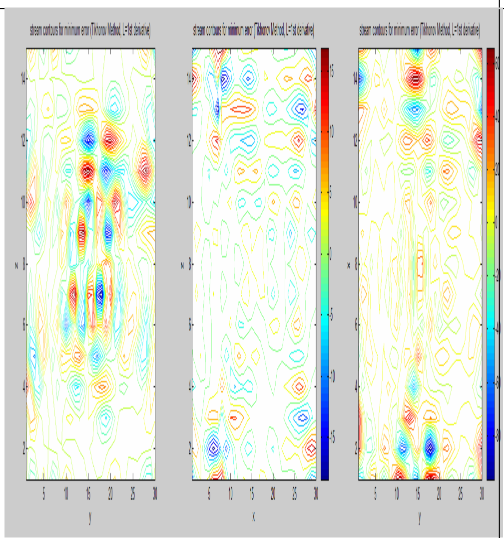	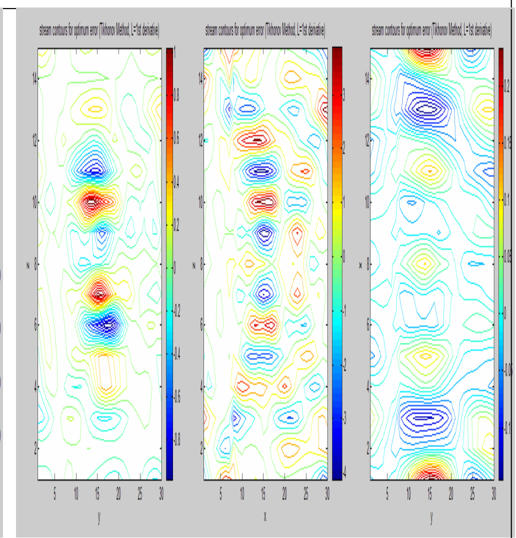
$L = 2^{nd} der.$	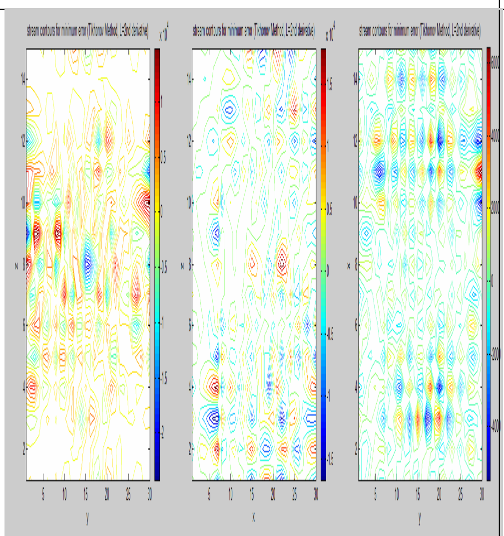	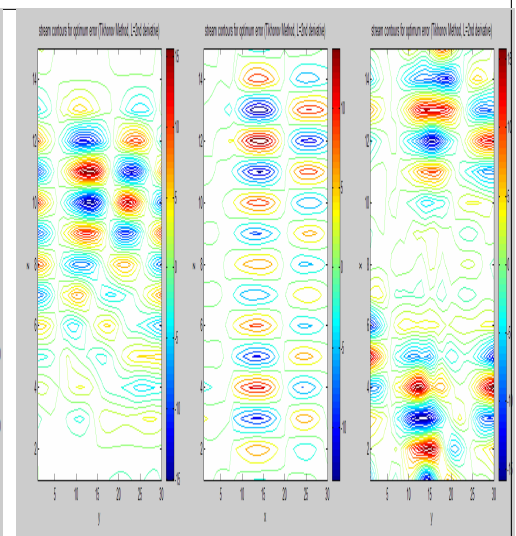

Table 4.13: Stream function contours for cylindrical surface - 1

CYLINDRICAL		
	Minimum Error Solution	Optimum Error Solution
CGLS	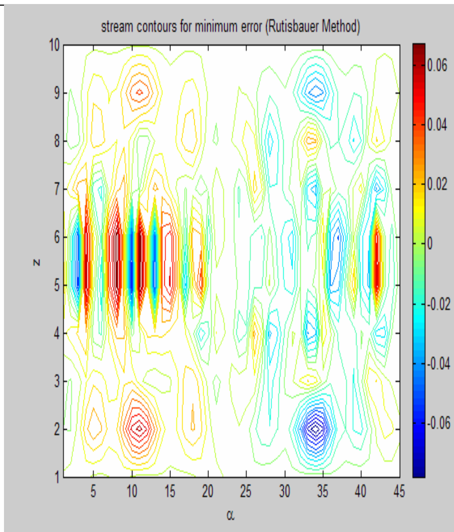	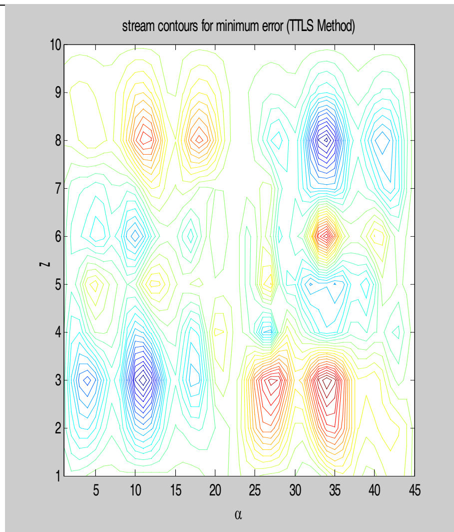
Rutis.	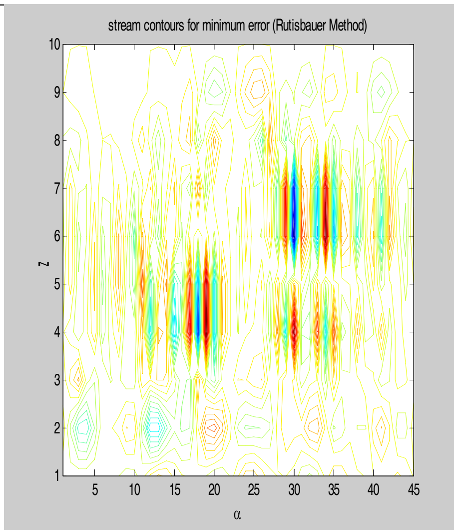	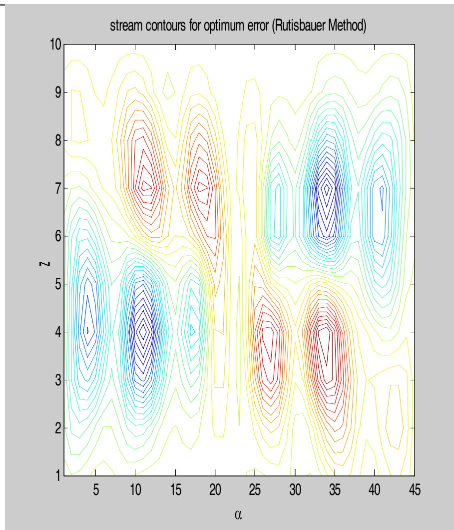
TSVD	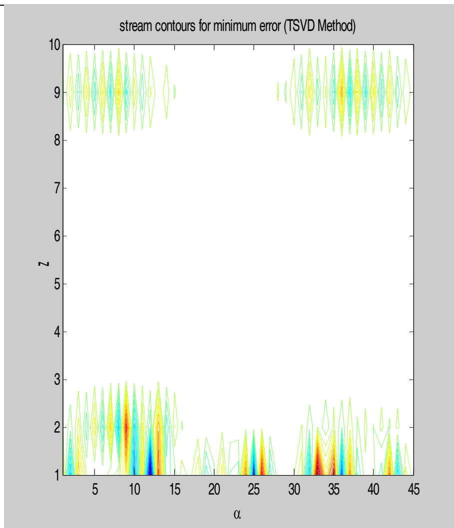	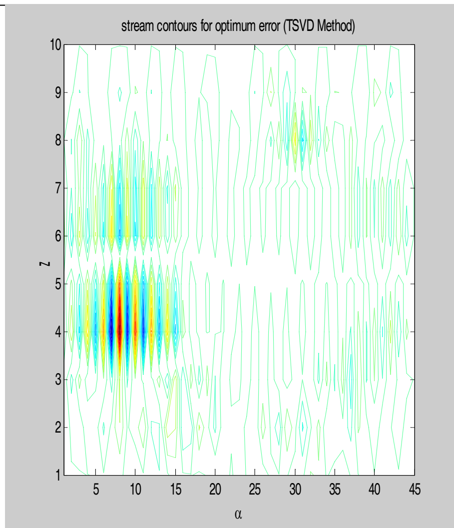

Table 4.14: Stream function contours for cylindrical surface - 2

CYLINDRICAL		
Tikh.	Minimum Error Solution	Optimum Error Solution
$L = I$	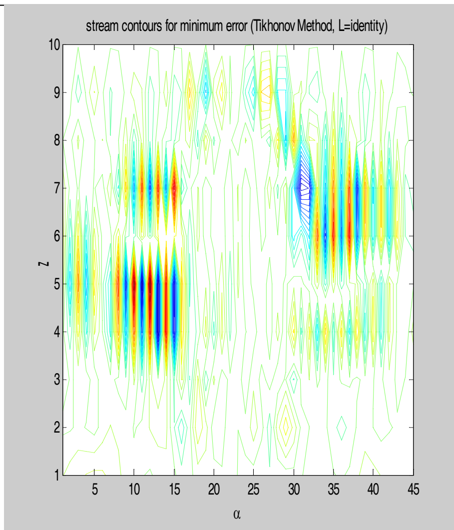	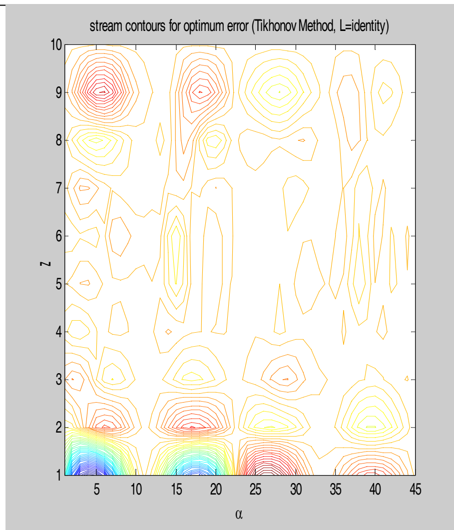
$L = 1^{st} der.$	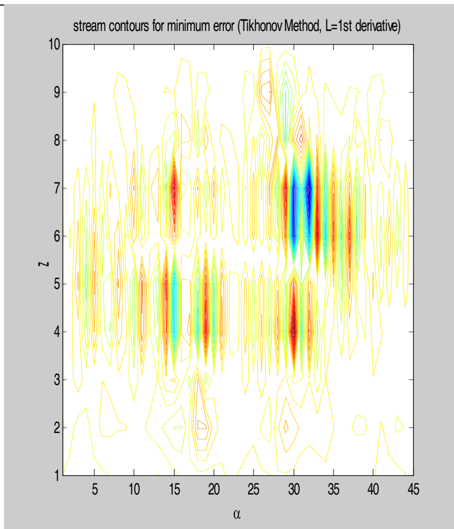	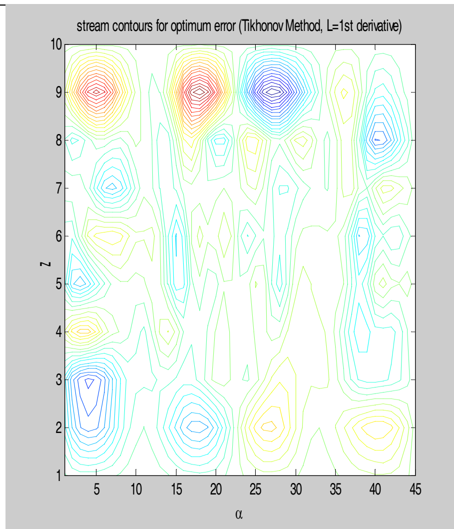
$L = 2^{nd} der.$	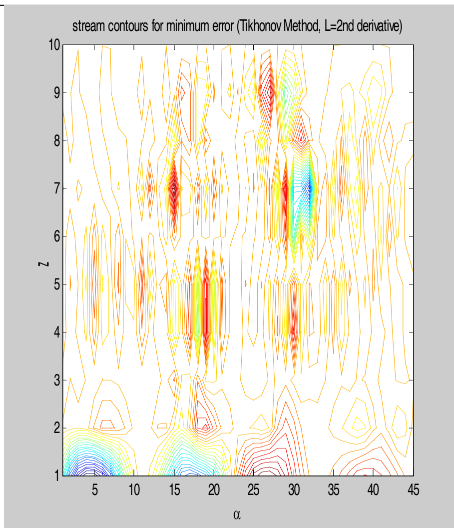	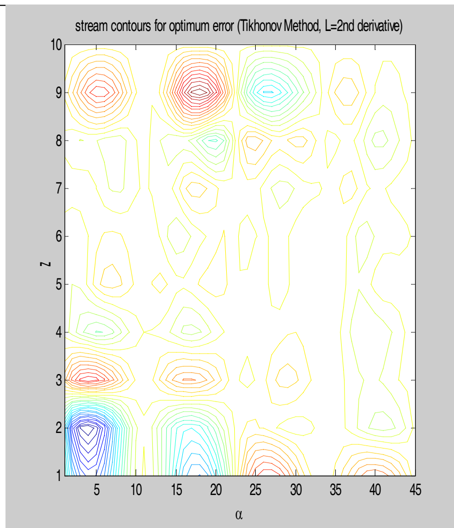

When the conductor patterns obtained using each regularization method for each geometry are compared with reference to the complexity of patterns, the optimum surface geometry is determined to be the cylindrical coil and the optimum regularization method is chosen to be Rutisbauer, which produces the conductor pattern illustrated in Figure 4.1.

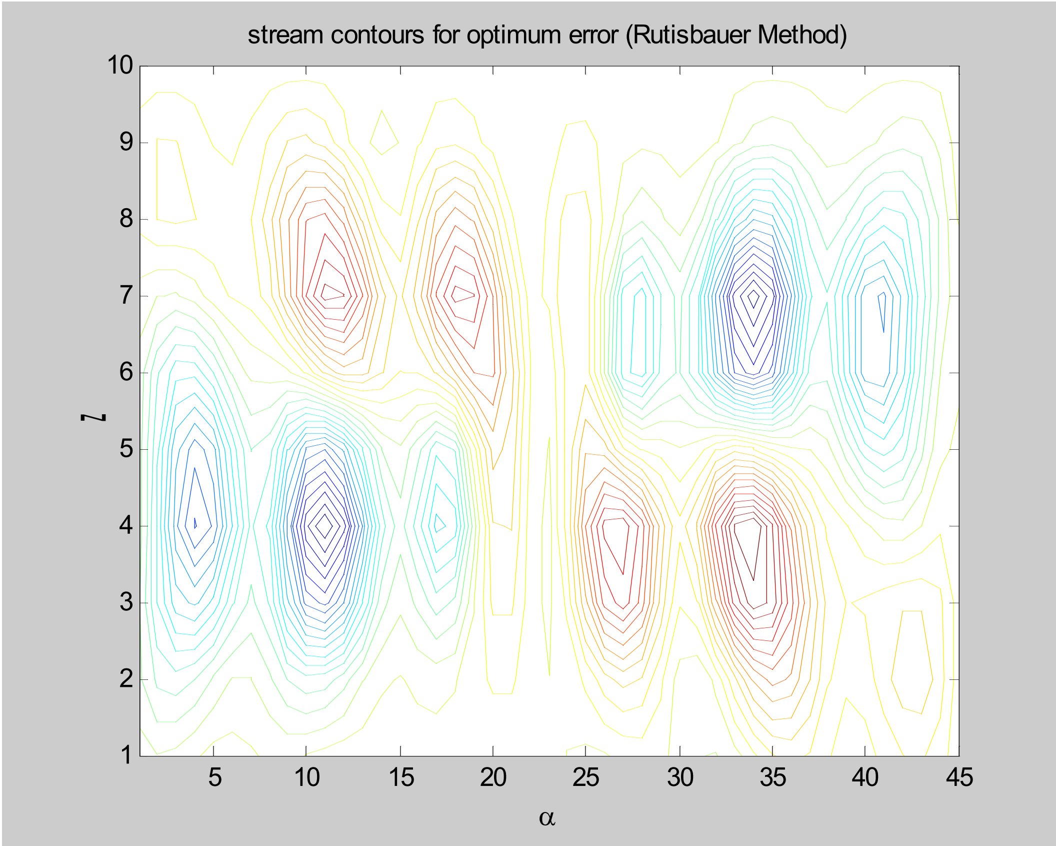

Figure 4.1: Stream function contours on the cylindrical surface for the solution with optimum error

4.2 Realizing the Coil

4.2.1 Orientation of Field Points

In order to illustrate the desired and created magnetic field values, 2-D plots are used, which illustrate the magnetic field magnitudes at corresponding field points. Figure 4.2 illustrates the orientation of the field points and which number they symbolize on the magnetic field plot.

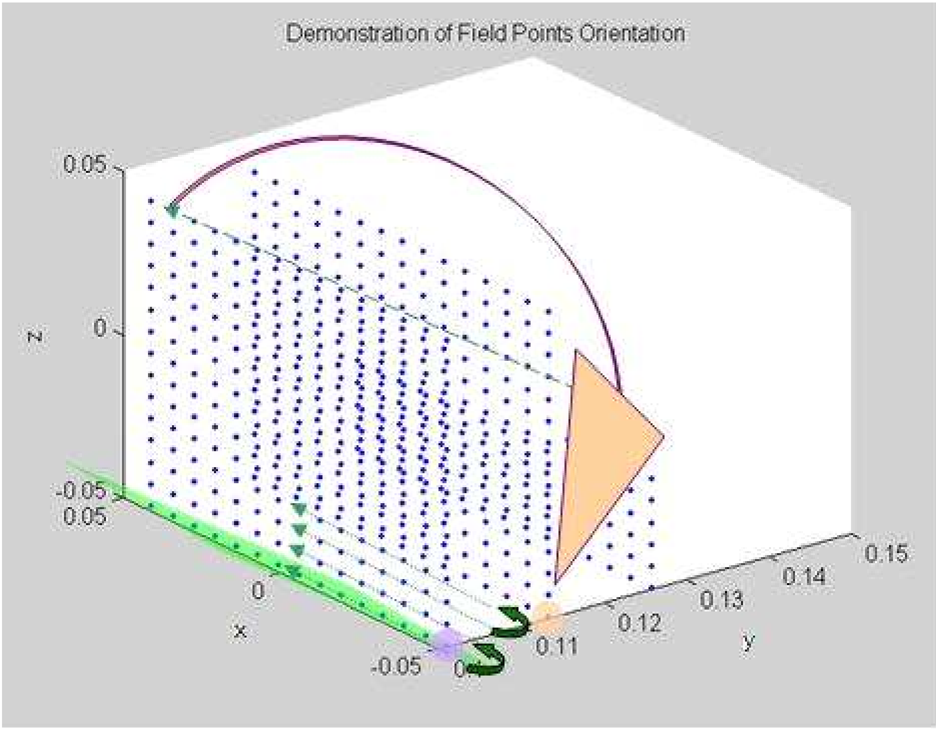

Figure 4.2: Orientation of field points in the target field. The target field is made up of 1800 field points. The target volume is a 10 cm by 10 cm by 10 cm cube the center of which is placed at point (0,12.5,0) and which is divided into 15, 8 and 15 divisions in x, y and z directions respectively.During the formation of field points, first the x- axis is filled while y and z values are kept constant. When a single x row is filled, which corresponds to 15 points, z value is incremented and another x row is filled from negative to positive direction. This means, the purple dot corresponds to "1" on the magnetic field plot and the first 15 point group on the magnetic field plot symbolize the highlighted points in Figure 4.2, increasing in value in the direction of the green arrows on Figure 4.2. When a single slice of the cube is filled, which corresponds to 225 points, y value is incremented

During the formation of field points, first the x- axis is filled while y and z values are kept constant. When a single x row is filled, which corresponds to 15 points, z value is incremented and another x row is filled from negative to positive direction. This means, the purple dot corresponds to "1" on the magnetic field plot and the first 15 point group on the magnetic field plot symbolize the highlighted points in Figure 4.2, increasing in value in the direction of the green arrows on Figure 4.2. When a single slice of the cube is filled, which corresponds to 225 points, y value is incremented. Figure 4.2 illustrates this transition with an orange arrow.

The magnetic field plots which are illustrated have a maximum index of 5400 instead of the number of field points, which is 1800. This is because all the three components are displayed on the same graph. That is, first 1800 index display B_x component, the second 1800 index display B_y component and the third 1800 index display the B_z component on the plots.

4.2.2 Implementation of the Planar Coil

In order to realize the coil pattern, the solution for xz-plane member of the three orthogonal planes using Rutisbauer method is considered. The required magnetic field for this member has a homogeneous y component and the remaining components are zero as illustrated in Figure 4.3.

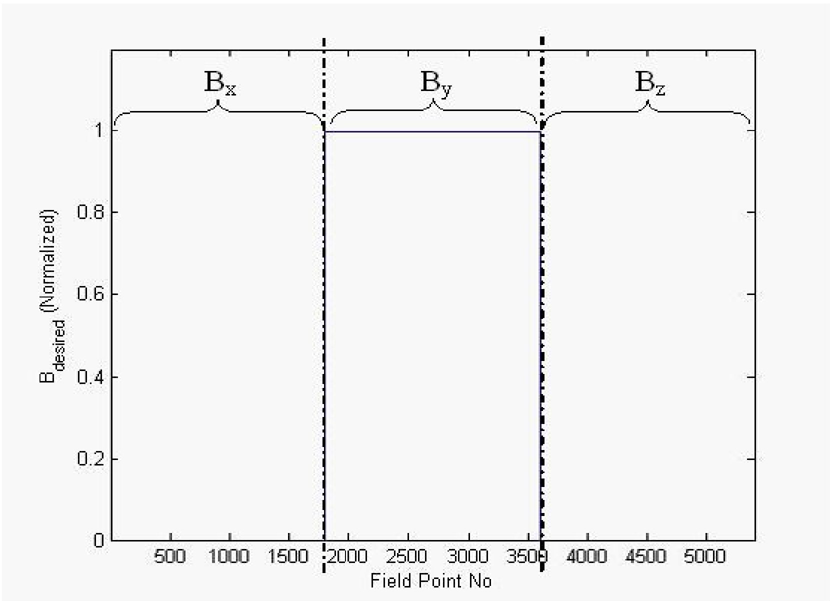

Figure 4.3: Normalized desired magnetic field Components at field points. The first 1800 field points correspond to the x-component of the magnetic field with the orientation stated above. The second and third 1800 field points correspond to the y and z components respectively.

4.2.2.1 Current Density and Stream Function Solutions

The solutions obtained for current density distribution in x and z directions on the planar surface are illustrated in Figure 4.4 and Figure 4.5.

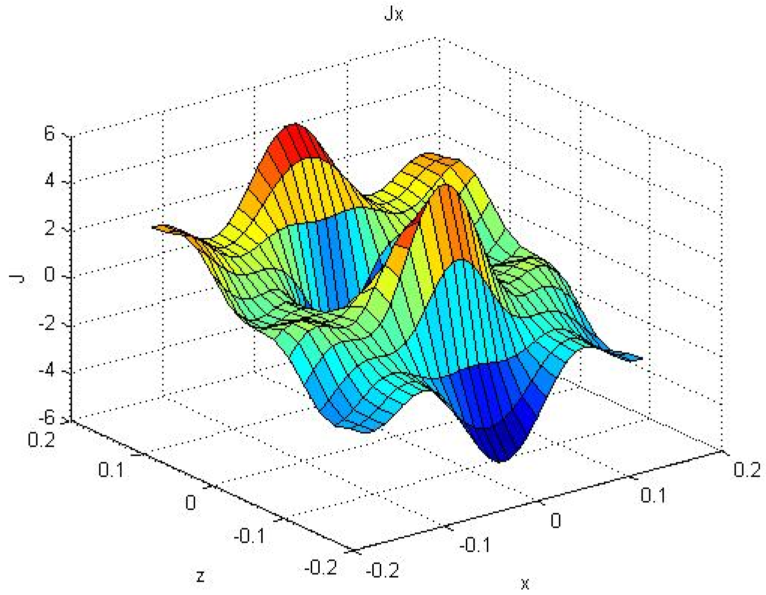

Figure 4.4: Magnitude of J_x solution for the planar surface on xz-plane. The center of the planar surface of dimensions 30 cm by 30 cm is placed at (x=0, z=0) on xz-plane. The magnitude of J is expressed in A/m.

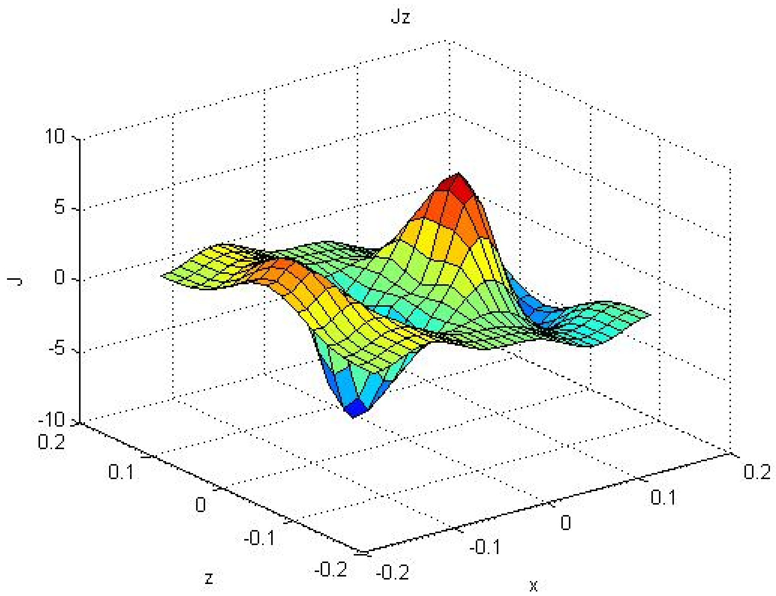

Figure 4.5: Magnitude of J_z solution for the planar surface on xz-plane. The center of the planar surface of dimensions 30 cm by 30 cm is placed at (x=0, z=0) on xz-plane. The magnitude of J is expressed in A/m.

Figure 4.6 illustrates the current density solution in vector plot.

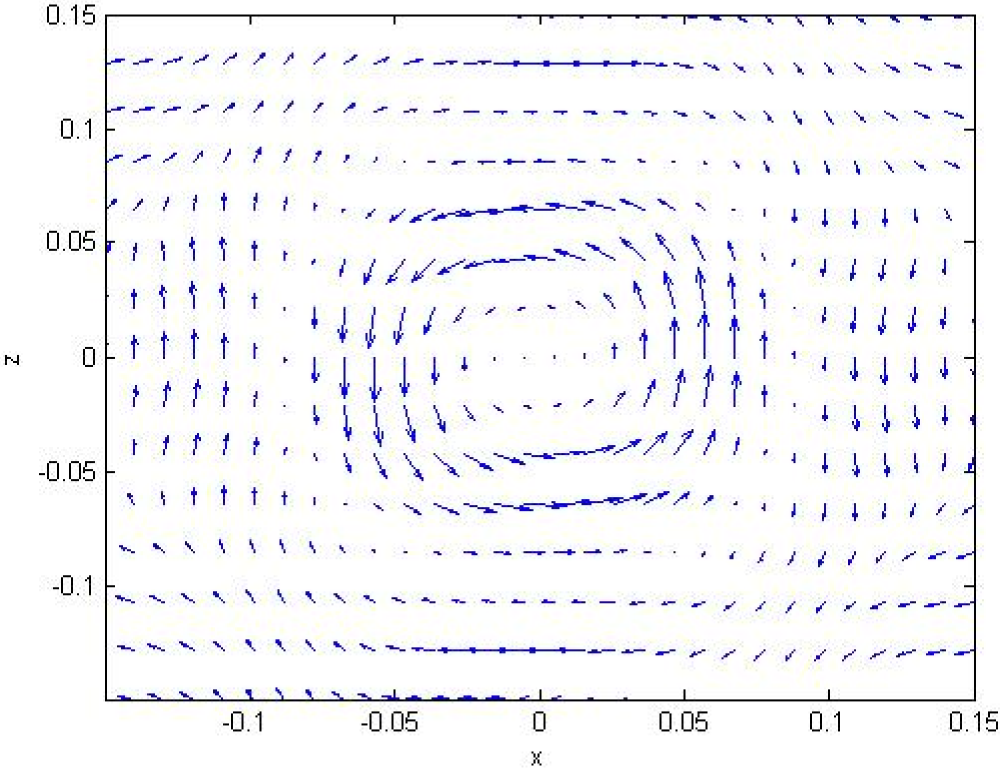

Figure 4.6: Current density distribution solution on the planar surface on xz-plane in vector form. The lengths of the arrows are proportional to the magnitude of the current density vector at the corresponding point.

The solution obtained for the problem yields a two dimensional stream function, the contour plot of which is illustrated in Figure 4.7.

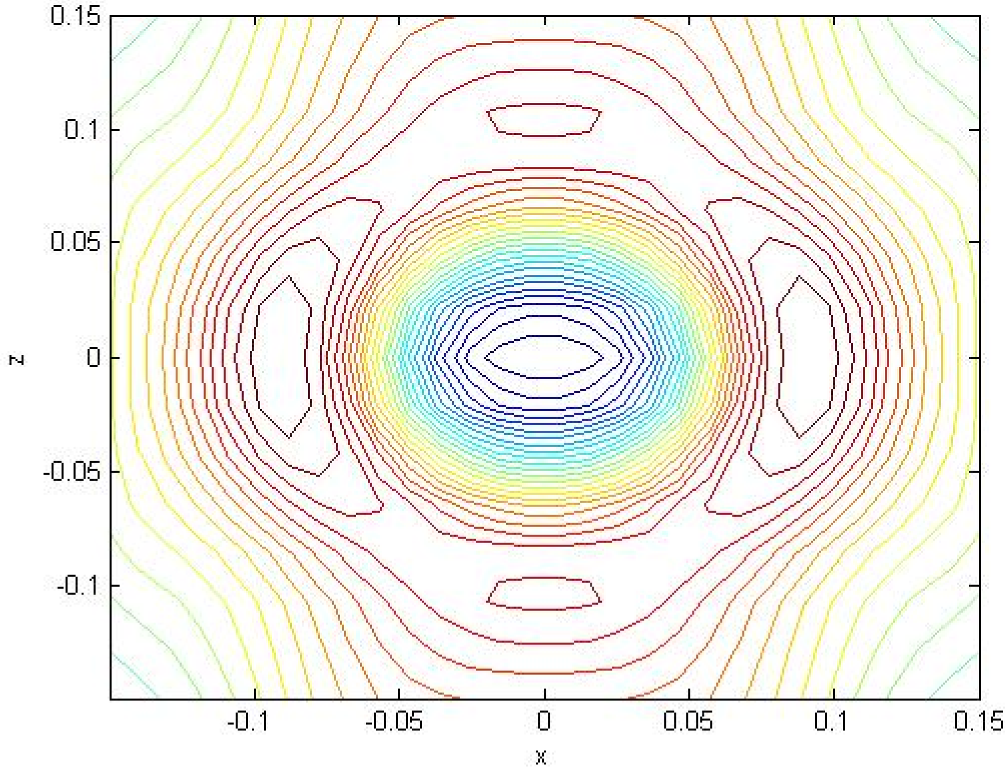

Figure 4.7: Stream function solution for the current density distribution on the xz-plane. x and z axis represent the coordinates of the points on the planar surface in meters. The stream function is represented with 25 streamlines.

The stream function solution is considered using 6 streamlines as illustrated in Figure 4.8.

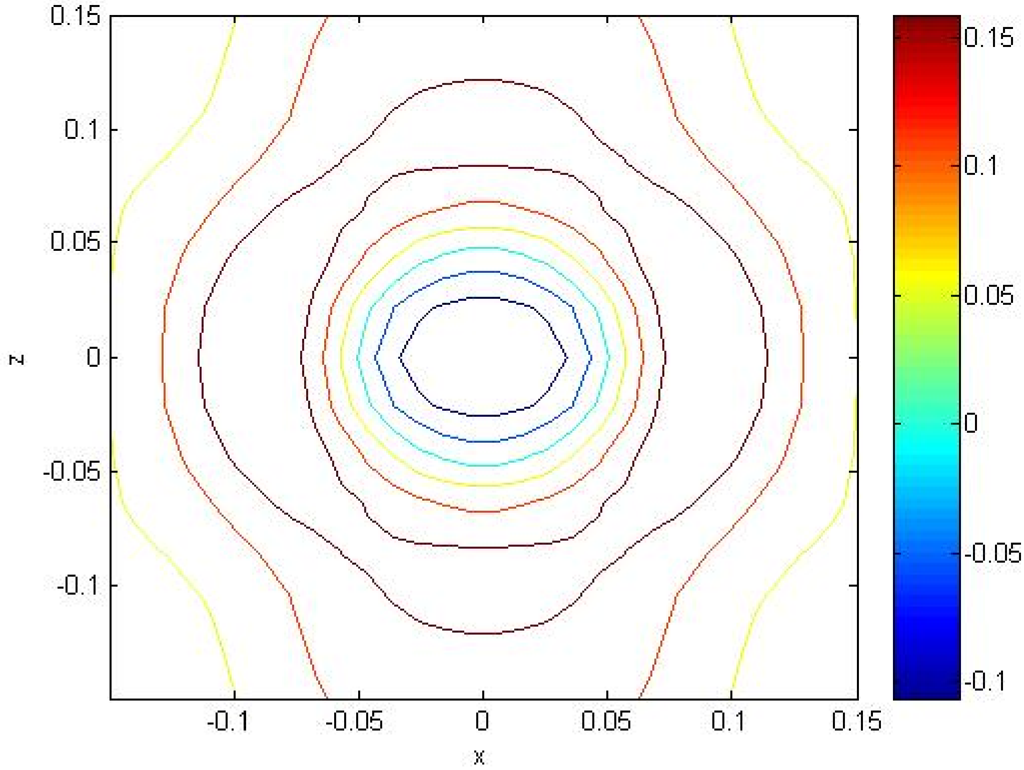

Figure 4.8: Streamlines for the stream function solution on the xz-Plane. x and z axis represent the coordinates of the points on the planar surface in meters. The stream function is represented with 6 streamlines.

4.2.2.2 Comparing the Desired, Generated and Measured Fields

The magnetic field calculated using the current density distribution solution is illustrated in Figure 4.9. The average error percentage between the y component of the desired and the generated magnetic field using current density distributions is calculated to be 4.38%.

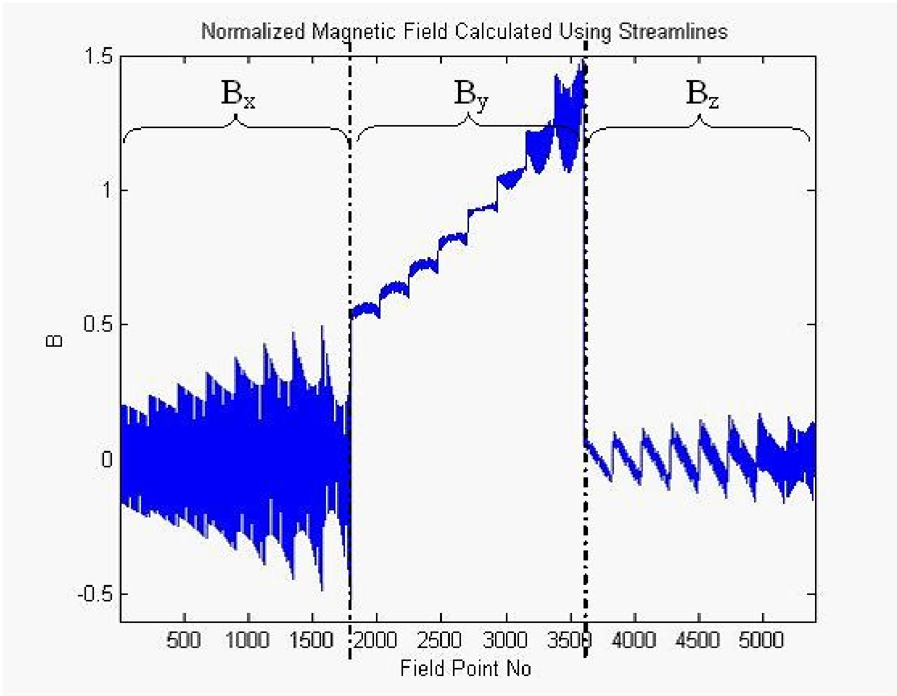

Figure 4.9: Normalized magnetic field components generated by current density solution. The first 1800 field points correspond to the x-component of the magnetic field with the orientation stated in the text. The second and third 1800 field points correspond to the y and z components respectively.

The stream function contours are used to construct the coil pattern. In order to observe the magnetic field generated by the coil pattern derived from the stream function contours, the contours are considered as conductors and generated magnetic field is calculated. The magnetic field generated by passing currents through streamlines is illustrated in Figure 4.10.

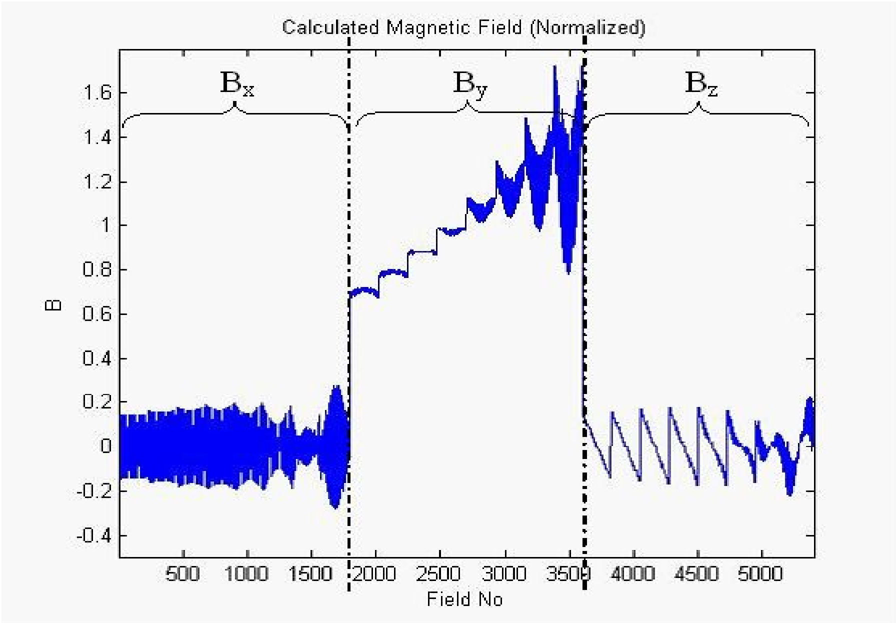

Figure 4.10: Normalized magnetic field components generated using streamlines. Streamlines are considered as conductor wires. The first 1800 field points correspond to the x-component of the magnetic field with the orientation stated above. The second and third 1800 field points correspond to the y and z components respectively.

The average error percentage between the y component of the desired and the generated magnetic field using stream lines is calculated to be 6.83%.

4.2.2.3 Constructing the Coil and the Circuitry

The streamlines illustrated in Figure 4.8 are utilized as explained in Chapter 3 to construct a conductor pattern for the RF coil. The conductor pattern is produced using AutoCAD and the design illustrated in Figure 4.11 is realized by etching of $FR4$ plates. The realized coil is illustrated in Figure 4.12

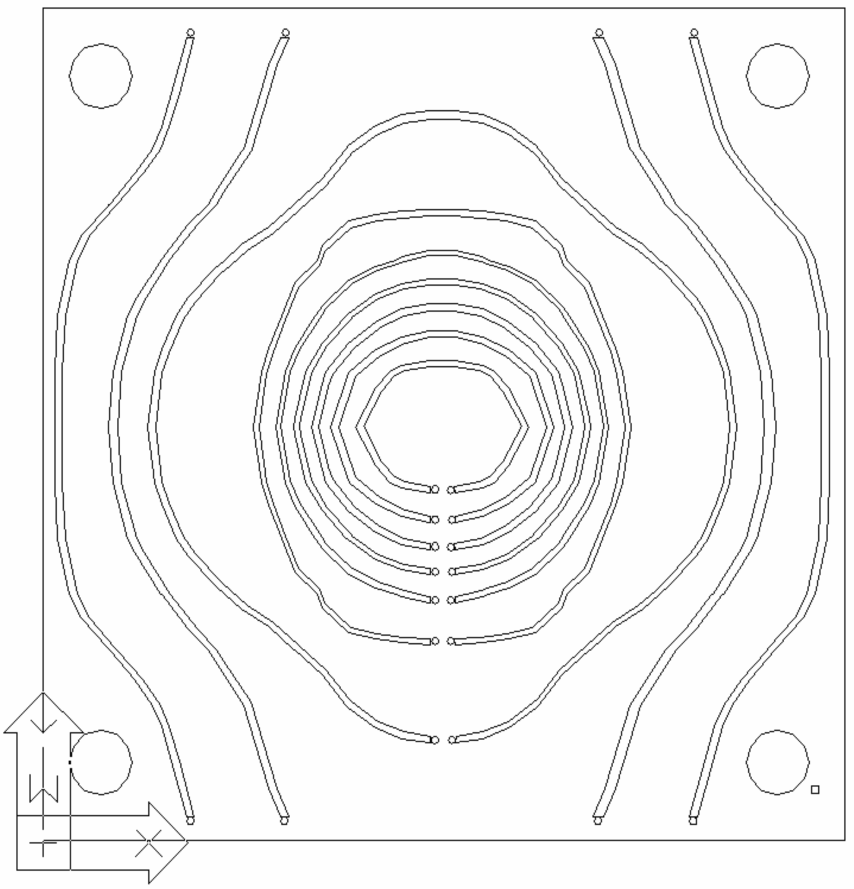

Figure 4.11: Planar RF coil design. Each conductor path is represented as an independent wire strip. The wires that carry the same current magnitudes are interconnected.

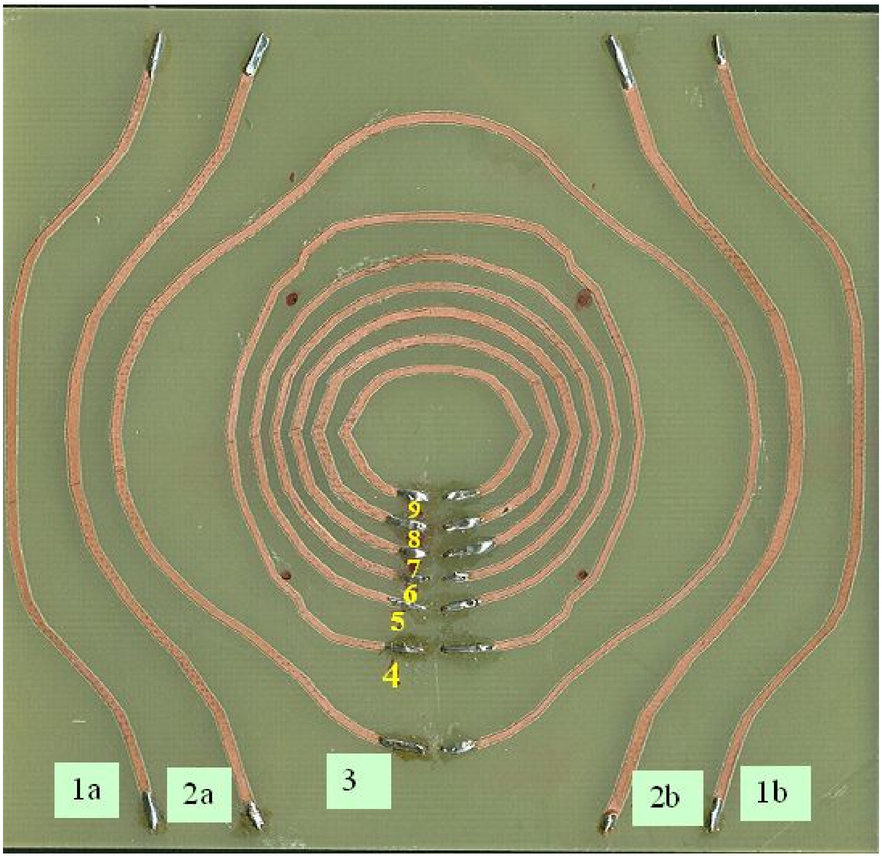

Figure 4.12: Realized RF coil. The wires that carry the same current magnitudes are interconnected. The wire strips labeled as 1a-1b-6-8; 3-4; 2a-2b-5-9; 7 form four independent current paths.

The conductor paths in Figure 4.11 which carry currents that are close in magnitude are interconnected such that there are 4 main currents flowing through the conductor pattern. These current values are calculated using the procedure in Chapter 3 and produced by the emitter currents of the simple circuit illustrated in Figure 4.13.

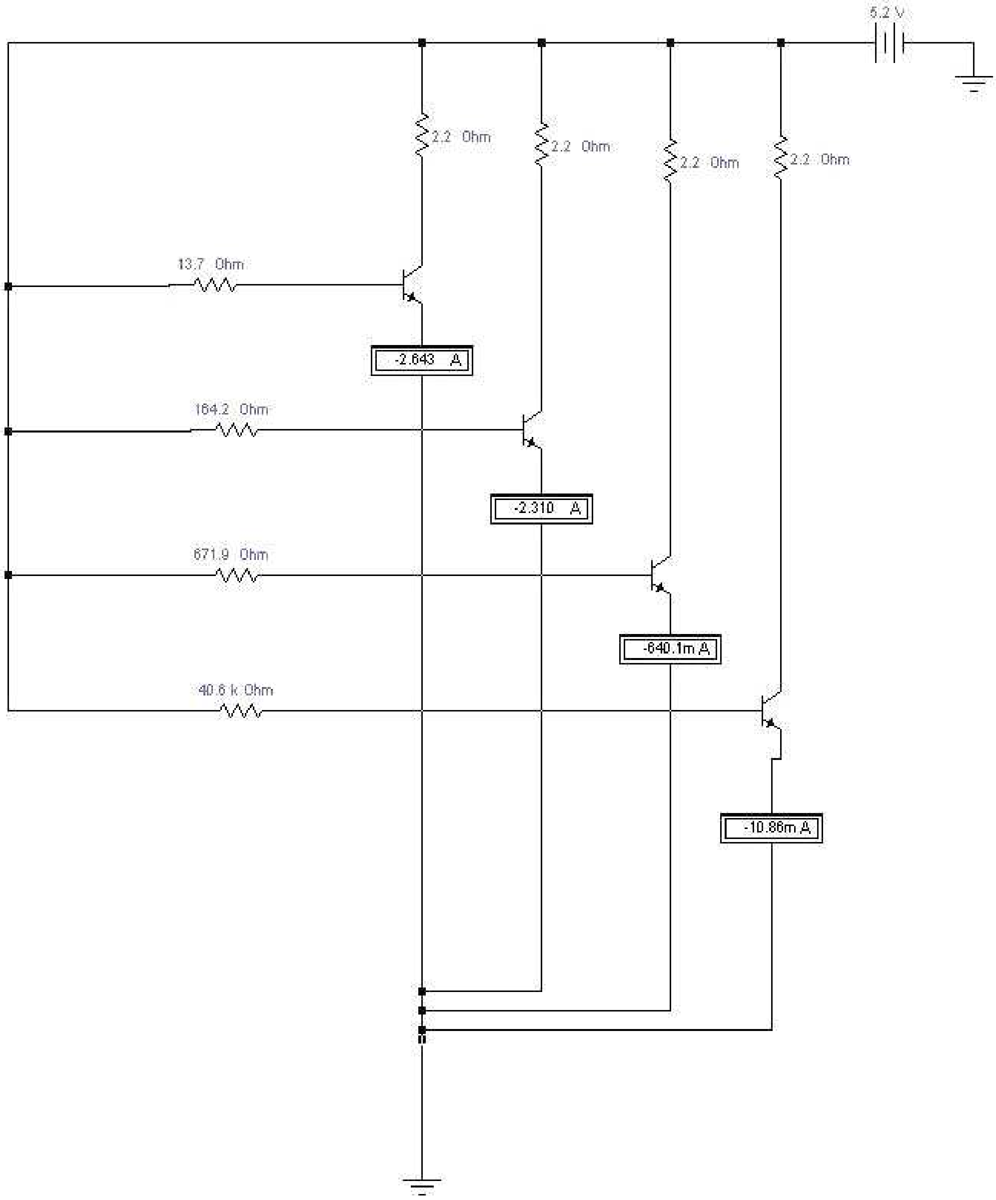

Figure 4.13: Circuit to provide DC currents. The currents to feed the RF coil wire are obtained by the emitter currents of each branch.

This circuit design is realized and the DC currents produced by the circuit are applied to the planar RF coil. The y component of the magnetic field produced by the RF coil is measured using the 3-Channel Gauss meter. Three measurement experiments were carried out and the measurements were recorded for the field points using the same orientation convention.

The planar surface is chosen to be a square plane of $10 \times 10cm$ and the target field is chosen to be a cube of $3.3 \times 3.3 \times 3.3cm$ the center of which is placed $5cm$ away from the surface of the square plane. The magnetic field generated by the RF coil is measured in 200 field points with the same orientation convention in 8 slices in y direction and 5 by 5 grid on xz plane. The experimental setup for the measurement is illutrated in Figure 4.14. Two parallel plates are placed on four rods and the height of the plates are determined by screws on each rod. The plates both have holes in 15 by 15 grid on 10 cm by 10cm area. The probe is inserted in each matching hole so that both the planar location is determined and the probe is double fixed with the help of two reciprocal holes. The distance of the probe in depth is determined by changing the height of the upper plate with the help of screws. The coil, meanwhile, is kept steady in location under the plates inside the measurement setup.

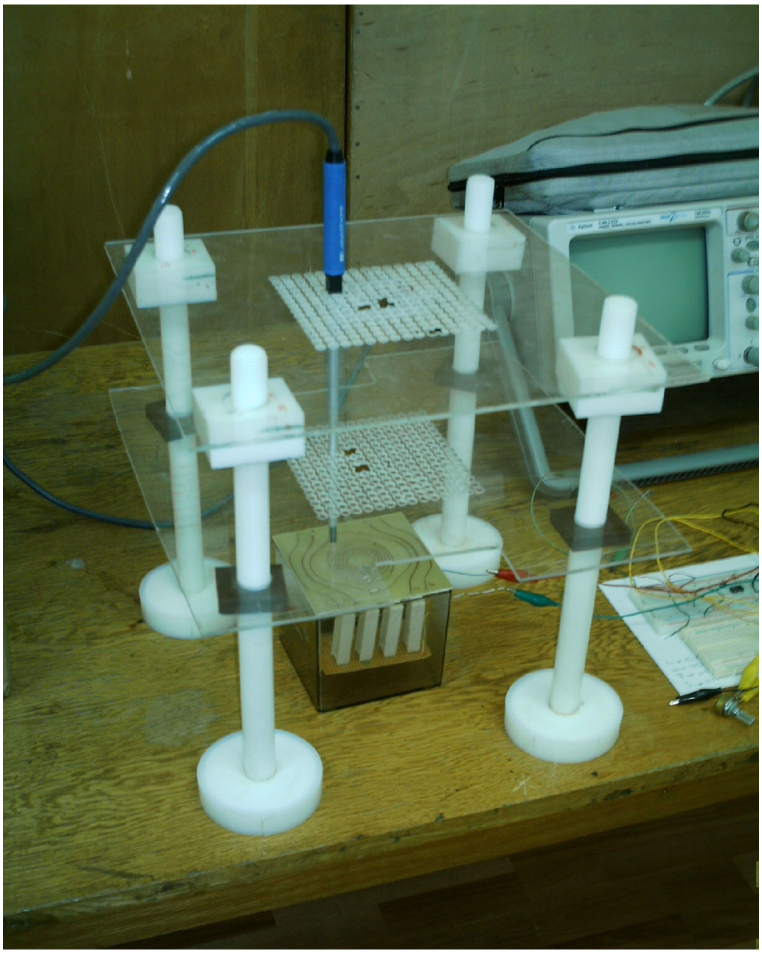

Figure 4.14: Experimental setup for the measurements. Two parallel plates are placed on four rods and the height of the plates are determined by screws on each rod.

The normalized magnetic field results for each measurement are illustrated in Figure 4.15, 4.16 and 4.17. The magnetic field values measured for the RF coil are compared to the theoretical values at the corresponding field points which is illustrated in Figure 4.18.

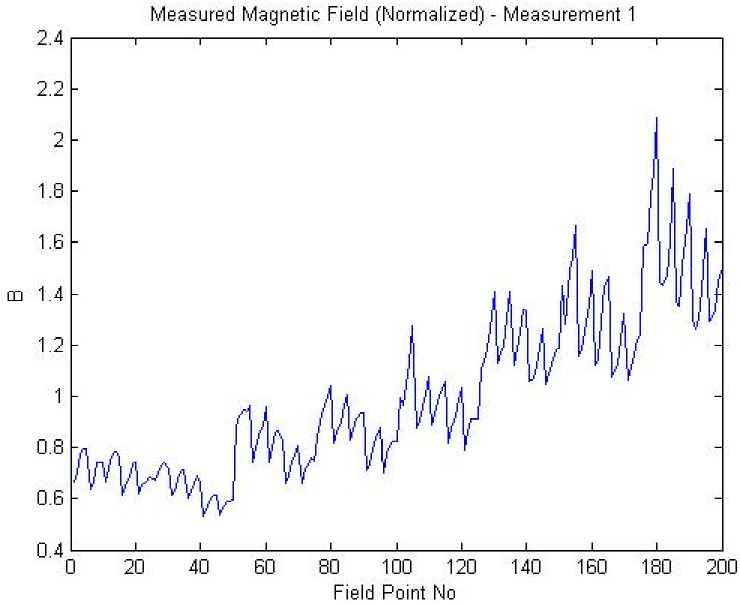

Figure 4.15: Normalized measured magnetic field - Measurement 1. y-component of the magnetic field is measured using the LakeShore 3-Channel Gaussmeter. The target volume is a cube of dimensions 3.3cm by 3.3cm by 3.3cm. The target volume is divided into 5, 8 and 5 divisions in x, y and z directions respectively yielding 200 field points

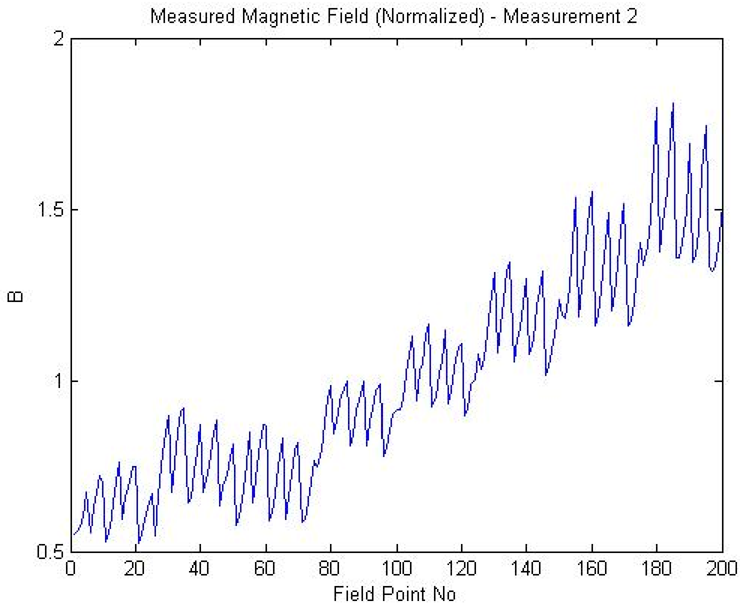

Figure 4.16: Normalized measured magnetic field - Measurement 2. Second measurement is done on the y-component of the magnetic field using the LakeShore 3-Channel Gaussmeter under similar conditions.

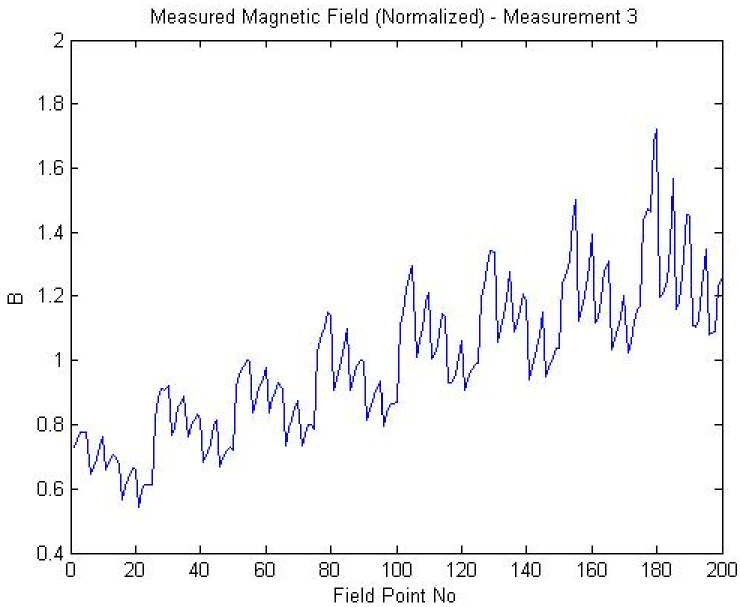

Figure 4.17: Normalized measured magnetic field - Measurement 3. Third measurement is done on the y-component of the magnetic field using the LakeShore 3-Channel Gaussmeter under similar conditions.

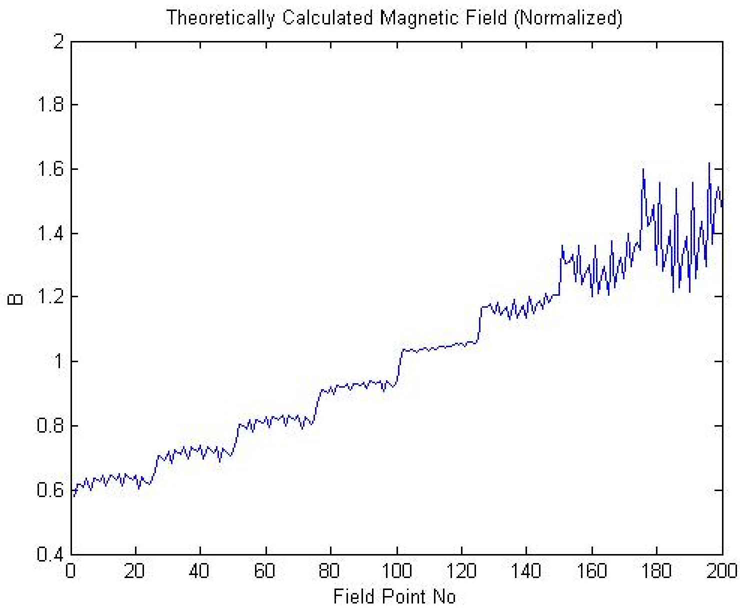

Figure 4.18: Calculated magnetic field. y-component of the magnetic field is calculated considering the streamlines as conductor paths. The target volume is a cube of dimensions 3.3cm by 3.3cm by 3.3cm. The target volume is divided into 5, 8 and 5 divisions in x, y and z directions respectively yielding 200 field points

The error percentages between the measured and calculated magnetic field values are calculated using Equation 4.1, which are stated in Table 4.15.

Table 4.15: Error percentages between desired, calculated and measured Fields

	Measurement 1	Measurement 2	Measurement 3
Error % between the calculated and measured fields	2.13 %	1.98 %	1.92 %
Error % between the desired and measured fields	9.78 %	7.26 %	5.21 %

4.2.3 Tuning and Matching the RF Coil

As the RF Coil is designed to operate in 0.15 Tesla MRI system, it should be tuned to 6.387 MHz and matched to 50 Ohms. Another requirement on the RF coil is that four conductor paths should carry different currents. Therefore, each branch is matched to a real impedance such that it passes the required current and the resultant impedance matches 50 Ohms.

1. In order to measure the inductance of each conductor path, an RLC circuit is set up where each conductor path is connected in series with a resistor of 1Ω and a variable capacitance of $1pF$ sensitivity.

2. The voltage on the resistance is measured by the 54622D Mixed Signal Oscilloscope increasing the capacitance value at a constant frequency.

3. Maximum voltage amplitude on the resistor is determined where capacitance totally cancels inductance.

4. Fine tuning is accomplished by the varying the frequency value.

5. The capacitance value at the maximum voltage is recorded and used to calculate the inductance value according to the formula:

$$L = \frac{1}{w^2 C} \tag{4.2}$$

6. Inductance of each conductor path is calculated as stated in Table 4.16.

Table 4.16: Inductance values for conductor paths

	Inductance Value (μH)
Conductor 1	2.05
Conductor 2	2.12
Conductor 3	1.87
Conductor 4	1.62

7. Resistance value of each conductor path is measured to be 0.22 Ohms.

8. Tuning capacitor values for each conductor path is calculated and a sweep operation is carried out such that each conductor path is tuned to 6.387 MHz and matched to the real impedance providing the branch with the required current magnitude and resulting the overall circuit to match 50 Ohms.

The resulting impedance values at operating frequency and capacitor values for each branch is illustrated in Table 4.17 and the resulting circuit is illustrated in Figure 4.19.

Table 4.17: Tuning and matching parameters for conductor paths

	$R_{in}(\Omega)$	X_{in}	$C_{tuning}(nF)$	$C_{matching}(nF)$
Conductor 1	154.75	- 0.3	0.326	4.26800
Conductor 2	303.45	1.56	0.324	3.04800
Conductor 3	100.32	0.01	0.354	5.29840
Conductor 4	19195	0.78	913	0.38345

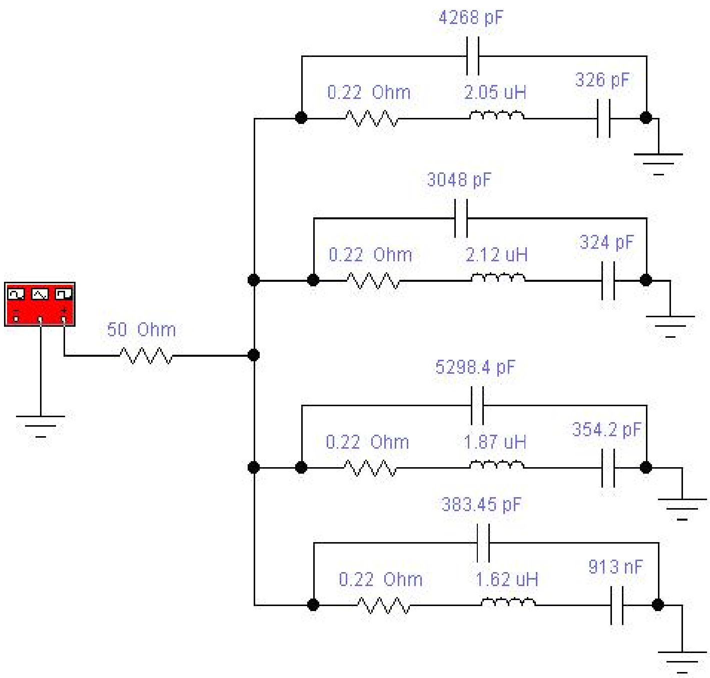

Figure 4.19: Equivalent circuit diagram for the RF coil

The equivalent circuit in series with a resistance of 50Ω is simulated by applying an alternating voltage of $10V$ and the frequency response is investigated. At the operating frequency ($6.873MHz$), the RF coil equivalent circuit almost exactly matched 50Ω (The voltage value is halved corresponding to $5V$ at operating frequency) with a quality factor value of 162.5 as can be visualized in Figure 4.20, Figure 4.21 and Figure 4.22.

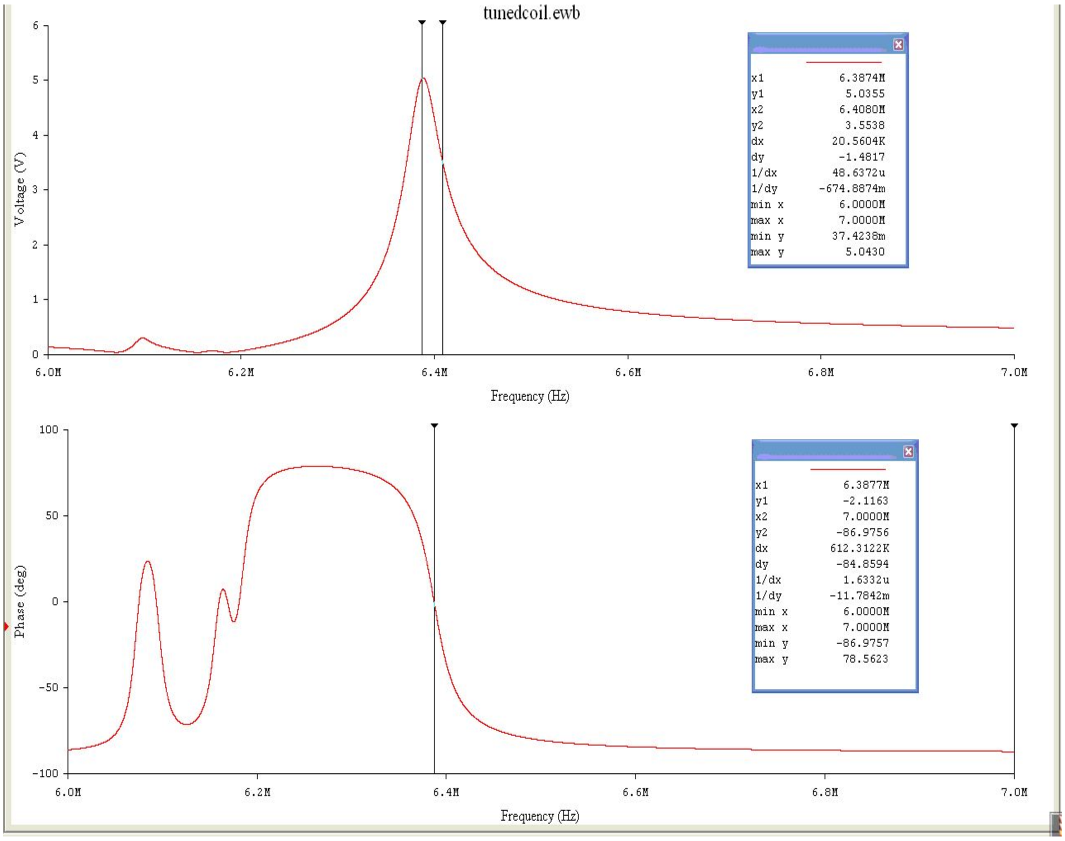

Figure 4.20: Frequency response of the equivalent circuit. Voltage and phase of the equivalent circuit are marked for the operating frequency. Also the frequency where the power of the equivalent circuit is halved is also marked.

x1	6.3874M
y1	5.0355
x2	6.4080M
y2	3.5538
dx	20.5604K
dy	-1.4817
1/dx	48.6372u
1/dy	-674.8874m
min x	6.0000M
max x	7.0000M
min y	37.4238m
max y	5.0430

Figure 4.21: Voltage magnitude on the equivalent circuit at the operating frequency when the coil is considered to be connected in series with a resistance of 50 Ω. At 6.387MHz, the applied voltage of 10V is divided into two; in other words, the coil is matched to 50 Ω.

x1	6.3877M
y1	-2.1163
x2	7.0000M
y2	-86.9756
dx	612.3122K
dy	-84.8594
1/dx	1.6332u
1/dy	-11.7842m
min x	6.0000M
max x	7.0000M
min y	-86.9757
max y	78.5623

Figure 4.22: The phase of the equivalent circuit at the operating frequency when the coil is considered to be connected in series with a resistance of 50 Ω. At 6.387MHz, the phase of the equivalent circuit is nearly zero; in other words, the coil is tuned to 50 Ω.

4.3 Conclusion

Using the algorithm provided in this study, the source and field geometries can be defined as any geometry providing a source field that surrounds or fits a particular part of the patient and a target field that constitutes the volume of an inner part of the body like an organ, vessel... etc.

When the error between the desired and generated magnetic fields is considered, the desired magnetic field is theoretically obtained within acceptable error ranges for several source geometries using regularization methods of different characteristics. However, the characteristics of the required magnetic field affect the success of the algorithm. In other words, any kind of magnetic field can not be created with an error within acceptable limits. Magnetic fields that are more likely to be produced by a surface current density, based on the current density and magnetic field mathematical relations, are created with smaller errors. Magnetic fields that have more homogenous characteristics are created with much less errors than the ones with inhomogeneous characteristics. This is attributed to the averaging effect of regularization algorithms.

Besides, three dimensional surface models give better results for the same required magnetic fields. This is attributed to the compensation of additional surfaces, which are located orthogonally to the single planar surface, to the radically decreasing characteristics of the magnetic field. The tri-planar surface model and orthogonally placed planar surfaces model give similar results for the same magnetic field inputs. However, the problem is solved independently for each coil for the orthogonally placed planar surfaces model. It is speculated that the error between the desired magnetic field and the created field can be diminished by solving the problem when the surfaces are specified to be dependent on each other. The minimum and optimum average error percentage values were smallest for cylindrical surface model for every regularization method.

When current density solutions are considered, the current density distributions producing the minimum average error percentages are harder to implement due to the high magnitude values than the ones producing the optimum average error percentages which have relatively smaller magnitudes.

Stream functions are proved to be reliable tools to provide the conductor pattern to produce the calculated current distribution. The coil patterns corresponding to the current density distributions producing the minimum average error percentages are harder to implement than the ones corresponding to the current density distributions producing the optimum average error percentages for each regularization method.

When conductor pattern solutions with reference to the utilized regularization method are compared, the conductor pattern solutions using Rutisbauer Method are easier to implement. When conductor pattern solutions with reference to the utilized source field geometry are compared, the coil patterns computed for the tri-planar surface by the regularization methods are hard to implement even though the average error percentages are very small.

When the RF coil pattern is realized for the planar coil and the generated magnetic field is both theoretically calculated and experimentally measured, the conductor patterns obtained using stream functions proved both theoretically and experimentally to generate the calculated magnetic fields with a small error.

During the simulation of the circuitry used to tune and match the coil, it is seen that the capacitance values that yield the tuning and matching conditions are very sensitive to small changes. When compared to tuning and matching a conventional RF coil, tuning and matching process is harder to implement as different current magnitudes on conductor branches with different matching requirements should be accomplished at the same time. This requires accurate measurement of the inductance values and capacitances the magnitudes of which can be changed in very small steps.

4.4 Future Work

- The errors on the solenoidal characteristics of the current density due to discritization of the fields on source geometries are aimed to be diminished by increasing the source points which will require parallel processing and iterative algorithms.
- Genetic algorithm is aimed to be adapted to the problem in order to obtain smaller errors with more realizable patterns.
- The signal obtained using the theoretical and experimental magnetic field outcome is aimed to be simulated in an MRI simulator.
- The coil which is realized is aimed to be tuned to multiple frequencies.
- The coil is aimed to be experimented in METU MRI system.
- The coil is aimed to be experimented in inhomogeneous magnetic fields.
- A hand-held MRI scanner is aimed to be implemented and manufactured.

CHAPTER 5

Publications

5.1 Publications Prior to M. Sc. Study

H. Yiğitler, A. Ozan Yılmaz, B. Murat Eyüboğlu, "An approach to geometrical design of permanent magnets for biomedical applications", 11th. International Biomedical Science and Technology Days, Ankara - Turkey, p.24, 2004.

5.2 Publications during M. Sc. Study

A. Ozan Yılmaz, B. Murat Eyüboğlu,"Homojen Olmayan Ana Manyetik Alanda Manyetik Rezonans Görüntüleme için RF sargısı Tasarımı" Proc. of URSI-Türkiye 2006 3rd National Congress, Ankara - TR, pp.207-9, 2006

A. Ozan Yılmaz, B. Murat Eyüboğlu, "RF Coil Design for MRI Applications in Inhomogeneous Main Magnetic Fields", World Congress 2006, Seoul-Korea, p.3084, August 2006.

REFERENCES

[1] F. Bloch, "Nuclear induction," *Physical Review*, vol. 70, pp. 460–474, 1946.

[2] F. Bloch, W. W. Hansen, and M. Packard, "The nuclear induction experiment," *Physical Review*, vol. 70, pp. 474–485, 1946.

[3] E. M. Purcell, H. C. Torrey, and R. V. Pound, "Resonance absorption by nuclear magnetic moments in a solid," *Physical Review*, vol. 69, pp. 37–38, 1946.

[4] P. C. Lauterbur, "Image formation by induced local interactions - examples employing nuclear magnetic-resonance," *Nature*, vol. 242, pp. 190–191, 1973.

[5] R. Damadian, M. Goldsmith, and L. Minkoff, "Nmr in cancer: Xvi. fonar image of the live human body," *Physiological Chemistry and Physics*, vol. 9, pp. 97–100, 1977.

[6] F. Bálibanu, K. Hailu, R. Eymael, D. E. Demco, and B. Blümich, "Nuclear magnetic resonance in inhomogeneous magnetic fields," *Journal of Magnetic Resonance*, vol. 145, pp. 246–258, 2000.

[7] S. Anferova, V. Anferov, M. Adams, P. Blümler, N. Routley, K. Hailu, K. Kupferschläger, M. Malett, G. Schroeder, S. Sharma, and B. Blümich, "Nuclear magnetic resonance in inhomogeneous magnetic fields," *Concepts in Magnetic Resonance*, vol. 15, pp. 15–25, 2002.

[8] F. Casanova and B. Blümich, "Two dimensional imaging with single-sided nmr probe," *Journal of Magnetic Resonance*, vol. 163, pp. 38–45, 2003.

[9] J. Perlo, F. Casanova, and B. Blümich, "3d imaging with a single-sided sensor: an open tomograph," *Journal of Magnetic Resonance*, vol. 166, pp. 228–235, 2004.

[10] M. Brown, D. Verganelakis, M. Mallett, J. Mitchell, and P. Blümler, "Surface normal imaging with a hand-held nmr device," *Journal of Magnetic Resonance*, vol. 169, pp. 308–312, 2004.

[11] P. J. Prado, "Single sided imaging sensor," *Magnetic Resonance Imaging*, vol. 21, pp. 397–400, 2003.

[12] D. A. Thayer, "Imaging techniques and hardware for inhomogeneous mri," Master's thesis, Brigham Young University, December 2004.

[13] H. Yigitler, "Permanent magnet design and image reconstruction technique for magnetic resonance imaging in inhomogeneous magnetic fields," Master's thesis, Middle East Technical University, September 2006.

[14] C. E. Hayes, W. A. Edelstein, J. F. Schenck, O. M. Mueller, and M. Eash, "An efficient, highly homogeneous radiofrequency coil for whole-body nmr imaging at 1.5t," *Journal of Magnetic Resonance*, vol. 63, pp. 622–628, 1985.

[15] J. Tropp, "The theory of the bird-cage resonator," *Journal of Magnetic Resonance*, vol. 82, pp. 51–62, 1989.

[16] J. Tropp, "The theory of an arbitrary perturbed bird-cage resonator, and a simple method for restoring it to full symmetry," *Journal of Magnetic Resonance*, vol. 95, pp. 235–243, 1991.

[17] F. D. Doty, G. Entzminger, and C. D. Hauch, "Error-tolerant rf litz coils for nmr/mri," *Journal of Magnetic Resonance*, vol. 140, pp. 17–31, 1999.

[18] D. A. Roberts, E. K. Insko, L. Bolinger, and J. S. Leigh, "The theory of an arbitrary perturbed bird-cage resonator, and a simple method for restoring it to full symmetry," *Journal of Magnetic Resonance*, vol. A102, pp. 34–41, 1993.

[19] J. Jin, *Electromagnetic Analysis and Design in Magnetic Resonance Imaging.* FL CRC, 1999.

[20] D. Ballon, S. M. M. C. Graham, and J. A.Koutcher, "A64 mhz half-birdcage resonator for clinical imaging," *Journal of Magnetic Resonance*, vol. 90, pp. 131–140, 1990.

[21] J. Gasson, I. R. Summers, M. E. Fry, and W.Vennart, "Modified birdcage coils for target imaging," *Mag. Reson. Imag.*, vol. 13, pp. 1003–1012, 1995.

[22] K. L. Zakian, J. A. Koutcher, and D. Ballon, "A dual-tuned resonator for proton-decoupled phosphorus-31 chemical shift imaging of the brain," *Magn. Reson. Med.*, vol. 41, no. 4, pp. 809–815, 1999.

[23] K. L. Meyer, K. Kim, T. Li, P. K. Tulipano, K. M. Lee, R. DeLaPaz, J. Hirsch, and D. Ballon, "Sensitivity-enhanced echo-planar mri at 1.5 t using a 5x5 mesh dome resonator," *Magn. Reson. Med.*, vol. 36, no. 4, pp. 606–612, 1996.

[24] D. A. Molyneux and A. H. Qureshi, "Quadrature coil system for simultaneous reception," *IEEE Transactions on Magnetics*, vol. 29, pp. 2470–2472, November 1993.

[25] D. A. Molyneux and A. H. Qureshi, "Quadrature coil system for simultaneous reception," *IEEE Transactions on Magnetics*, vol. 32, pp. 5124–5126, September 1996.

[26] R. F. Lee, C. R. Westgate, R. G. Weiss, D. C. Newman, and P. A. Bottomley, "Planar strip array for mri," *Magnetic Resonance in Medicine*, vol. 45, pp. 673–683, 2001.

[27] Z. Zhang, K. Ugurbil, and W. Chen, "Microstrip rf surface coil design for extremely high-field mri and spectroscopy," *Magnetic Resonance in Medicine*, vol. 46, pp. 443–450, 2001.

[28] Q. Y. Ma, "Rf applications of high temperature superconductors in mhz range," *IEEE Transactions on Applied Superconductivity*, vol. 9, pp. 3565–3568, June 1999.

[29] Q. Y. Ma, K. C. Chan, D. F. Kacher, E. Gao, M. S. Chow, K. K. Wong, H. Xu, E. S. Yang, G. S. Young, J. R. Miller, and F. A. Jolesz, "Superconducting rf coils for clinical mr imaging at low field," *Acad Radiol*, vol. 10, pp. 978–987, 2003.

[30] J.-C. Ginefri, L. Darrasse, and P. Crozat, "High-temperature superconducting surface coil for in vivo microimaging of the human skin," *Magnetic Resonance in Medicine*, vol. 45, pp. 376–382, 2001.

[31] M. A. Martens, L. S. Petropoulos, R. Brown, and J. H. Andrews, "Insertable biplanar gradient coils for magnetic resonance imaging," *Rev. Sci. Instrum.*, vol. 62, pp. 2639–2645, Nov 1991.

[32] H. Fujita, L. S. Petropoulos, M. A. Morich, S. M. Shvartsman, and R. W. Brown, "A hybrid inverse approach applied to the design of lumpedelement rf coils," *IEEE Trans. Biomed. Eng.*, vol. 46, pp. 353–361, Mar 1999.

[33] B. G. Lawrence, S. Crozier, D. Yau, and D. Doddrell, "A time-harmonic inverse methodology for the design of rf coils in mri," *IEEE Trans. Biomed. Eng.*, pp. 64–71, Jan 2002.

[34] B. G. Lawrence, S. Crozier, G. Cowin, and D. D. Yau, "An inverse design of an open, head/neck rf coil for mri," *IEEE Trans. Biomed. Eng.*, vol. 49, pp. 1024–1030, September 2002.

[35] P. T. While, L. K. Forbes, and S. Crozier, "A time-harmonic target-field method for designing unshielded rf coils in mri," *Measurement Science and Technology*, vol. 16, pp. 997–1006, 2005.

[36] L. T. Müftüler, G. Chen, and O. Nalcıoğlu, "An inverse method to design rf coil arrays optimized for sense imaging," *Physics in Medicine and Biology*, vol. 51, pp. 6457–6469, 2006.

[37] Z.-P. Liang and P. C. Lauterbur, *Principles of Magnetic Resonance Imaging.* IEEE.

[38] J. Pauly, D. Nishimura, and A. Macovski, "A k-space analysis of small-tip-angle excitation," *Journal of Magnetic Resonance*, vol. 81, pp. 43–56, 1989.

[39] R. F. Harrington, *Field Computation by Moment Methods.* The Machmillan Company, 1968.

[40] D. K. Cheng, *Field and Wave Electromagnetics.* Addison-Wesley Company.

[41] M. A. Bridgeson, L. K. Forbes, and S. Crozier, "Determining complicated winding patterns for shim coils using stream functions and the target-field method," *Concepts Magn. Reson.*, vol. 14, pp. 9–18, 2002.

[42] O. C. Lingjearde and N. Christophersen, *Regularization Principles Solving Ill-Posed Inverse Problems.* September 1998.

[43] R. J. L. Montero, *Pulse-Echo Image Formation using non-quadratic regularization with speckle-based images.* Pontificia Universidad Catolica del Peru, 2002.

[44] G. Mallinson, "The calculation of the lines of a three dimensional vector field," *Computation Fluid Mechanics*, pp. 525–534, 1988.

[45] D. Knight and G. Mallinson, "Visualizing unstructured flow data using dual stream functions," *IEEE Transactions on Visualization and Computer Graphics*, vol. 2, pp. 355–363, December 1996.

[46] P. C. Hansen, *Rank-Deficient and Discrete Ill-Posed Problems: Numerical Aspects of Linear Inversion.* SIAM.

[47] J. P. Reilly, "Matrix computations for signal processing." Department of Electrical and Computer Engineering, McMaster University, February 1998.

[48] G. H. Golub and C. F. V. Loan, *Matrix Computations.* the Johns Hopkins University Press, 3 ed., 1996.

[49] A. J. Laub, *Matrix Analysis for Scientists and Engineers.* SIAM.

[50] H. Zha and P. C. Hansen, "Regularization and the general gauss-markov linear model," *Physics in Medicine and Biology*, vol. 55, pp. 613–624, October 1990.

[51] C. Paige, "Fast numerically stable computations for generalized linear least squares problems," *SIAM Journal on Numerical Analysis*, vol. 16, pp. 165–171, February 1979.

[52] G. H. Golub, P. C. Hansen, and D. P. O'Leary, "Tikhonov regularization and total least squares," *SIAM Journal on Numerical Analysis*, vol. 16, pp. 165–171, February 1979.

APPENDIX A

Regularization

A.1 Singular Value Decomposition

Every matrix $A \in R^{m,n}$ has a SVD:

$$A = U_0 D_0 V_0^T = \left(U \tilde{U} \right) \begin{pmatrix} D & 0 \\ 0 & 0 \end{pmatrix} \begin{pmatrix} V^T \\ \tilde{V}^T \end{pmatrix} = U D V^T \tag{A.1}$$

where $U_0 \in R^{n,n}$ and $V_0 \in R^{m,m}$ are orthogonal (i.e. $U_0^T U_0 = I$ and $V_0^T V_0 = I$) and $U \in R^{m,r}$, $D \in R^{r,r}$ and $V \in R^{m,r}$, where $r \leq \min{(n,m)}$ is the rank of A . The diagonal matrix D , has nonnegative diagonal elements appearing in non increasing order such that

$$\sigma_1 \geq \sigma_2 \geq \cdots \geq \sigma_r > 0 \tag{A.2}$$

Let $u_1, u_2, \ldots, u_n$ denote the column vectors of U_0 and $v_1, v_2, \ldots, v_m$ the column vectors of V_0 . Then, $u_1, u_2, \ldots, u_r$ span $\Re(A)$, $u_{r+1}, u_2, \ldots, u_n$ span $N(A^T)$, $v_1, v_2, \ldots, v_r$ span $\Re(A^T)$ and $v_{r+1}, v_2, \ldots, v_m$ span $N(A)$. It can be observed that $v_1, v_2, \ldots, v_m$ are the eigenvectors of $A^T A$ while $u_1, u_2, \ldots, u_n$ are the eigenvectors of AA^T . Furthermore, $\sigma_1^2, \ldots, \sigma_r^2$ are the non-zero eigenvalues of these matrices.

If the mapping Ax of an arbitrary vector x is considered, using the SVD

$$x = \sum_{i=1}^{n} \left(v_i^T x\right) \; v_i \tag{A.3}$$

$$Ax = \sum_{i=1}^{n} \sigma_i \left(v_i^T x\right) \; u_i \tag{A.4}$$

these relations clearly show that due to multiplication with the σ_i , the high frequency components of x are more damped in Ax than the low frequency components. Moreover, the inverse problem, that computes x from $Ax = b$ or $\min \|Ax - b\|_2$, must have the opposite effect; it amplifies the high-frequency oscillations in the right-hand side b [46].

A.2 The Generalized Singular Value Decomposition (GSVD)

The GSVD of the matrix pair (A, L) is a generalization of the SVD of A in the sense that the generalized singular values of (A, L) are essentially the square roots of the generalized eigenvalues of the matrix pair $\left(A^T A,\; L^T L\right)$. We assume that the dimensions of $A \in R^{mxn}$ and $L \in R^{pxn}$ satisfy $m \geq n \geq p$, which is always the case in connection with discrete ill-posed problems. We also assume that $N(A) \bigcap N(L) = \{0\}$ and that L has a full rank. Then the GSVD is decomposition of A and L in the form

$$A = U \begin{pmatrix} D & 0 \\ 0 & I_{n-p} \end{pmatrix} X^{-1}, \qquad L = V\,(M,\; 0)\,X^{-1} \tag{A.5}$$

The columns of $U \in R^{mxn}$ and $V \in R^{pxp}$ are orthonormal, $U^T U = I_n$ and $V^T V = I_p$; $X \in R^{nxn}$ is nonsingular with columns that are $A^T A$ -orthogonal; and D and M are pxp diagonal matrices with diagonal terms $\sigma_1, \ldots, \sigma_p$ and $\mu_1, \ldots, \mu_p$ respectively. Moreover, the diagonal elements are nonnegative and ordered such that

$$0 \leq \sigma_1 \leq \cdots \leq \sigma_p \leq 1 \,, \qquad 1 \geq \mu_1 \geq \cdots \geq \mu_p > 0 \tag{A.6}$$

and they are normalized such that

$$\sigma_i^2 + \mu_i^2 = 1 \ , \qquad i = 1, \ldots, p \tag{A.7}$$

The generalized singular values of the pair (A, L) are then

$$\gamma_i = \frac{\sigma_i}{\mu_i}, \qquad i = 1, \ldots, p. \tag{A.8}$$

A.3 QR Decomposition

The QR decomposition of a mxn matrix A is given by:

$$A = QR \tag{A.9}$$

where $Q \in R^{mxm}$ is orthogonal and $R \in R^{mxn}$ is upper triangular. If $m \geq n$, the QR decomposition takes on the following form:

$$\begin{array}{cccccc} m & \begin{bmatrix} \\ A \\ \\ \end{bmatrix} & = & \begin{bmatrix} & & \\ & Q & \\ & & \end{bmatrix} & \begin{bmatrix} R_1 \\ 0 \end{bmatrix} & \begin{array}{c} n \\ m-n \end{array} \\ & n & & m & n & \end{array} \tag{A.10}$$

where $R_1 \in R^{nxn}$ is upper triangular [47]. If A has full column rank, then the first n columns of Q form an orthonormal basis for $\Re(A)$ [48]. Thus, calculation of QR decomposition is one way to compute an orthonormal basis for a set of vectors. This computation can be arranged in several ways.

A.3.1 Householder Transformation

Let $v \in R^n$ to be nonzero. A nxn matrix P of the form

$$P = I - \frac{2}{v^T v} v v^T \tag{A.11}$$

is called a *Householder reflection.* The vector v is called a *Householder vector.* If a vector x is multiplied by P , then it is reflected in the hyperplane span $\{v\}^{\perp}$ [48]. In particular, suppose we are given $0 \neq x \in R^n$ and we want Px to be a multiple of $e_1 = I_n(:, 1)$. Using A.11 and setting $v = x + \alpha e_1$ gives:

$$v^T x = x^T x + \alpha x_1 \tag{A.12}$$

and

$$v^T v = x^T x + 2\alpha x_1 + \alpha^2 \tag{A.13}$$

and therefore,

$$Px = \left(1 - 2\frac{x^T x + \alpha x_1}{x^T x + 2\alpha x_1 + \alpha^2}\right) x - 2\alpha \frac{v^T x}{v^T v} e_1 \tag{A.14}$$

In order for the coefficient of x to be zero, $\alpha = \mp \|x\|_2 e_1$. During the utilization of this transformation in this study, the normalized Householder vector $v \in R^n$ is calculated with $v(1) = 1$ and $\beta \in R$ such that $P = I_n - \beta v v^T$ is orthogonal and $Px = \|x\|_2 e_1$.

In order to visualize QR decomposition utilizing Householder transformation, suppose $m = 6, \quad n = 5$ and assume that Householder matrices H_1 and H_2 have been computed so that

$$H_2 H_1 A = \begin{bmatrix} \times & \times & \times & \times & \times \\ 0 & \times & \times & \times & \times \\ 0 & 0 & \otimes & \times & \times \\ 0 & 0 & \otimes & \times & \times \\ 0 & 0 & \otimes & \times & \times \\ 0 & 0 & \otimes & \times & \times \end{bmatrix} \tag{A.15}$$

Based on the marked entries, a Householder matrix $\tilde{H}_3 \in R^{4x4}$ is determined such that

$$\tilde{H}_3 \begin{bmatrix} \otimes \\ \otimes \\ \otimes \\ \otimes \end{bmatrix} = \begin{bmatrix} \times \\ 0 \\ 0 \\ 0 \end{bmatrix} \tag{A.16}$$

If $H_3 = diag\left(I_2, \tilde{H}_3\right)$, then

$$H_3 H_2 H_1 A = \begin{bmatrix} \times & \times & \times & \times & \times \\ 0 & \times & \times & \times & \times \\ 0 & 0 & \times & \times & \times \\ 0 & 0 & 0 & \times & \times \\ 0 & 0 & 0 & \times & \times \\ 0 & 0 & 0 & \times & \times \end{bmatrix} \tag{A.17}$$

after n such steps an upper triangular matrix $R = H_n H_{n-1} \cdots H_1 A$ is obtained and so by setting $Q = H_1 \cdots H_n$ we obtain $A = QR$.

A.3.2 Givens Rotations

Householder reflections are useful on the annihilation of all but the first component of a vector. However, in calculations where it is necessary to zero elements more selectively, *Givens Rotations* are the transformation of choice. A Givens Rotation is defined as:

$$G\left(i,\,k,\,\theta\right) = \begin{array}{cc} \begin{bmatrix} 1 & \cdots & 0 & \cdots & 0 & \cdots & 0 \\ \vdots & \ddots & \vdots & & \vdots & & \vdots \\ 0 & \cdots & c & \cdots & s & \cdots & 0 \\ \vdots & & \vdots & \ddots & \vdots & & \vdots \\ 0 & \cdots & -s & \cdots & c & \cdots & 0 \\ \vdots & & \vdots & & \vdots & \ddots & \vdots \\ 0 & \cdots & 0 & \cdots & 0 & \cdots & 1 \end{bmatrix} & \begin{array}{c} \\ \\ i \\ \\ k \\ \\ \\ \end{array} \\ \begin{array}{ccccccc} \quad & i & \quad & k & \quad & \quad & \quad \end{array} & \end{array} \tag{A.18}$$

where $c = \cos\left(\theta\right)$ and $s = \sin\left(\theta\right)$. Givens Rotations are clearly orthogonal.

Premultiplication by $G\left(i,\,k,\,\theta\right)^T$ amounts to a counter clockwise rotation of θ radians in the (i, k) coordinate plane. If $x \in R^n$ and $y = G\left(i,\,k,\,\theta\right)^T x$, then

$$y_k = \begin{cases} cx_i - sx_k & j = i \\ sx_i + cx_k & j = k \\ x_j & j \neq i, k \end{cases} \tag{A.19}$$

Therefore, y_k can be forced to be zero by setting

$$c = \frac{x_i}{\sqrt{x_i^2 + x_k^2}} \qquad s = \frac{-x_k}{\sqrt{x_i^2 + x_k^2}} \tag{A.20}$$

$c = \cos\left(\theta\right)$ and $s = \sin\left(\theta\right)$ is computed so that

$$\begin{bmatrix} c & s \\ -s & c \end{bmatrix}^T \begin{bmatrix} a \\ b \end{bmatrix} = \begin{bmatrix} \tau \\ 0 \end{bmatrix} \tag{A.21}$$

The general idea in the usage of Givens Rotations to compute QR factorization can be illustrated by a $4x3$ case:

$$
\begin{bmatrix} \times & \times & \times \\ \times & \times & \times \\ \times & \times & \times \\ \times & \times & \times \end{bmatrix} \underset{\rightarrow}{(3,4)} \begin{bmatrix} \times & \times & \times \\ \times & \times & \times \\ \times & \times & \times \\ 0 & \times & \times \end{bmatrix} \underset{\rightarrow}{(2,3)} \begin{bmatrix} \times & \times & \times \\ \times & \times & \times \\ 0 & \times & \times \\ 0 & \times & \times \end{bmatrix} \underset{\rightarrow}{(1,2)}
$$

$$
\begin{bmatrix} \times & \times & \times \\ 0 & \times & \times \\ 0 & \times & \times \\ 0 & \times & \times \end{bmatrix} \underset{\rightarrow}{(3,4)} \begin{bmatrix} \times & \times & \times \\ 0 & \times & \times \\ 0 & \times & \times \\ 0 & 0 & \times \end{bmatrix} \underset{\rightarrow}{(2,3)} \begin{bmatrix} \times & \times & \times \\ 0 & \times & \times \\ 0 & 0 & \times \\ 0 & 0 & \times \end{bmatrix} \underset{\rightarrow}{(3,4)} \quad R \tag{A.22}
$$

Therefore, by setting $Q = \prod_j^t G_j$ we obtain $Q^T A = R$ where G_j denotes the *jth* Givens rotation and t denotes the total number of rotations. A given matrix $A \in R^{mxn}$ is overwritten with $m \geq n$ such that $Q^T A = R$, where R is upper triangular and Q is orthogonal.

A.4 Orthogonal Bidiagonalization

Suppose $A \in R^{mxn}$ and $m \geq n$. Orthogonal matrices $U_B \in R^{mxm}$ and $V_B \in R^{nxn}$ can be computed such that

$$
U_B^T A V_B = \begin{bmatrix} d_1 & f_1 & 0 & \cdots & 0 \\ 0 & d_2 & f_2 & & 0 \\ \vdots & \ddots & \ddots & \ddots & \\ 0 & \cdots & & d_{n-1} & f_{n-1} \\ 0 & \cdots & & 0 & d_n \\ 0 & 0 & \cdots & 0 & 0 \end{bmatrix} \tag{A.23}
$$

$U_B = U_1 \cdots U_n$ and $V_B = V_1 \cdots V_{n-2}$ can each be determined as a product of

Householder matrices:

$$\begin{bmatrix} \times & \times & \times & \times \\ \times & \times & \times & \times \\ \times & \times & \times & \times \\ \times & \times & \times & \times \\ \times & \times & \times & \times \end{bmatrix} \overset{U_1}{\rightarrow} \begin{bmatrix} \times & \times & \times & \times \\ 0 & \times & \times & \times \\ 0 & \times & \times & \times \\ 0 & \times & \times & \times \\ 0 & \times & \times & \times \end{bmatrix} \overset{V_1}{\rightarrow} \begin{bmatrix} \times & \times & 0 & 0 \\ 0 & \times & \times & \times \\ 0 & \times & \times & \times \\ 0 & \times & \times & \times \\ 0 & \times & \times & \times \end{bmatrix} \overset{U_2}{\rightarrow}$$

$$\begin{bmatrix} \times & \times & 0 & 0 \\ 0 & \times & \times & \times \\ 0 & 0 & \times & \times \\ 0 & 0 & \times & \times \\ 0 & 0 & \times & \times \end{bmatrix} \overset{V_2}{\rightarrow} \begin{bmatrix} \times & \times & 0 & 0 \\ 0 & \times & \times & 0 \\ 0 & 0 & \times & \times \\ 0 & 0 & \times & \times \\ 0 & 0 & \times & \times \end{bmatrix} \overset{U_3}{\rightarrow} \begin{bmatrix} \times & \times & 0 & 0 \\ 0 & \times & \times & 0 \\ 0 & 0 & \times & \times \\ 0 & 0 & 0 & \times \\ 0 & 0 & 0 & \times \end{bmatrix} \overset{U_4}{\rightarrow}$$

$$\begin{bmatrix} \times & \times & 0 & 0 \\ 0 & \times & \times & 0 \\ 0 & 0 & \times & \times \\ 0 & 0 & 0 & \times \\ 0 & 0 & 0 & 0 \end{bmatrix} \tag{A.24}$$

$A \in R^{mxn}$, $m \geq n$ is overwritten with $U_B^T A V_B = B$ where B is upper bidiagonal and $U_B = U_1 \cdots U_n$ and $V_B = V_1 \cdots V_{n-2}$. The essential part of U_j 's Householder vector is stored in $A(j+1:m, j)$ and the essential part of V_j 's Householder vector is stored in $A(j, j+2:n)$.

If the matrices $U_B = U_1 \cdots U_j \cdots U_n$ and $V_B = V_1 \cdots V_j \cdots V_{n-2}$ are desired explicitly:

$$U_j = I - \beta_j \, u^{(j)} {u^{(j)}}^T \tag{A.25}$$

where

$$u^{(j)} = \left(\underbrace{0 \quad 0 \quad \cdots \quad 0}_{j-1} \quad 1 \quad \underbrace{u_{j+1}^{(j)} \quad \cdots u_m^{(j+1)}}_{essential\ part} \right) \tag{A.26}$$

and

$$V_j = I - \beta_j \, v^{(j)} v^{(j)^T} \tag{A.27}$$

where

$$v^{(j)} = \left(\underbrace{0 \quad 0 \quad \cdots \quad 0}_{j} \quad 1 \quad \underbrace{v_{j+2}^{(j)} \quad \cdots v_n^{(j+1)}}_{essential\ part} \right) \tag{A.28}$$

A.5 Direct Regularization Techniques

A.5.1 Tikhonov Regulatization

The key idea in Tikhonov's method is to incorporate a priori assumptions about the size and the smoothness of the desired solution, in the form of the smoothing semi norm $\|Lx\|_2$. For discrete ill-posed problems, Tikhonov Regularization in general form leads to the minimization problem:

$$\min \left\{ \; \|Ax - b\|_2^2 + \lambda^2 \, \|Lx\|_2^2 \; \right\} \tag{A.29}$$

where the regularization parameter λ controls the weight given to minimization of the regularization term, relative to the minimization of the residual norm. Underlying this formulation, is the assumption that the errors in the right hand side are uncorrelated and with covariance matrix $\sigma_0^2 I_m$. If the covariance matrix is of general form CC^T , where C has full rank m, then one should scale the least squares residual with C^{-1} and solve the scaled problem

$$\min\left\{ \| C^{-1}(Ax-b) \|_2^2 + \lambda^2 \| Lx \|_2^2 \right\} \tag{A.30}$$

The Tikhonov problem has two important alternative formulations:

$$\left(A^TA + \lambda^2 L^T L\right) x = A^T b \qquad \textit{and} \qquad \min \left\| \begin{pmatrix} A \\ \lambda L \end{pmatrix} x - \begin{pmatrix} b \\ 0 \end{pmatrix} \right\|_2 \tag{A.31}$$

The Tikhonov solution $x_{L,\lambda}$ is given by

$$x_{L,\lambda} = A_\lambda^{\#} b \qquad \textit{with} \qquad A_\lambda^{\#} = \left(A^TA + \lambda^2 L^T L\right)^{-1} A^T \tag{A.32}$$

where $A_\lambda^{\#}$ is the Tikhonov regularized inverse. If we insert GSVD of (A, L) into this equation, then the filter factors for Tikhonov regularization in standard form where $L = I_n$ and general form where $L \neq I_n$ are given by

$$f_i = \frac{\sigma_i^2}{\sigma_i^2 + \lambda^2}, \quad L = I_n \qquad \textit{and} \qquad f_i = \frac{\gamma_i^2}{\gamma_i^2 + \lambda^2} \quad L \neq I_n \tag{A.33}$$

For a square invertible L , the alternative formula

$$x_{L,\lambda} = \left(L^TL\right)^{-1} A^T \left(A\left(L^TL\right)^{-1} A^T + \lambda^2 I_m\right)^{-1} b \tag{A.34}$$

occasionally appears in literature.

The method also appears when the least squares problem is augmented with statistical a priori information about the solution, in the form of a covariance matrix $C_x^T C_x$ for the desired solution (considered as a stochastic variable). In this setting, the estimator is the solution to

$$\left(A^T\left(CC^T\right)^{-1}A+\left(C_xC\right)^{-1}\right)x=A^T\left(CC^T\right)^{-1}b \tag{A.35}$$

It can be seen that the estimator is the scaled Tikhonov solution when λL is replaced by C_x^{-1} . In order to solve the Tikhonov problem numerically we should form the matrix $\left(A^TA+\lambda^2L^TL\right)$ and compute its Cholesky factorization [46]. However, forming A^TA explicitly can lead to loss of information in finite-precision arithmetic and a new Cholesky factorization is required for each regularization parameter λ .

Elden's Bidiagonalization Algorithm is the most efficient and numerically stable way to compute the solution to the Tikhonov problem [3]. If the problem is given in the general form $(L \neq I_n)$, then the standard forms of the matrices A and b should be computed using explicit standard-form transformation developed by Elden, which is based on two QR factorizations.

$$L^T=KR=\begin{pmatrix} K_p & K_{n-p}\end{pmatrix}\begin{pmatrix} R_p \\ 0\end{pmatrix} \tag{A.36}$$

$$AK_{n-p}=HT=\begin{pmatrix} H_{n-p} & H_{m-(n-p)}\end{pmatrix}\begin{pmatrix} T_{n-p} \\ 0\end{pmatrix} \tag{A.37}$$

Hence, the standard forms of the matrices A and b are obtained as

$$\begin{aligned}
\bar{A} &= A\left(I_p-K_{n-p}T_{n-p}^{-1}H_{n-p}^{-1}A\right)L^+ && \text{(A.38)}\\
&= \left(I_m-H_{n-p}H_{n-p}^T\right)AL^+\\
&= H_{m-(n-p)}H_{m-(n-p)}^TAL^+\\
\bar{b} &= b-AK_{n-p}T_{n-p}^{-1}H_{n-p}^Tb && \text{(A.39)}\\
&= \left(I_m-H_{n-p}H_{n-p}^T\right)b=H_{m-(n-p)}H_{m-(n-p)}^Tb
\end{aligned}$$

where $L^+=K_pR_p^{-1}$ is the pseudo inverse of the full rank matrix L . Then

Tikhonov problem should be treated as a least squares problem of the form

$$\min \left\| \begin{pmatrix} \bar{A} \\ \lambda I_p \end{pmatrix} \bar{x} - \begin{pmatrix} \bar{b} \\ 0 \end{pmatrix} \right\|_2 \tag{A.40}$$

This problem can be reduced to an equivalent sparse and highly structured problem by transforming $\bar{A}$ into a *pxp* upper triangular matrix $\bar{B}$ by means of left and right orthogonal transformations,

$$\bar{A} = \bar{U}\,\bar{B}\,\bar{V}^T \tag{A.41}$$

Once $\bar{A}$ has been reduced to a bidiagonal matrix $\bar{B}$, we make the substitution $\bar{x} = \bar{V}\,\bar{\xi}$ and obtain the problem:

$$\min \left\| \begin{pmatrix} \bar{B} \\ \lambda L_p \end{pmatrix} \bar{\xi} - \begin{pmatrix} \bar{U}^T b \\ 0 \end{pmatrix} \right\|_2 \tag{A.42}$$

The sub-matrix λL_p can be annihilated by Givens Rotations as explained in *3.1.1*. After λL_p has been removed we arrive at the problem:

$$\min \left\| \begin{pmatrix} \hat{B} \\ 0 \end{pmatrix} \bar{\xi} - \begin{pmatrix} \hat{\beta}_1 \\ \hat{\beta}_2 \end{pmatrix} \right\|_2 \tag{A.43}$$

based on the fact that $\| Ax - b \|_2^2 = \left\| Q^T Ax - Q^T b \right\|_2^2$ [49]. As a result, the solution becomes:

$$\bar{\xi} = \hat{B}^{-1}\hat{\beta}_1 \tag{A.44}$$

We can also incorporate an a priori estimated x^* into the smoothing norm and thus “bias” the regularized solution towards this estimate. The least squares estimation takes the form

$$\min \left\| \begin{pmatrix} A \\ \lambda L \end{pmatrix} x - \begin{pmatrix} b \\ \lambda L x^* \end{pmatrix} \right\|_2 \tag{A.45}$$

and after standard form transformation we have

$$\min \left\| \begin{pmatrix} \bar{A} \\ \lambda I_p \end{pmatrix} \bar{x} - \begin{pmatrix} \bar{b} \\ \lambda \bar{x}^* \end{pmatrix} \right\|_2 \tag{A.46}$$

A.5.1.1 Least Squares with a Quadratic Constraint

There are two other regularization methods which are almost equivalent to Tikhonov's method, and which can be treated numerically by standard form transformation plus bidiagonalization or GSVD. These two methods are formulated as the following least squares problems with a quadratic constraint.

$$\min \|Ax - b\|_2 \qquad \textit{subject to} \qquad \|L\,(x - x^*)\|_2 \leq \alpha, \tag{A.47}$$

$$\min \|L\,(x - x^*)\|_2 \qquad \textit{subject to} \qquad \|Ax - b\|_2 \leq \delta \tag{A.48}$$

where α and δ are nonzero parameters each playing the role of the regularization parameters. The solution to both problems is identical to $x_{L,\lambda}$ from Tikhonov's method. Graphically, the solution to A.25 lies on the intersection of the Tikhonov L-curve and the horizontal line $\|L\,(x - x^*)\|_2 = \alpha$, while the solution to A.26 lies on the intersection of the L-curve and the vertical line $\|Ax - b\|_2 = \delta$.

A.5.1.2 Inequality or Equality Constraints

It is sometimes convenient to add certain contraints to the Tikhonov solution, such as nonnegativity, monotonicity, or convexity. All three constraints can be formulated as inequality constraints of the form $Gx \geq 0$, taking the special forms

$$\begin{aligned} x \geq 0 &\qquad \textit{nonnegativity} \\ L_1 x \geq 0 &\qquad \textit{monotonicity} \\ L_2 x \geq 0 &\qquad \textit{convexity} \end{aligned} \tag{A.49}$$

where L_1 and L_2 approximate the first and second derivative operators, respectively [42]. The constraints can, of course, also be combined in the matrix G. Thus, the inequality-constrained Tikhonov solution solves the problem

$$\min \left\{ \, \| Ax - b \|_2^2 + \lambda^2 \, \| Lx \|_2^2 \right\} \qquad \textit{subject to} \qquad Gx \geq 0 \tag{A.50}$$

The constraints can be in the form of equalities incorporated with total least squares problems [42]. The general form of the linearly restricted least squares problem is

$$\min \| \, Ax - b \, \|_2 \qquad \textit{such that} \qquad Rx = r \tag{A.51}$$

where $R \in R^{pxn}$. In order to solve the problem, method of Lagrangian multipliers is used. The solution is found by minimizing the unconstrained problem

$$\| Ax - b \|_2 - 2\lambda \, (Rx - r) \tag{A.52}$$

with respect to x and $\lambda = (\lambda_1, \ldots, \lambda_p)$ respectively and the following stationary conditions are obtained:

$$2A^T \, (Ax - b) - 2R^T \lambda \;\; = \;\; 0 \tag{A.53}$$

$$Rx - r \;\; = \;\; 0 \tag{A.54}$$

Let $S = A^T A$. From the first equation above,

$$x = S^{-1}A^T b + S^{-1}R^T \lambda = x_{ols} + S^{-1}R^T \lambda \tag{A.55}$$

where $x_{ols} = S^{-1}A^T b$ is the ordinary least squares solution under no restrictions. Multiplying by R and using the second equation:

$$Rx_{ols} + RS^{-1}R^T \lambda = Rx = r \tag{A.56}$$

The symmetric $RS^{-1}R^T$ is positive definite, hence invertible, and it is found that

$$\lambda = \left[RS^{-1}R^T\right]^{-1}(r - Rx_{ols}) \tag{A.57}$$

Inserting this into A.31 yields the solution

$$x = x_{ols} + S^{-1}R^T \left[RS^{-1}R^T\right]^{-1}(r - Rx_{ols}) \tag{A.58}$$

A.5.1.3 Related Methods

The Tikhonov solution can be modified by a process which resembles iterative refinement for linear systems of equations. If the set $x^{(1)} = x_{L,\lambda}$, then the modified Tikhonov solutions are defined recursively as

$$x^{(k+1)} = x^{(k)} + \left(A^T A + \lambda^2 L^T L\right)^{-1} A^T \left(b - Ax^{(k)}\right), \qquad k = 1,\ 2,\ \ldots \tag{A.59}$$

This technique is called *Iterated Tikhonov Regularization* [46].

Another modification of Tikhonov's method for achieving sharper filter factors amounts to solve the following system of equations in the standard form case:

$$\left(A^T A + \lambda^2 I_n + \lambda^2 \left(A^T A + \lambda^2 I_n\right)^{-1}\right) x = A^T b \tag{A.60}$$

The corresponding filter factors are:

$$f_i = \frac{\sigma_i^2}{\sigma_i^2 + \lambda^2 + \lambda^2/(\sigma_i^2 + \lambda^2)} \tag{A.61}$$

For *symmetric positive definite* matrices A and L , Tikhonov's problem is suggested to be replaced with the problem:

$$(A + \lambda L)\, x = b, \qquad \lambda \geq 0 \tag{A.62}$$

If $L = I_n$ then the solution can be expressed in terms of the SVD of A, in the form with filter factors $f_i = \frac{\sigma_i}{\sigma_i + \lambda}$. If $L \neq I_n$ then the solution is most conveniently expressed in terms of the generalized eigenvalues and eigenvectors of (A, L) .

Another variant of Tikhonov regularization is a statistical approach such that the expected value $\varepsilon\left(\left\|x^{exact} - x_{reg}\right\|_2^2\right)$ of the error norm is minimized. It is assumed that $b = b^{exact} + e, \quad x_{reg} = A^{\#} b$, and that the covariance matrix for e is CC^T . Then we obtain

$$\begin{aligned} \varepsilon\left(\left\|x^{exact} - x_{reg}\right\|_2^2\right) &= \left\|x^{exact} - A^{\#} b^{exact}\right\|_2^2 + trace\left(A^{\#} C C^T \left(A^{\#}\right)^T\right) \\ &= \sum_{i=1}^{n} (1 - f_i)^2 \left(v_i^T x^{exact}\right)^2 + \sum_{i=1}^{n} f_i^2 \sigma_i^{-2} \left\|C^T u_i\right\|_2^2 \end{aligned} \tag{A.63}$$

and this quantity is minimized for

$$f_i = \frac{\sigma_i^2}{\sigma_i^2 + \|C^T u_i\|_2^2 \Big/ \left(v_i^T x^{exact}\right)^2}, \qquad i = 1, \ldots, n \tag{A.64}$$

A.5.2 The Regularized General Gauss-Markov Linear Model

The *general Gauss-Markov linear model* is defined as

$$Ax + \varepsilon = b \qquad (62) \tag{A.65}$$

where $A \in R^{mxn}$ $(m \geq n)$ and $b \in R^m$ are known, $x \in R^n$ is an unknown vector to be estimated, and $\varepsilon \in R^m$ is a random vector with zero mean and variance-covariance matrix $V(\varepsilon) = s^2 CC^T$ with $C \in R^{mxq}$ $(m \geq q)$ [50]. The best linear unbiased estimator of x in this model is the solution to the problem:

$$\min \| u \|_2 \qquad \textit{subject to} \qquad Ax + Cu = b \tag{A.66}$$

where $u \in R^q$ such that $\varepsilon = Cu$ and u has the variance-coariance matrix $V(u) = s^2 I_q$

When A is ill-conditioned while B is well-conditioned, a *regularized Gauss-Markov problem* can be proposed as:

$$\min \left\{ \| u \|_2^2 + \lambda^2 \| Lx \|_2^2 \right\} \qquad \textit{subject to} \qquad Ax + Cu = b \tag{A.67}$$

This equation involves three matrices $A,$ C and L where $A \in R^{mxn}$, $C \in R^{mxq}$ and $L \in R^{pxn}$. The appropriate tool for this analysis is the restricted SVD (RSVD) where it is assumed that

$$\begin{aligned} rank\,(C) &= q \leq m, \\ rank\,(L) &= p \leq n \leq m, \\ rank \begin{pmatrix} A \\ L \end{pmatrix} &= n. \end{aligned} \tag{A.68}$$

Then, there exist nonsingular matrices $X \in R^{nxn}$ and $Z \in R^{mxm}$, and orthogonal matrices $U \in R^{qxq}$ and $V \in R^{pxp}$ such that

$$Z^T AX = \Sigma, \qquad Z^T CU = M, \qquad V^T LX = N, \tag{A.69}$$

where Σ , N and M are pseudo diagonal matrices with nonnegative elements having the following structure:

$$\Sigma = \begin{array}{cc} \begin{pmatrix} \Sigma_A & 0 & 0 & 0 \\ 0 & I_j & 0 & 0 \\ 0 & 0 & I_k & 0 \\ 0 & 0 & 0 & I_l \\ 0 & 0 & 0 & 0 \end{pmatrix} & \begin{matrix} s \\ j \\ k \\ l \\ u \end{matrix} \\ \begin{matrix} t & j & k & l \end{matrix} & \end{array} \qquad (66.1) \tag{A.70}$$

$$M = \begin{array}{cc} \begin{pmatrix} I_s & 0 \\ 0 & 0 \\ 0 & I_k \\ 0 & 0 \\ 0 & 0 \end{pmatrix} & \begin{matrix} s \\ j \\ k \\ l \\ u \end{matrix} \\ \begin{matrix} s & k \end{matrix} & \end{array} \qquad N = \begin{array}{cc} \begin{pmatrix} I_t & 0 & 0 & 0 \\ 0 & I_j & 0 & 0 \end{pmatrix} & \begin{matrix} t \\ j \end{matrix} \\ \begin{matrix} t & j & k & l \end{matrix} & \end{array} \tag{A.71}$$

and where

$$\Sigma_A = diag\left(\sigma_1, \ldots, \sigma_{\min(s,t)}\right) \in R^{sxt}, \qquad \sigma_1 \geq \cdots \geq \sigma_{\min(s,t)} > 0$$

$$j = rank\,(A,\ C)\,, \qquad k = n + q - rank \begin{pmatrix} A & C \\ L & 0 \end{pmatrix},$$

$$l = rank \begin{pmatrix} A & C \\ L & 0 \end{pmatrix} - p - q, \qquad s = rank \begin{pmatrix} A & C \\ L & 0 \end{pmatrix} - n \tag{A.72}$$

$$t = ank\,(A,\ C) - rank \begin{pmatrix} A & C \\ L & 0 \end{pmatrix}, \qquad u = m - rank\,(A,\ C)$$

As a result, the solution $x_{L,C,\lambda}$ can be written as

$$x_{L,C,\lambda} = XF_\lambda \Sigma^+ X^T b, \qquad F_\lambda = diag\,(f_1, \ldots, f_t, 1, \ldots, 1) \tag{A.73}$$

where

$$f_i = \frac{\sigma_i^2}{\sigma_i^2 + \lambda^2}, \qquad i = 1, \ldots, t \tag{A.74}$$

As in the case of Tikhonov regularization, it is seen that λ controls the solution's sensitivity to errors in b .

A.5.2.1 Numerical Algorithm

Equation A.67 can be reformulated as:

$$\min \left\| \begin{bmatrix} \lambda L & 0 \\ 0 & I_q \end{bmatrix} \begin{bmatrix} x \\ u \end{bmatrix} \right\| subject\, to \qquad \begin{bmatrix} A & C \end{bmatrix} \begin{bmatrix} x \\ u \end{bmatrix} = b \tag{A.75}$$

A.5.2.1.1 Step1

Make a QR decomposition of C, so that $C = Q\begin{bmatrix} C_1 \\ 0 \end{bmatrix}$, where $C_1 \in R^{qxq}$ is upper triangular and nonsingular.

A.5.2.1.2 Step2

Let

$$Q^T\left[A \;\; b\right] = \begin{array}{cc} \begin{bmatrix} A_1 & b_1 \\ A_2 & b_2 \end{bmatrix} & \begin{array}{c} q \\ m-q \end{array} \end{array} \tag{A.76}$$

and make the following decomposition of A_2 :

$$\begin{array}{ll} A_2U = [\begin{array}{cc} 0 & A_{22} \end{array}] & m-q \qquad (70) \\ \qquad\quad\;\; \begin{array}{cc} n-i & i \end{array} & \end{array} \tag{A.77}$$

so that U is orthogonal and $A_{22} \in R^{(m-q)xi}$ is of full column rank i.

A.5.2.1.3 Step3

Let

$$\begin{bmatrix} A_1 \\ L \end{bmatrix} U = \begin{array}{c} \begin{bmatrix} A_{11} & A_{12} \\ L_1 & L_2 \end{bmatrix} \\ \begin{array}{cc} n-i & i \end{array} \end{array} \qquad \textit{and} \qquad U^Tx = \begin{array}{cc} \begin{bmatrix} x_1 \\ x_2 \end{bmatrix} & \begin{array}{c} n-i \\ i \end{array} \end{array} \tag{A.78}$$

Make a QR decomposition of A_{22} , so that $A_{22} = Q_1\begin{bmatrix} \tilde{A}_{22} \\ 0 \end{bmatrix}$, where $\tilde{A}_{22} \in R^{ixi}$ is upper triangular and nonsingular. Let

$$Q_1^Tb_2 = \begin{bmatrix} b_2^{(1)} \\ b_2^{(2)} \end{bmatrix} \qquad \textit{with } b_2^{(1)} \in R^i \tag{A.79}$$

Then the regularized Gauss-Markov linear model is consistent only if $b_2^{(2)} = 0$ [50]. In this case,

$$x_2 = \tilde{A}_{22}^{-1} b_2^{(1)} \tag{A.80}$$

and x_1 solves the least squares problem:

$$\min \left\| \begin{bmatrix} \lambda L_1 \\ C_1^{-1} A_{11} \end{bmatrix} x_1 - \begin{bmatrix} \lambda L_2 x_2 \\ C_1^{-1} \left(b_1 - A_{12} x_2 \right) \end{bmatrix} \right\| \tag{A.81}$$

This problem can be solved for x_1 using plane rotations and orthogonal transformations [50],[51] giving the unique solution:

$$x = U \begin{bmatrix} x_1 \\ x_2 \end{bmatrix} \tag{A.82}$$

A.5.3 Truncated SVD and GSVD (TSVD and TGSVD)

A different way to treat the ill-conditioning of A is to derive a new problem with a well-conditioned rank-deficient coefficient matrix. This is the idea behind the methods TSVD and TGSVD.

For problems with ill-determined numerical rank, it is not obvious that truncation of the SVD/GSVD leads to regularized solution. However, it is proven that under suitable conditions, for any valid truncation parameter k there always exists a regularization parameter λ such that TSVD/GTSVD solution is close to Tikhonov solution.

The filter factors for these methods simply consist of zeros and ones:

$$\begin{aligned} TSVD: \quad f_i &= \begin{cases} 1, & i \leq k, \\ 0, & i > k \end{cases} \\ TGSVD: \quad f_i &= \begin{cases} 0, & i \leq n-k, \\ 1, & i > n-k \end{cases} \end{aligned} \tag{A.83}$$

A.5.4 Algorithms based on Total Least Squares

In order to explain the basic idea behind this method, consider a moment the usual least squares solution x_{ols} found by minimizing $\|Ax - b\|_2$. It can be seen that x_{ols} solves the problem $Ax = \hat{b}$ where $\hat{b}$ is the smallest possible perturbation if b such that $\hat{b} \in \Re(A)$, i.e, such that $\left\|b - \hat{b}\right\|$ is minimal. In other words, we first perturb b just enough to ensure that the perturbed equation has a solution, and then x_{ols} is found solving this system. If A is also subject to noise, A can be perturbed as well as b . That is, we can try to find $\hat{A}$ and $\hat{b}$ such that $\left\|[A;\, b] - \left[\hat{A}; \hat{b}\right]\right\|$ is as small as possible and such that $\hat{b} \in \Re\left(\hat{A}\right)$. Then $\hat{A}x = \hat{b}$ has a solution, and any such solution is called *total least squares* (TLS) solution of the problem $Ax = b$.

A.5.4.1 Truncated Total Least Squares (TTLS)

TTLS is a modification of TLS, which is also suitable as a regularization method for ill-posed problems. The TTLS solution is usually defined as follows:

Suppose a regularization parameter k has been specified and consider the singular value decomposition

$$[A \;\; b] = \tilde{U}\tilde{D}\tilde{V}^T \tag{A.84}$$

where $\tilde{V} \in R^{(n+1)x(n+1)}$ can be block partitioned as

$$\tilde{V} = \begin{pmatrix} \tilde{V}_{11} & \tilde{V}_{12} \\ \tilde{V}_{21} & \tilde{V}_{22} \end{pmatrix} \tag{A.85}$$

where $\tilde{V}_{11} \in R^{nxk}$. Then the TTLS solution is defined by

$$x_{ttls} = -\frac{\tilde{V}_{12}\tilde{V}_{22}^T}{\left\|\tilde{V}_{22}\right\|_2^2} \tag{A.86}$$

and the filter factors corresponding to $u_i^T \neq 0$ and $\sigma_i \neq 0$ are given by

$$f_i = \sum_{j=1}^{k} \frac{\bar{v}_{n+1,j}^2}{\left\| \tilde{V}_{22} \right\|_2^2} \left(\frac{\sigma_i^2}{\bar{\sigma}_j^2 - \sigma_i^2} \right) \tag{A.87}$$

For $i \leq k$, these filter factors increase monotonically with i and satisfy

$$0 \leq f_i - 1 \leq \frac{\bar{\sigma}_{k+1}^2}{\sigma_i^2 - \bar{\sigma}_{k+1}^2}, \qquad i \leq k, \tag{A.88}$$

while for $k < i < rank\,(A)$, these filter factors satisfy

$$0 \leq f_i \leq \left\| \tilde{V}_{22} \right\|_2^{-2} \frac{\sigma_i^2}{\bar{\sigma}_k^2 - \sigma_i^2}, \qquad k < i < rank\,(A) \tag{A.89}$$

It can be observed that for the first k filter factors, the larger the ratio between σ_i and $\bar{\sigma}_{k+1}$, the closer the bound on f_i to 1 . Similarly, for the last $n-k$ filter factors, it is observed that the smaller the ratio between σ_i and $\bar{\sigma}_k$, the closer f_i is to $\frac{\sigma_i^2}{\bar{\sigma}_k^2}$.

A.5.4.2 Regularized TLS (R-TLS)

An alternative approach to adding regularization to the TLS technique is based on Tikhonov formulation (*). In the TLS setting we add the bound $\| L\,x \|_2 \leq \alpha$ to the ordinary TLS problem and the R-TLS problem thus becomes,

$$\min \left\| \, (A,\, b) - \left(\tilde{A},\, \tilde{b}\right) \, \right\|_F \qquad \textit{subject to} \qquad \tilde{b} = \tilde{A}x, \quad \| \, L\, x \, \|_2 \leq \alpha. \tag{A.90}$$

The R-TLS solution $\bar{x}_\alpha$ to A.55 is a solution to the problem

$$\left(A^T A + \lambda_I I_n + \lambda_L L^T L\right) \, x = A^T b \tag{A.91}$$

where the parameters λ_I and λ_L are given by

$$\begin{aligned} \lambda_I &= -\tfrac{\| \, Ax - b \, \|_2^2}{1 + \| \, x \, \|_2^2}, \\ \lambda_L &= \tfrac{(b - Ax)^T Ax}{\alpha^2} \end{aligned} \tag{A.92}$$

Moreover, the TLS residual satisfies,

$$\left\| \, (A,\, b) - \left(\tilde{A},\, \tilde{b}\right) \, \right\|_F^2 = -\lambda_I \tag{A.93}$$

The expressions for the parameters λ_I , λ_L and the residual are proven using Lagrange multiplier formulation in [52]. In the standard form case, the Tikhonov problem becomes

$$\min \| \, Ax - b \, \|_F \qquad \textit{subject to} \qquad \| \, x \, \|_2 \leq \alpha. \tag{A.94}$$

with solution x_α satisfying

$$\left(A^T A + \lambda I_n\right) \, x_\alpha = A^T b \tag{A.95}$$

Similarly, R-TLS problem takes the form,

$$\min \left\| \, (A,\, b) - \left(\tilde{A},\, \tilde{b}\right) \, \right\|_F \qquad \textit{subject to} \qquad \tilde{b} = \tilde{A}x, \quad \| \, x \, \|_2 \leq \alpha. \tag{A.96}$$

with solution $\bar{x}_\alpha$ satisfying

$$\left(A^T A + \lambda_{IL} I_n\right) \bar{x}_\alpha = A^T b \tag{A.97}$$

whenever $\| \bar{x}_\alpha \|_2 > \alpha$, with $\lambda_{IL} = \lambda_I + \lambda_L$. Clearly, these two solutions are closely related. For each value of α , the resulting solutions x_α and $\bar{x}_\alpha$ are related as in Table A.1

Table A.1: Relation between the solutions x_α, $\bar{x}_\alpha$ and α value.

α	Solutions	λ_{IL}
$\alpha < \| x_{LS} \|_2$	$\bar{x}_\alpha = x_\alpha$	$\lambda_{IL} > 0$
$\alpha = \| x_{LS} \|_2$	$\bar{x}_\alpha = x_\alpha = x_{LS}$	$\lambda_{IL} = 0$
$\| x_{LS} \|_2 < \alpha < \| x_{TLS} \|_2$	$\bar{x}_\alpha \neq x_\alpha = x_{LS}$	$0 > \lambda_{IL} > -\bar{\sigma}_{n+1}^2$
$\alpha \geq \| x_{TLS} \|_2$	$\bar{x}_\alpha = x_{TLS}, \quad x_\alpha = x_{LS}$	$\lambda_{IL} = -\bar{\sigma}_{n+1}^2$

where $\bar{\sigma}_{n+1}$ denotes the smallest singular value of (A, b) .

In the general form case, the R-TLS solution $\bar{x}_\alpha$ is different from the Tikhonov solution whenever the residual $b - Ax$ is different from zero, since both λ_I and λ_L are nonzero. For a given α , there are usually several pairs of parameters λ_I and λ_L , and thus several solutions $\bar{x}_\alpha$, that satisfy relations A.56-A.58, but only one of these, satisfy the optimization problem A.55. According to A.58 this is the solution that corresponds to the smallest value of $| \lambda_I |$. The relations in Table A.2 hold.

Table A.2: Relation between the solutions and parameters of the R-TLS problem.

α	Solution	λ_I	λ_L
$\alpha < \| Lx_{TLS} \|_2$	$\bar{x}_\alpha \neq x_{TLS}$	$\lambda_I < 0 \qquad \partial\lambda_I/\partial\alpha > 0$	$\lambda_L > 0$
$\alpha \geq \| Lx_{TLS} \|_2$	$\bar{x}_\alpha = x_{TLS}$	$\lambda_I = -\bar{\sigma}_{n+1}^2$	$\lambda_L = 0$

A.5.5 Other Direct Methods

There is a variant of Tikhonov's method for the case when A is Toeplitz and $L = I_n$. The filter factors of this method are:

$$f_i = \frac{\sigma_i}{\sigma_i + \rho_i}, \qquad i = 1, \ \ldots, \ n \tag{A.98}$$

and using either $\rho_i = \lambda$ (a constant) or $\rho_i = \| Lv_i \|_2^2$, i.e, a measure of smoothness of the ith singular vector v_i is suggested with this method (Ekstrom and Rhoads Method). A possible further extension to the case $L \neq I_n$ is proposed to use the filter factors $f_i = \frac{\sigma_i}{\sigma_i + \lambda \mu_i}$ in the GSVD expansion. These filter factors decay more slowly than the Tikhonov filter factors and thus, in a sense, introduce less filtering.

Regularization in other norms than the L2-norm are also important, and problems of the general form

$$\min \left\{ \| Ax - b \|_p + \lambda^2 \ \| x \|_s^s \right\} \tag{A.99}$$

are considered where $1 < p < \infty$ and $1 < s < \infty$. The s-norm of a matrix x is defined as:

$$\| x \|_s^s = \sum_{i=1}^{n} | x |_i^s \tag{A.100}$$

It can be seen that as the value s increases, the penalization is less severe for larger values and more severe for smaller values of the argument of the s-norm function.

Regarding the solution norm, the L1-norm $\| x \|_1$ has achieved special attention in some applications, such as reflection seismology, where this norm is able to produce a "sparse spike train" solution, i.e, a solution that has the least number of nonzero components. This feature of the 1-norm can be used to compute regularized solutions with steep gradients and even discontinuities, when $\| L x \|_2$ in Tikhonov method is replaced by the 1-norm of a derivative of x. When 1-norm is used with the matrix L is equal to the discrete gradient approximation, this method is called T*Total Variation* (TV) *Regularization.*

TV de-noising and regularization are able to produce solutions with localized steep gradients without prior knowledge of the positions of these steep gradients.

A non-quadratic s-norm regularization cost analogous to the quadratic Tikhonov regularization can be expressed as:

$$\hat{x} = \arg\min_{x} \left\{ \| b - Ax \|_2^2 + \lambda^2 \| Lx \|_s^s \right\} \tag{A.101}$$

One difficulty of this particular choice of cost function is that the s-norm for values of s less or equal to 1 is not differentiable at zero [43]. The cost function can be rewritten as

$$\hat{x} = \arg\min_{x} \left\{ \| b - Ax \|_2^2 + \lambda^2 \sum_{1}^{n} \left(\left|(Lx)_i\right|^2 + \beta \right)^{k/2} \right\} \tag{A.102}$$

where β is a small positive constant. The solution x to this problem is a solution to the equality:

$$\left(A^T A + \lambda^2 L^T W_\beta \left(x \right) L \right) \, x = A^T b \tag{A.103}$$

where $W_\beta \left(x \right) = \frac{k}{2} diag \left(\left(\left|(Lx)_i\right|^2 + \beta \right)^{k/2} \right)$. This nonlinear equation is proposed to be solved iteratively, starting with an initial guess $x^{(0)}$ and using the fact that at convergence $x^{(n+1)} = x^{(n)}$.

$$\left(A^T A + \lambda^2 L^T W_\beta \left(x^{(n)} \right) L \right) \, x^{(n+1)} = \gamma \, A^T b + (1 - \gamma) \, H \left(x^n \right) x^{(n)} \tag{A.104}$$

where $\gamma \leq 1$ is a parameter controlling the relative amplitude of the terms in the modified Hessian update equation [43].

Maximum Entropy Regularization [42] is another technique which yields a solution with only positive elements. The solution is defined much the same as the Tikhonov regularization, the only difference being the choice of the penalty term such that:

$$x_{me} = \arg\min_x \left\{ \| b - Ax \|_2^2 + \lambda^2 \sum_1^n x_i \log(w_i x_i) \right\}, \qquad x_i \geq 0 \quad \text{(A.105)}$$

where w_i are positive weights. It can be observed that the maximum entropy method penalizes large elements x_i less than Tikhonov regularization method as illustrated in Figure A.1.

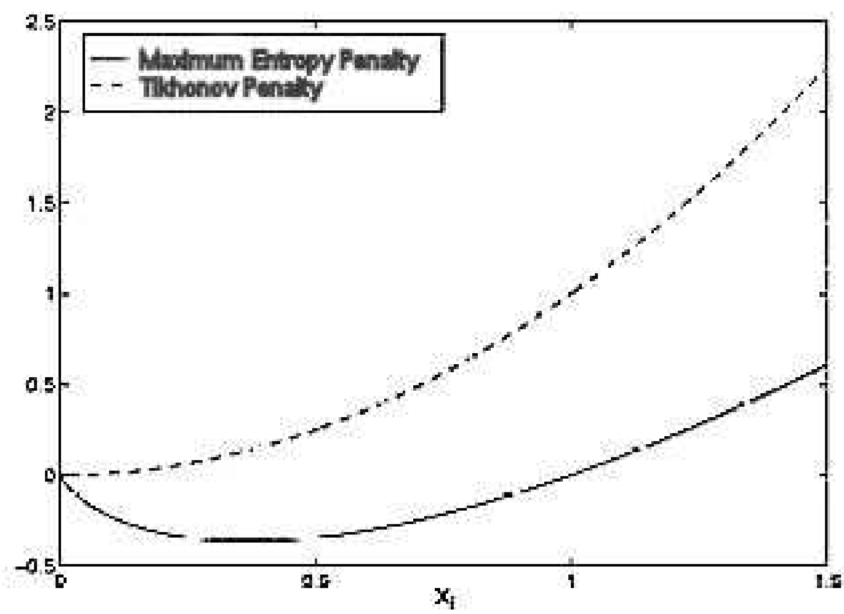

Figure A.1: Penalty term comparison

Note that the maximum entropy penalty is minimized when the i^th component of x is equal to $x_i^* = \frac{e^{-1/w_i}}{w_i}$ (assuming log is the natural logarithm). Selecting all w_i equal, we implicitly penalize for large differences in values between the components of x. The latter effect could also have been obtained by a Tikhonov penalty of the form $\| x - x^* \|$, where x^* is a vector with all components equal.

A.6 Iterative Regularization Methods

Iterative methods for linear systems of equations ad linear least squares problems are based on iteration schemes that access the coefficient matrix A only via matrix-vector multiplications with A and A^T , and they produce a sequence of iteration vectors $x^{(k)}, \quad k = 1,\ 2,\ \ldots$, that converge to the desired solution. Iterative methods are preferable to direct methods when the coefficient matrix is so large that it is too time-consuming or too memory demanding to work with an explicit decomposition of A [46].

A.6.1 Landweber Iteration

This is one of the main iterative regularization methods, which takes the form

$$x^{(k)} = x^{(k-1)} + wA^T \left(b - Ax^{(n-1)}\right) \tag{A.106}$$

where $x^{(0)} = 0$, w is a real parameter satisfying $0 < w < 2 \left\|A^T A\right\|_2^{-1}$. After k iterations, we have the filtering factors:

$$f_i^{(k)} = 1 - \left(1 - w\sigma_i^2\right)^k, \qquad i = 1, \ldots, n \tag{A.107}$$

A disadvantage of this method is that it may take many steps k to achieve a useful regularized solution [42].

A.6.2 Regularizing Conjugate Gradient(CG) Iterations

The CG method was originally developed for solving large sparse systems of equations with a symmetric positive definite coefficient matrix. Applying the method to normal equations $A^T Ax = A^T b$ produces iterates which converges to a least squares solution for the problem $Ax = b$. One implementation of the CG method for solving the system $A^T Ax = A^T b$ is the CGLS method which iterates the following statements [42],[46] for $k = 1,\ 2, \ldots$:

$$
\begin{aligned}
\alpha_k &= \frac{\left\|A^T r^{(k-1)}\right\|_2^2}{\left\|A d^{(k-1)}\right\|_2^2} \\
x^{(k)} &= x^{(k-1)} + \alpha_k d^{(k-1)}, \\
r^{(k)} &= r^{(k-1)} - \alpha_k A d^{(k-1)}, \qquad (101) \\
\beta_k &= \frac{\left\|A^T r^{(k)}\right\|_2^2}{\left\|A^T r^{(k-1)}\right\|_2^2}, \\
d^{(k)} &= A^T r^{(k)} - \beta_k A d^{(k-1)}
\end{aligned}
\tag{A.108}
$$

where $r^{(k)}$ is the residual vector $r^{(k)} = b - Ax^{(k)}$. The CGLS algorithm is initialized by with the starting vector $x^{(0)} = 0$, $r^{(0)} = b$ and $d^{(0)} = A^T r^{(0)}$.

It can be observed that the CG method avoids the computation of $A^T A$, which is numerically an advantage as $A^T A$ is worse conditioned than A and A^T . The filter factors for the CG method after k iterations can be shown to be:

$$
f_i^{(k)} = 1 - \prod_{j=1}^{k} \frac{\theta_j^{(k)} - \sigma_i^2}{\theta_j^{(k)}}, \qquad i = 1, \ldots, n \tag{A.109}
$$

where $\theta_1^{(k)} \geq \theta_2^{(k)} \geq \cdots \geq \theta_k^{(k)}$ are called *Ritz values* [42]. The Ritz values can be precisely defined and can be shown to approach squared singular values such that $\theta_j^{(k)} \rightarrow \sigma_j^2 \quad as \quad k \rightarrow n$ where $k \leq n$. Also, A.109 requires that $f_i^{(k)} = f_j^{(k)}$ whenever $\sigma_i = \sigma_j$. Furthermore, we have $f_i^{(k)} \rightarrow 1 \quad as \quad k \rightarrow n$, which states the fact that CG iterates converge towards the least squares solution.